Titre: Title:	Numerical modeling of liquid spills from the damaged container and collision of two rising bubbles in partially filled enclosure using modified Volume-Of-Fluid (VOF) method
Auteurs: Authors:	Tarek Merabtene, Faroogh Garoosi, & Tew-Fik Mahdi
Date:	2023
Type:	Article de revue / Article
Référence: Citation:	Merabtene, T., Garoosi, F., & Mahdi, T.-F. (2023). Numerical modeling of liquid spills from the damaged container and collision of two rising bubbles in partially filled enclosure using modified Volume-Of-Fluid (VOF) method. Engineering Analysis with Boundary Elements, 154, 83-121. https://doi.org/10.1016/j.enganabound.2023.05.037

Titre de la revue: Journal Title:	Engineering Analysis with Boundary Elements (vol. 154)
Maison d'édition: Publisher:	Elsevier
URL officiel: Official URL:	https://doi.org/10.1016/j.enganabound.2023.05.037
Mention légale: Legal notice:	

Numerical modeling of liquid spills from the damaged container and collision of two rising bubbles in partially filled enclosure using modified Volume-Of-Fluid (VOF) method

Tarek Merabtene[a], Faroogh Garoosi[*,b], Tew-Fik Mahdi[b]

[a]Department of Civil and Environmental Engineering, University of Sharjah. P. O.Box 27272 Sharjah. United Arab Emirates

[b]Department of Civil, Geological and Mining Engineering, Polytechnique Montreal, Montreal, Quebec, Canada

Corresponding author: faroogh.garoosi@polymtl.ca

First author: tmerabtene@sharjah.ac.ae

Third author: tewfik.mahdi@polymtl.ca

Abstract

In the present work, two crucial shortcomings associated with Volume-Of-Fluid (VOF) model namely: (1) spurious interface smearing arising from false-diffusion errors, and (2) non-physical velocity fluctuation across the physical discontinuities, are systematically addressed, aiming to establish a unique methodological foundation and guidelines for the enhancement of interface-capturing techniques in handling multi-fluid flows. To accomplish this objective, first, a novel third-order bounded convection scheme is derived based on the Normalized Variable Diagram and Total Variation Diminishing concepts (NVD-TVD) and is then applied for the discretization of the volume-fraction equation. To cope with the instability issue induced by pressure fluctuation, the standard version of the implicit non-iterative PISO algorithm is first modified by incorporating the third pressure-correction step into the algorithm and is then utilized for the treatment of the pressure-velocity coupling. A feasibility and applicability of the proposed modifications in dealing with violent free-surface and multi-fluid flows are demonstrated against the five different challenging benchmark cases including two-dimensional dam-break flow over the dry bed, oil spill from the damaged container, single bubble rising, merging of two rising bubbles and two-fluid

Rayleigh-Taylor Instability problems. The comparison of the obtained results with previously published literatures vividly corroborates the robustness and versatility of the modified VOF model in handling multi-fluid flows involving interface coalescence and breakup events. In the last staged, three new benchmark solutions namely (1) coalescence of two consecutive bubbles inside the partially filled enclosure, (2) two-dimensional three-fluid Rayleigh-Taylor Instability, and (3) oil/water spilling from the damaged tank are analyzed using the verified VOF method, aiming to provide a high-quality validation data for CFD simulations.

Keywords: Third-order NVD-TVD bounded convection scheme; Modified PISO algorithm (MPISO); Multi-fluid flows; ELVIRA technique; Improved VOF model; 2D Bubble rising;

Nomenclature

C_{φ}	Interface compression coefficient
F_g	gravity force
F_{ST}	surface tension force
g	Gravitational acceleration, ms^{-2}
H	enclosure height, m
L	Length of the enclosure (m)
$\mathbf{n}$	interface normal vector
p	pressure, Nm^{-2}
P	dimensionless pressure
t	time (s)
t^*	dimensionless time, $(t\alpha/H^2)$
u,v	velocity components, ms^{-1}
$\boldsymbol{u}_R$	artificial compressive velocity, ms^{-1}

Re	Reynolds number
U, V	Dimensionless velocity components
x,y	Cartesian coordinates, *m*
X, Y	Dimensionless Cartesian coordinates
We	Weber number

Greek symbols

μ	dynamic viscosity, kg m^{-1} s^{-1}
ν	kinematic viscosity, m^2s^{-1}
ρ	density, kg m^{-3}
φ	Volume fraction of the primary phase (phase 1)
λ	Volume fraction of the secondary phase (phase 2)
γ	Volume fraction of the third phase (phase 3)
k	curvature of interface
σ	interfacial tension coefficient
ψ	stream function$(=-\int_{Y_0}^{Y} U\partial Y+\psi(X,Y_0))$

Subscripts

L	Lighter fluid
H	Heavy fluid
M	Middle fluid

1. Introduction

The study of incompressible multi-fluid problems is of great importance since they are ubiquitous in both natural and industrial processes, covering a broad spectrum of applications from chemical reactors [1], fuel injection and spray atomization [2], to nuclear power plants [3]. During the last two decades, due to the significant progress in the development of computer hardware and

computational science, Computational Fluid Dynamics (CFD) technique as an economical and promising alternative to the traditional experimental and theoretical approaches have widely utilized to understand the basic principles of multiphase flows [4]. Conversely, the establishment of accurate and efficient multi-fluid CFD methodology is still ongoing challenge and the applicability of existing computational models are mostly restricted to simple configurations. However, a comprehensive literature survey conducted by Gibou et al. [5] revealed that among various CFD techniques, Level-Set (LS) [6] and Volume-Of-Fluid (VOF) [7] methods as two of the most popular interface-capturing methods defined in Eulerian description, have been widely employed to investigate the hydrodynamic characteristics of various multiphase transport phenomena. Examples include simulations of formation/evaporation of droplets [8], bubble rising [9,10], sloshing of liquid tank [11], wave-structure interactions [12], nanofluids [13] and dam failure flows [14]. Despite the proven effectiveness and potential of LS and VOF models in handling multi-fluid flows with sever deformation, stretching, and tearing, the results of Kumar et al. [15] showed that, the former method is characterized by density error accumulation which manifest itself through unphysical loss (or gain) of mass especially in long term simulations especially when the fluid filaments become comparable to size of computational grids. To be more precise, the LS approach uses an explicit δ-function formulation (i.e. Heaviside smooth function) to describe the distribution of the material discontinuities and determine its geometrical information (i.e. interface curvature and its normal vectors) [16]. However, due to the implementation of the smoothing operator, the numerical conservation cannot be preserved rigorously. Contrary to LS model, the VOF uses an implicit volume fraction advection equation to advect the scalar quantities and capture the position of the targeted fluid in space [17]. Thanks to the implicit surface representation, VOF has propensity to guarantee mass conservative and handle

multi-fluid flows in the case of three-dimensions or non-orthogonal meshes. Nevertheless, as highlighted by Lima et al. [18], VOF is in general less accurate in the determination of the interface properties/orientations compared to LS model and has a tendency to smearing out the steep gradients and produce false velocity oscillations across the physical jumps. Over the years, considerable research efforts have been devoted to address the aforementioned shortcomings associated with VOF methodology.

An initial effort toward mitigation of numerical smearing was made by Leonard [19] who proposed the notion of non-oscillatory bounded schemes known as NVD (Normalized Variable Diagram). He constructed a novel high-resolution bounded convection scheme so-called SHARP and showed that this scheme is less diffusive than the classical Upwind scheme and can simultaneously ensure both boundedness and conservativeness of the numerical solutions. Later, Gaskell et al. [20] modified and generalized the NVD concept through incorporating the principle of CBC constraints (Convection Boundedness Criterion) into the scheme. They proposed a new monotone convection scheme known as SMART and mathematically demonstrated that, the NVD constraints cannot solely guarantee iterative convergence and monotonicity of the solution such that the second criterion, related to CBC conditions, needs to be fulfilled. From then on, many scholars have been motivated to construct high-resolution bounded convection schemes on the basis of hybrid NVD-CBC conditions. Examples include SMARTER [21], HLPA [22], SOUCUP [23], ISNAS [24], HRIC [25] and CUBISTA [26]. However, the results of Zijlema [24] revealed that majority of these NVD schemes don't completely assure CBC conditions and are prone to numerical oscillations (i.e. overshoots/undershoots). Similar observations were also reported by Ubbink and Issa [27] who proposed a blended high-resolution differencing scheme known as CICSAM (Compressive Interface Capturing Scheme for Arbitrary Meshes) for arbitrary meshes by

combining the bounded Hyper-C and Ultimate-Quickest schemes. They showed that, unlike the previously mentioned NVD-CBC schemes, the geometrical quantities of the interface namely its curvature and normal vector can be easily computed by the implementation of the CICSAM. However, the numerical findings of Wacławczyk et al. [25], Malgarinos et al. [28], Gopala et al. [29] and Arote et al. [30] showed that, in spite of its simplicity and relatively low computational cost, the CICSAM suffers from low-order of accuracy and cannot preserve the shape of the interface especially when it comes to resolve sharp gradients. They suggested the use of M-CICSAM scheme (i.e. Modified version of CICSAM) to simulate incompressible multiphase flows involving severe breaking up, coalescence and/or deformation events. Another non-dimensional diagram was later introduced by Harten [31] and Sweby [32] who established the concept of Total Variation Diminishing (TVD) and Flux-Limiter Function in the finite volume framework for the construction of second-order accurate and oscillation-free convection schemes. Since then, a number of second-order limiter functions were developed based on the TVD properties such as MUSCL (Van-Leer) [33], Van-Albada [34], MINMOD [35], Harmonic [36,37] and OSPRE [38]. A brief review of the latest and up-to-date TVD schemes with associated flux-limiter function can be found in work of Zhang et al. [39]. Recently, Alves et al. [26] and Jasak et al. [40] numerically showed that, although the TVD criteria are more restrictive compared to the NVD-CBC conditions in constructing monotone schemes, the former is slightly diffusive than the latter and cannot accurately preserve the sharpness of the interfaces. Moreover, in a pioneering work, they embedded an additional criterion so-called "*smoothness condition*" into the bounding strategy and pointed out that, the smooth characteristic of the blended schemes in the TVD or NV diagram has a vital impact on the stability of the numerical simulation such that the abrupt alteration in the derivative of the dependent variable must be avoided.

Recently, Heyns et al. [41] suggested the use of Interface-Sharpening Technique (IST) as a second remedy to the problem of preserving interface resolution. In this technique, in order to remove the interface smearing due to numerical diffusion and control the excessive grows of interface thickness, an additional gradient terms so-called "*Artificial Compression Velocity*" is inserted into the transport equation. The performance and effectiveness of this technique were later verified by Zanutto et al. [42] , Akhlaghi et al. [43] and Cerqueira et al. [44] against a series of challenging multiphase problems including droplet evaporation, bubble rising, plug/slug flows, and slurry Taylor flow. They found that, the presence of Artificial Compression Velocity terms in the colour function can considerably alleviate the undesirable effects of false-diffusion errors, thereby retaining the integrity and shape of interface.

Referring to the second drawback associated with VOF model, in order to eliminate the unphysical velocity fluctuations in the vicinity of the steep gradients and material discontinuities, Wang et al. [45], Radman et al. [46], Pham et al. [47] and Tretola et al. [48] employed the improved version of PISO [49] algorithm so-called "PIMPLE" (mixed PISO-SIMPLE available in OpenFOAM® platform) to solve the link between velocity and pressure fields and speed up the convergence rate of simulations. Their results showed that, since PIMPLE takes the advantages of both iterative SIMPLE and non-iterative PISO algorithms, this pressure-based solver is less sensitive to numerical instability arising from selecting large time-steps. However, the results of comparison study conducted by Wang et al. [50] between five classical pressure-based solvers (i.e. SIMPLE, SIMPLER, SIMPLEC, SIMPLEST, SIMPLEX and PIMPLE) revealed that, due to the existence of the additional iterative SIMPLE loop in the PIMPLE algorithm, it needs a large amount of computer storage and exhibits the disadvantages of CPU time requirements which makes PIMPLE

more computationally expensive when it comes to solve strongly coupled three-dimensional systems.

Finally, as highlighted before, the third drawback faced by VOF methodology is to identify the geometrical information of the interface for the accurate imposition of surface tension force. To address this issue, Youngs [51] introduced the concept of Piecewise Line Interface Construction (PLIC) where a series of sloped line segments defined in the 3×3 grid stencils is utilized to approximate fluid-fluid interface curvature. However, the analytical investigation conducted by Pilliod et al. [52] showed that, Youngs' PLIC reconstruction technique suffers from the first-order of accuracy, that is, it cannot efficiently estimate the actual interface orientation. To tackle this shortcoming, they proposed a second-order least-square fitting approach known as ELVIRA and concluded that, this iterative technique can successfully predict the interface slope but at the expense of an increased computational cost. Similar observations were also highlighted by Garoosi et al. [53] who implemented ELVIRA technique for the enforcement of the surface tension force in modeling single rising bubble and dam failure problems.

In light of the above literature review, one can conclude that there are still two major drawbacks associated with VOF methodology including (1) interface smearing in the case of the strong flow-to-grid skewness, and (2) the oscillatory convergence behaviour due to the inefficiency in the classical pressure-based solvers in dealing with incompressible convection-dominated multiphase flows. As highlighted earlier, these two disadvantages can remarkably jeopardize the reliability and accuracy of the numerical solutions or even lead to the unwanted termination of the calculations. Thus, the primary objective of the present study is to systematically address the aforementioned drawbacks. To accomplish this, a novel third-order bounded monotone scheme is first developed based on the TVD, NVD and CBC criteria and is then employed for the treatment

of the convection terms in the Navier-Stokes and advection equations (see section 4). To further suppress interface smearing and enforce a selected interface thickness, the Artificial Compression Velocity term (ACT) is also embedded into the advection equation. In order to tackle the problem of pressure/velocity oscillation across the interfaces and enhance the convergence rate of the numerical simulations, the standard PISO algorithm is revised by incorporating the third pressure correction step into the methodology. In addition, the second order ELVIRA technique is utilized to estimate the normal vector of the interface and accurate imposition of the surface tension force. The feasibility and accuracy of the proposed modifications are verified against the five canonical test cases. Having verified the state-of-the-art CFD code, the developed VOF code is employed to introduce and examine four new benchmark cases namely (1) three-fluid Rayleigh-Taylor Instability problem, (2) coalescence of two consecutive bubbles inside the partially filled enclosure, and (3) oil/water spilling from the damaged tank, aiming to provide detailed numerical data for CFD validation and shed further light on the transient evolution of multi-fluid flows (see section 6).

2. Problem statement and governing equations

Schematic diagram of ten different multi-fluid problems under consideration with associated boundary conditions and coordinate system are displayed in Fig. 1 where cases 1 to 5 are utilized to demonstrate the validity and precision of the proposed modifications, whereas cases 6 to 10 are introduced to establish the state-of-the-art benchmark solutions for CFD validation. The improved VOF method was coded in the Intel® Fortran Compiler Classic 2021.

The flow for unsteady, incompressible and viscous Newtonian fluid can be described using the conservation equations for continuity, momentum, and volume fraction as follows [27,54]:

$$\frac{\partial \rho}{\partial t}+\frac{\partial \rho u}{\partial x}+\frac{\partial \rho v}{\partial y}=0, \tag{1}$$

$$\frac{\partial \rho_m u}{\partial t}+\frac{\partial \rho_m uu}{\partial x}+\frac{\partial \rho_m vu}{\partial y}=-\frac{\partial p}{\partial x}+[\frac{\partial}{\partial x}\mu_m(\frac{\partial u}{\partial x})+\frac{\partial}{\partial y}\mu_m(\frac{\partial u}{\partial y})]+F_{ST} \tag{2}$$

$$\frac{\partial \rho_m v}{\partial t}+\frac{\partial \rho_m uv}{\partial x}+\frac{\partial \rho_m vv}{\partial y}=-\frac{\partial p}{\partial y}+[\frac{\partial}{\partial x}\mu_m(\frac{\partial v}{\partial x})+\frac{\partial}{\partial y}\mu_m(\frac{\partial v}{\partial y})]+\rho_m g+F_{ST} \tag{3}$$

$$\frac{\partial \varphi}{\partial t}+\frac{\partial \varphi u}{\partial x}+\frac{\partial \varphi v}{\partial y}+\nabla\cdot(\varphi(1-\varphi)\mathbf{u}_{R\varphi})=0 \tag{4}$$

$$\frac{\partial \lambda}{\partial t}+\frac{\partial \lambda u}{\partial x}+\frac{\partial \lambda v}{\partial y}+\nabla\cdot(\lambda(1-\lambda)\mathbf{u}_{R\lambda})=0 \tag{5}$$

$$\varphi+\lambda=1 \text{ or } \varphi+\lambda+\gamma=1 \tag{6}$$

where *u* and *v* denote the dimensional fluid velocities in *x* and *y*-directions while the terms *g*, *t* and *p* are gravity acceleration, time and pressure, respectively. ρ_m and μ_m are the linear interpolations of the physical properties of the mixed fluid at the interface which may be approximated by [55]:

$$\rho_m=\varphi\rho_1+(1-\varphi)\rho_2 \tag{7}$$

$$\mu_m=\varphi\mu_1+(1-\varphi)\mu_2 \tag{8}$$

$$\rho_m=\varphi\rho_1+\lambda\rho_2+(1-\lambda-\varphi)\rho_3 \tag{9}$$

$$\mu_m=\varphi\mu_1+\lambda\mu_2+(1-\lambda-\varphi)\mu_3 \tag{10}$$

Note that, in the present study, Eqs. (7)-(8) are applied for calculating the density and dynamic viscosity of two-fluid flow problems (i.e. cases 1, 3, 4 and 5) whereas Eqs. (9) and (10) are exploited for three-phase cases. The term F_{ST} in the momentum equations is volumetric surface tension force which is formulated based on the Continuum Surface Force (CSF) model proposed by Brackbill et al. [56] as:

$$\begin{aligned} F_{ST,\varphi}&=\sigma_\varphi k_\varphi\nabla\varphi, \\ F_{ST,\lambda}&=\sigma_\lambda k_\lambda\nabla\lambda, \end{aligned} \tag{11}$$

In the above equations, σ_i represents the interfacial tension coefficient between working fluids and k_i is the curvature of interface in a computational cell defined as which is approximated as the divergence of unit surface normal ($\mathbf{n}$) given by [57]:

$$\begin{aligned} k_\varphi &= -\nabla\cdot\mathbf{n}_\varphi = -\nabla\cdot\left(\frac{\nabla\varphi}{|\nabla\varphi|}\right), \\ k_\lambda &= -\nabla\cdot\mathbf{n}_\lambda = -\nabla\cdot\left(\frac{\nabla\lambda}{|\nabla\lambda|}\right), \end{aligned} \tag{12}$$

$$\begin{aligned} \mathbf{n}_\varphi &= \frac{\vec{n}_\varphi}{|\vec{n}_\varphi|},\ \vec{n}_\varphi = \nabla\varphi, \\ \mathbf{n}_\lambda &= \frac{\vec{n}_\lambda}{|\vec{n}_\lambda|},\ \vec{n}_\lambda = \nabla\lambda, \end{aligned} \tag{13}$$

The last terms ($\nabla\cdot(\varphi(1-\varphi)\mathbf{u}_R)$ and $\nabla\cdot(\lambda(1-\lambda)\mathbf{u}_R)$) in Eqs. (4) and (5) represent the contribution of the interface-sharpening technique (artificial compression velocity) [41] which is non-zero only at the interface owing to the presence of $\varphi(1-\varphi)$ and $\lambda(1-\lambda)$ terms. $\mathbf{u}_R$ denotes the compressive velocity which is quantified based on local velocity in vicinity of the interface region as follows [43]:

$$\begin{aligned} \mathbf{u}_{R\varphi} &= C_\varphi\left|\vec{u}\right|\mathbf{n}_\varphi = C_\varphi\left|\vec{u}\right|\frac{\nabla\varphi}{|\nabla\varphi|}, \\ \mathbf{u}_{R\lambda} &= C_\lambda\left|\vec{u}\right|\mathbf{n}_\lambda = C_\lambda\left|\vec{u}\right|\frac{\nabla\lambda}{|\nabla\lambda|}, \end{aligned} \tag{14}$$

The coefficient $C_\varphi = C_\lambda = 0.5$ is the primary parameter which controls the compression of the interface [42].

3. Numerical methodology

The governing equations are discretized using the Finite Volume Method (FVM) on a staggered mesh arrangement where scalar variables, such as pressure, density and viscosity are stored in the center of the grid while velocity components are stored at the cell faces of scalar control volumes [58,59]. To resolve physical discontinuity without generating spurious fluctuations, a novel third-order bounded Upwinding scheme is first derived on the basis of the NVD-TVD concepts and then adopted for the discretisation of the convection terms in momentum and transport equations. Meanwhile, the diffusion terms on the right hand side of Eqs. (2) and (3) is approximated by the central differencing scheme. In addition, in order to mitigate the unphysical pressure/velocity oscillation in the vicinity of steep gradients, the Modified version of the PISO algorithm is first introduced and is then implemented for the treatment of the pressure-velocity coupling in unsteady incompressible multi-fluid flows. A more detailed description of the newly developed pressure-based methodology is given in Appendix A. To further increase the accuracy of the numerical solution, the second-order interface reconstruction technique (PLIC-ELVIRA) pioneered by Pilliod et al. [52] is employed for the enforcement of the surface tension effects and determination of the interface curvature and its normal vector. Interested readers can find a detailed discussion of the ELVIRA technique in previous work of Garoosi et al. [53,60], Finally the developed Fortran code based on the ELVIRA technique is also provided as a supplementary material.

4. A novel third-order oscillation-free bounded NVD scheme

Inspired by works of Leonard [19] and Sweby [32], a new third-order bounded convection scheme is formulated in this section by combination of the Total Variational Diminishing and Normalized Variable Diagram constraints (TVD-NVD) for the approximation of the convection terms in Navier-Stokes and transport equations. To accomplish this goal, the TVD region (shaded area

highlighted in grey color) in Sweby diagram (see also table 1) is first mapped into the NV diagram by using the following relationships [61,62]:

$$\mathrm{K}_f = \Phi_c + \frac{1}{2}\psi(r)\times(1-\Phi_c), \qquad \Phi_c = \frac{r}{1+r} \tag{15}$$

Note that, in both diagrams, the borders of the TVD region are bounded from below and top by two well-known Minmod and Superbee linear schemes which indicates that any linear or non-linear scheme which lie outside this region cannot retain the monotonicity of the solutions [63]. To reach the third-order monotone bounded properties, the desired scheme must satisfy the necessary and sufficient conditions formulated by Leonard [19], Zijlema [24], Gaskell et al. [20] and Alves et al. [26] as:

- To guarantee the TVD properties with first-order of accuracy, the normalized function (K_f) must be restricted in the shaded area and passes through the points (0,0) and (1,1) in NV diagram,
- To guarantee the second-order of accuracy, the normalized function be nonlinear or piecewise linear and passes through the point (0.5, 0.75) in NV diagram,
- To achieve the third-order of accuracy, the given normalized function must pass through the critical point of (0.5, 0.75) with a tangential slope of 0.75 in NV diagram,
- To suppress the oscillatory convergence behaviour of the numerical calculations, the normalized function must be smooth throughout the TVD area with continuous derivative "*smoothness condition*",

By considering the above criteria, the following piecewise non-linear function can be constructed in NV diagram:

$$\mathrm{K}_f = \begin{cases} -\dfrac{625}{128}\Phi_c^4 + 2\Phi_c & 0 \le \Phi_c \le 0.4 \\ \dfrac{3}{4}\Phi_c + \dfrac{3}{8} & 0.4 < \Phi_c \le 0.6 \\ -\dfrac{375}{1504}\Phi_c^4 + \dfrac{25}{1504}\Phi_c^3 + \dfrac{1425}{1504}\Phi_c + \dfrac{429}{1504} & 0.6 < \Phi_c \le 1.0 \\ \Phi_c & \Phi_c > 1 \text{ or } \Phi_c < 0 \end{cases} \tag{16}$$

It can be seen from Fig. 2 that, similar to the conventional first-order Upwind differencing scheme ($\mathrm{K}_f = \Phi_c$), the newly developed piecewise polynomial function is located in TVD area and passes through the points $\mathrm{K}_f(0) = 0$ and $\mathrm{K}_f(1) = 1$, therefore it guarantees boundedness of the solution while satisfying the first-order of accuracy. Furthermore, similar to the HLPA scheme ($\mathrm{K}_f = -\Phi_c^2 + 2\Phi_c$) proposed by Zhu et al. [22,23], the given piecewise function passes through the point $\mathrm{K}_f(0.5) = 0.75$ which is necessary and sufficient condition for second-order accuracy. In addition to that, since the proposed function is completely coincided with Quick scheme ($\mathrm{K}_f = 3\Phi_c/4 + 3/8$) in the smooth flow region ($0.4 \le \Phi_c \le 0.6$), it has the same slope ($d\mathrm{K}_f / d\Phi_c\big|_{\Phi_c = 0.5} = 3/4$) as that of QUICK at the intersection point (0.5, 0.75) which confirms that the newly constructed function can successfully ensure third-order accuracy. More importantly, contrary to the SMART, CUBISTA and MUSCL schemes [20,26,64] which are characterized by breaking point or abrupt changes of slop within their linear sub-functions in the shaded region, the proposed function is differentiable/continuous and switches smoothly between its pieces without any break, angle, or cusp ($\mathrm{K}_{f1}(0.4) = \mathrm{K}_{f2}(0.4) = 27/40$ and $\mathrm{K}_{f2}(0.6) = \mathrm{K}_{f3}(0.6) = 33/40$) which can be regarded as an advantageous for fully-implicit implementations [65]. More precisely, in order to circumvent the problem of "*switching instability*" and enhance the convergence rate of the solution, the first derivatives of each sub-function in Eq. (16) (i.e. $\mathrm{K}_{f1} = -625\Phi_c^4/128 + 2\Phi_c$,

$K_{f2} = 3\Phi_c/4 + 3/8$ and $K_{f3} = (-375\Phi_c^4 + 25\Phi_c^3 + 1425\Phi_c + 429)/1504$ at the points (0.4, 0.675) and (0.6, 0.825) has been designed to be equal ($dK_{f1}/d\Phi_c\big|_{\Phi_c=0.4} = dK_{f2}/d\Phi_c\big|_{\Phi_c=0.4} = 3/4$ and $dK_{f2}/d\Phi_c\big|_{\Phi_c=0.6} = dK_{f3}/d\Phi_c\big|_{\Phi_c=0.6} = 3/4$), securing the fulfillment of the "*smoothness condition*" within the TVD area. The effects of this crucial criterion on the iterative convergence of the numerical solution were carefully examined by Alves et al. [26] and Gao et al. [66] who analytically showed that, when the NVD scheme has an abrupt change of slope in the smooth flow region ($0.4 \le \Phi_c \le 0.6$), it tends to exhibit spurious pressure/velocity fluctuation especially in vicinity the of the physical discontinuities in the complex multiphase flows. Before proceeding further, it should be mentioned that in Eq. (16), the normalized variable $\Phi_c = (\phi_C - \phi_U)/(\phi_D - \phi_U)$ stands for the ratio of upstream gradient to downstream gradient where the subscripts U and D represent the upstream and the downstream grid points, respectively [19]. To provide further insight into the computer programming of the proposed NVD scheme and demonstrate how to discretize it on the staggered grid arrangement in Cartesian coordinates, the following two-dimensional convection-diffusion equation in the steady state situation is considered as an illustration [67]:

$$\frac{d}{dx}(\rho u\phi) + \frac{d}{dy}(\rho v\phi) = \frac{d}{dx}[\eta \frac{d\phi}{dx}] + \frac{d}{dy}[\eta \frac{d\phi}{dy}] + S_u \tag{17}$$

In the above equation, ϕ, η and S_u are a general specific property (e.g. *T*, *u*,*v* , etc), diffusion coefficient and source term, respectively. The finite volume integration of equation (17) over the control volume surrounding point P (see also Fig. 2) yields [58]:

$$\begin{aligned} &F_e\phi_e - F_w\phi_w + F_n\phi_n - F_s\phi_s = \\ &D_e(\phi_E - \phi_P) - D_w(\phi_P - \phi_W) + D_n(\phi_N - \phi_P) - D_s(\phi_P - \phi_S) \end{aligned} \tag{18}$$

where $F_i = (\rho u)_i \Delta A_i$ with $\Delta A_i = \Delta x = \Delta y$ and $D_i = \eta_i \Delta y / \Delta x = \eta_i \Delta x / \Delta y$ denotes the convection and diffusive flux terms cross the cell boundaries, respectively. By taking into account the direction of the local velocity field ($\mathbf{u}^+ > 0$ or $\mathbf{u}^- < 0$), the values of the property ϕ across the cell faces (ϕ_e, ϕ_w, ϕ_n and ϕ_s) can be approximated as:

For the positive flow direction ($\mathbf{u}^+ > 0$)

$$\begin{cases} \dfrac{\phi_e - \phi_W}{\phi_E - \phi_W} = \mathrm{K}_f(\Phi^+_{c,e}), & \Phi^+_{c,e} = (\phi_P - \phi_W)/(\phi_E - \phi_W) \\ \dfrac{\phi_w - \phi_{WW}}{\phi_P - \phi_{WW}} = \mathrm{K}_f(\Phi^+_{c,w}), & \Phi^+_{c,w} = (\phi_W - \phi_{WW})/(\phi_P - \phi_{WW}) \\ \dfrac{\phi_n - \phi_S}{\phi_N - \phi_S} = \mathrm{K}_f(\Phi^+_{c,n}), & \Phi^+_{c,n} = (\phi_P - \phi_S)/(\phi_N - \phi_S) \\ \dfrac{\phi_s - \phi_{SS}}{\phi_P - \phi_{SS}} = \mathrm{K}_f(\Phi^+_{c,s}), & \Phi^+_{c,s} = (\phi_S - \phi_{SS})/(\phi_P - \phi_{SS}) \end{cases} \tag{19}$$

By adding and subtracting the gradient ratios of $\Phi^+_{c,e}$, $\Phi^+_{c,w}$, $\Phi^+_{c,n}$ and $\Phi^+_{c,s}$ in/from the right hand side of the above equation, the unnormalized form of Eq. (19) can be written as:

For the positive flow direction ($\mathbf{u}^+ > 0$)

$$\begin{cases} \phi_e = \phi_P + [-\Phi^+_{c,e} + \mathrm{K}_f(\Phi^+_{c,e})] \times (\phi_E - \phi_W), & \Phi^+_{c,e} = (\phi_P - \phi_W)/(\phi_E - \phi_W) \\ \phi_w = \phi_W + [-\Phi^+_{c,w} + \mathrm{K}_f(\Phi^+_{c,w})] \times (\phi_P - \phi_{WW}), & \Phi^+_{c,w} = (\phi_W - \phi_{WW})/(\phi_P - \phi_{WW}) \\ \phi_n = \phi_P + [-\Phi^+_{c,n} + \mathrm{K}_f(\Phi^+_{c,n})] \times (\phi_N - \phi_S), & \Phi^+_{c,n} = (\phi_P - \phi_S)/(\phi_N - \phi_S) \\ \phi_s = \phi_S + [-\Phi^+_{c,s} + \mathrm{K}_f(\Phi^+_{c,s})] \times (\phi_P - \phi_{SS}), & \Phi^+_{c,s} = (\phi_S - \phi_{SS})/(\phi_P - \phi_{SS}) \end{cases} \tag{20}$$

likewise, for the negative flow direction, the values of the property ϕ across the cell faces (ϕ_e, ϕ_w, ϕ_n and ϕ_s) may be written as:

For the negative flow direction ($\mathbf{u}^- < 0$)

$$\begin{cases} \dfrac{\phi_e-\phi_{EE}}{\phi_P-\phi_{EE}}=\mathrm{K}_f(\Phi^-_{c,e}), & \Phi^-_{c,e}=(\phi_E-\phi_{EE})/(\phi_P-\phi_{EE}) \\ \dfrac{\phi_w-\phi_E}{\phi_W-\phi_E}=\mathrm{K}_f(\Phi^-_{c,w}), & \Phi^-_{c,w}=(\phi_P-\phi_E)/(\phi_W-\phi_E) \\ \dfrac{\phi_n-\phi_{NN}}{\phi_P-\phi_{NN}}=\mathrm{K}_f(\Phi^-_{c,n}), & \Phi^-_{c,n}=(\phi_N-\phi_{NN})/(\phi_P-\phi_{NN}) \\ \dfrac{\phi_s-\phi_N}{\phi_S-\phi_N}=\mathrm{K}_f(\Phi^-_{c,s}), & \Phi^-_{c,s}=(\phi_P-\phi_N)/(\phi_S-\phi_N) \end{cases} \tag{21}$$

Similarly, by adding and subtracting the gradient ratios of $\Phi^-_{c,e}$, $\Phi^-_{c,w}$, $\Phi^-_{c,n}$ and $\Phi^-_{c,s}$ in/from the right hand side of the above equation, the unnormalized form of Eq. (21) can be rewritten as:

For the negative flow direction ($\mathbf{u}^- < 0$)

$$\begin{cases} \phi_e=\phi_E+[-\Phi^-_{c,e}+\mathrm{K}_f(\Phi^-_{c,e})]\times(\phi_P-\phi_{EE}), & \Phi^-_{c,e}=(\phi_E-\phi_{EE})/(\phi_P-\phi_{EE}) \\ \phi_w=\phi_P+[-\Phi^-_{c,w}+\mathrm{K}_f(\Phi^-_{c,w})]\times(\phi_W-\phi_E), & \Phi^-_{c,w}=(\phi_P-\phi_E)/(\phi_W-\phi_E) \\ \phi_n=\phi_N+[-\Phi^-_{c,n}+\mathrm{K}_f(\Phi^-_{c,n})]\times(\phi_P-\phi_{NN}), & \Phi^-_{c,n}=(\phi_N-\phi_{NN})/(\phi_P-\phi_{NN}) \\ \phi_s=\phi_P+[-\Phi^-_{c,s}+\mathrm{K}_f(\Phi^-_{c,s})]\times(\phi_S-\phi_N), & \Phi^-_{c,s}=(\phi_P-\phi_N)/(\phi_S-\phi_N) \end{cases} \tag{22}$$

by substituting Eqs. (20) and (22) into the Eq. (18) and incorporating the notation of the Upwind scheme, the follows stable algebraic equation can be obtained:

$$\begin{aligned} &a_P\phi_P=a_W\phi_W+a_E\phi_E+a_S\phi_S+a_N\phi_N+S_u \\ &a_W=D_w+\max(F_w,0) \\ &a_E=D_e+\max(-F_e,0) \\ &a_S=D_s+\max(F_s,0) \\ &a_N=D_n+\max(-F_n,0) \\ &a_P=a_W+a_E+a_S+a_N+(F_e-F_w)+(F_n-F_s) \end{aligned} \tag{23}$$

One of the main advantages of the above equation is that, the central and neighbour coefficients a_P, a_W, a_E, a_S and a_N are always positive which makes the implicit scheme unconditionally stable, thereby satisfying the needs for conservativeness, and transportiveness as highlighted by

Versteeget et al. [58]. The contribution arising from the additional piecewise NV function is introduced through the source term (S_u) as:

$$
\begin{aligned}
S_u = & -\gamma_e F_e[-\Phi^+_{c,e} + \mathrm{K}_f(\Phi^+_{c,e})]\times(\phi_E - \phi_W) \\
& +\gamma_w F_w[-\Phi^+_{c,w} + \mathrm{K}_f(\Phi^+_{c,w})]\times(\phi_P - \phi_{WW}) \\
& -\gamma_n F_n[-\Phi^+_{c,n} + \mathrm{K}_f(\Phi^+_{c,n})]\times(\phi_N - \phi_S) \\
& +\gamma_s F_s[-\Phi^+_{c,s} + \mathrm{K}_f(\Phi^+_{c,s})]\times(\phi_P - \phi_{SS}) \\
& -F_e(1-\gamma_e)[-\Phi^-_{c,e} + \mathrm{K}_f(\Phi^-_{c,e})]\times(\phi_P - \phi_{EE}) \\
& +F_w(1-\gamma_w)[-\Phi^-_{c,w} + \mathrm{K}_f(\Phi^-_{c,w})]\times(\phi_W - \phi_E) \\
& -F_n(1-\gamma_n)[-\Phi^-_{c,n} + \mathrm{K}_f(\Phi^-_{c,n})]\times(\phi_P - \phi_{NN}) \\
& +F_s(1-\gamma_s)[-\Phi^-_{c,s} + \mathrm{K}_f(\Phi^-_{c,s})]\times(\phi_S - \phi_N)
\end{aligned}
\tag{24}
$$

It is worth to mention that, the term S_u in the above equation is known as "*deferred correction*" which contains negative coefficients arising from the implementation of the high resolution bounded (e.g. TVD, NVD) or unbounded (e.g. QUICK) differencing schemes [58]. The existence of the *deferred correction* in the discretized equation can successfully prevent the occurrence of numerical instability while ensuring the desired order of accuracy and monotonic behaviour. In Eq. (24), γ_i is the dummy variable which depends on the direction of the flow given as:

$$
\begin{aligned}
&\gamma_e = 1 \text{ if } F_e > 0, \quad \gamma_e = 0 \text{ if } F_e < 0 \\
&\gamma_w = 1 \text{ if } F_w > 0, \quad \gamma_w = 0 \text{ if } F_w < 0 \\
&\gamma_n = 1 \text{ if } F_n > 0, \quad \gamma_n = 0 \text{ if } F_n < 0 \\
&\gamma_s = 1 \text{ if } F_s > 0, \quad \gamma_s = 0 \text{ if } F_s < 0
\end{aligned}
\tag{25}
$$

Before closing this section, it is important to underline that, in order to minimize the excessive use of *"IF"* in computer programming of the proposed scheme and to avoid the singularity problem in denominator of the subdomains (i.e. $\Phi_c < 0$, $0 \le \Phi_c \le 0.4$, $0.4 < \Phi_c \le 1.0$ and $1.0 < \Phi_c$) in Eq. (16), an proper treatment should be applied to each sub-domain of NV function. To this end, one

can multiply the numerator and denominator of gradient ratio (Φ_c) with the value of its denominator (e.g. $\Phi_c = A/B = A\times B/B^2$). For instance, the local gradient ratio of $\Phi^+_{c,w}$ on the West cell face for the positive flow direction can be written as:

$$\Phi^+_{c,w} = \frac{(\phi_W - \phi_{WW})}{(\phi_P - \phi_{WW})} = \frac{(\phi_W - \phi_{WW})}{(\phi_P - \phi_{WW})} \times \frac{(\phi_P - \phi_{WW})}{(\phi_P - \phi_{WW})} = \frac{(\phi_W - \phi_{WW}) \times (\phi_P - \phi_{WW})}{(\phi_P - \phi_{WW})^2} \tag{26}$$

By applying the above procedure on the sub-domains of Eq. (16), one can obtain:

For sub-domain ($\Phi^+_{c,w} < 0$)

$$\frac{(\phi_W - \phi_{WW}) \times (\phi_P - \phi_{WW})}{(\phi_P - \phi_{WW})^2} < 0 \quad \rightarrow \quad (\phi_W - \phi_{WW}) \times (\phi_P - \phi_{WW}) < 0$$

For sub-domain ($0 \le \Phi^+_{c,w} \le 0.4$)

$$0 \le \frac{(\phi_W - \phi_{WW}) \times (\phi_P - \phi_{WW})}{(\phi_P - \phi_{WW})^2} \le 0.4 \quad \rightarrow \quad 0 \le (\phi_W - \phi_{WW}) \times (\phi_P - \phi_{WW}) \le 0.4(\phi_P - \phi_{WW})^2$$

For sub-domain ($0.4 < \Phi^+_{c,w} \le 0.6$)

$$0.4 \le \frac{(\phi_W - \phi_{WW}) \times (\phi_P - \phi_{WW})}{(\phi_P - \phi_{WW})^2} \le 0.6 \rightarrow 0.4(\phi_P - \phi_{WW})^2 \le (\phi_W - \phi_{WW}) \times (\phi_P - \phi_{WW}) \le 0.6(\phi_P - \phi_{WW})^2 \tag{27}$$

For sub-domain ($0.6 < \Phi^+_{c,w} \le 1$)

$$0.6 \le \frac{(\phi_W - \phi_{WW}) \times (\phi_P - \phi_{WW})}{(\phi_P - \phi_{WW})^2} \le 1 \rightarrow 0.6(\phi_P - \phi_{WW})^2 \le (\phi_W - \phi_{WW}) \times (\phi_P - \phi_{WW}) \le (\phi_P - \phi_{WW})^2$$

For sub-domain $1.0 < \Phi^+_{c,w}$

$$1.0 < \frac{(\phi_W - \phi_{WW}) \times (\phi_P - \phi_{WW})}{(\phi_P - \phi_{WW})^2} \quad \rightarrow \quad (\phi_P - \phi_{WW})^2 < (\phi_W - \phi_{WW}) \times (\phi_P - \phi_{WW})$$

Note that, the similar procedure should be applied to other three faces of computational cell (i.e. $\Phi^-_{c,w}$, $\Phi^\pm_{c,e}$, $\Phi^\pm_{c,n}$ and $\Phi^\pm_{c,s}$). Finally, as mentioned before, there is a one-to-one relationship between Sweby and NV diagrams so that by substituting Eq. (16) into the Eq. (15), the corresponding flux-limiter function in Sweby diagram can be derived as:

$$\psi(r)=\begin{cases}\dfrac{(|r|+r)\times(-497r^3+384r^2+384r+128)}{128(1+r)^3} & r\le\dfrac{2}{3}\\ \dfrac{r+3}{4} & \dfrac{2}{3}<r\le\dfrac{3}{2}\\ \dfrac{1504r^3+2337r^2+1637r+429}{752(1+r)^3} & r>\dfrac{3}{2}\end{cases} \tag{28}$$

More details related to the implementation of the above flux-limiter function for the discretization of the governing equations in the context of TVD Sweby diagram can be found in Ref [53].

5. Validation

The effectiveness and performance of the newly developed third-order NVD bounded scheme alongside the Modified PISO algorithm (MPISO) in dealing with the multi-fluid flows with complex morphological changes (i.e. merging, deforming, flattening, twisting, and filamentation) are systematically demonstrated against five challenging benchmark problems. As schematically portrayed in Fig. 1, the first benchmark problem is the well-known dam-break flow over the horizontal dry bed (case 1) where due to the formation of reverse plunging wave, interface smearing arising from false-diffusion errors is likely to appear within the computational domain, making it a good candidate to assess the robustness of the proposed NVD-TVD scheme. The modeling of oil spill from the damaged container is considered as a second canonical test case (case 2) to verify the versatility of the enhanced VOF model in handling immiscible multi-fluid incompressible flows with continuous bending and twisting deformation scenarios. Two-phase Rayleigh-Taylor Instability (RTI) problem is reproduced as a third benchmark problem (case 3) where owing to the appearance of the secondary Kelvin-Helmholtz Instability phenomenon, the RTI evolution exhibits strong non-linearity and significant interface deformation, rendering it more suitable to challenge the capability of the enhanced VOF model in resolving the sharp gradients near the interface. The fourth and fifth examples under consideration are classical single

rising bubbles (case 4) and the collision of two rising bubbles (case 5) where due to the presence of surface tension force, the phenomena so-called filamentation, interface coalescence/rupture together with droplet detachment are likely to take place within the fluids domain, thereby making them more suitable to further evaluate the applicability of ELVIRA and MPISO models in reconstructing moving interfaces and alleviating non-physical velocity fluctuation in vicinity of the material discontinuities. The predicted results are presented in forms of volume fraction and pressure contours together with the time history of the interface positions.

5.1.Dam break over a dry bed (Case 1)

The first benchmark problem considers a dam-break wave advancing in a straight dry flume corresponding to the experiments conducted by Lobovský et al. [68]. This small-scale laboratory experiment was also numerically examined and reproduced by Zhang et al. [69] and Park et al. [70] using the Eulerian and Lagrangian methods (i.e. VOF and SPH). As schematically shown in Fig. 1, the channel is rectangular in shape with dimension size of $L = 3.22m$ and $D = 1.2m$ where a water column at standstill condition with height and width of $W = 1.2m$ and $H = 0.6m$ is initially confined in the left part of the enclosure ($\varphi = 1.0$) while the rest of the flume is considered to be totally drained (i.e. filled with the air as the second phase, $\lambda = 1.0$). No-slip velocity boundary condition is applied on the all solid walls and the effects of surface tension ($\sigma = 0.071\ Kgs^{-2}$) and viscosity ($\mu_{Water} = 855\times10^{-6} kg\, m^{-1}s^{-1}$ and $\mu_{Air} = 184\times10^{-7} kg\, m^{-1}s^{-1}$) are taken into consideration. The physical density of air and water are set equal to $\rho_{Air} = 1.0\, kgm^{-3}$ and $\rho_{Water} = 997\, kgm^{-3}$, respectively. Three pressure sensors ($h_{R1} = 0.03m$ and $h_{R2} = 0.16m$) for monitoring the pressure variation are deployed on the downstream wall while time histories of water level height are recorded at three different stations ($l_1 = 0.6m, l_2 = 2.228m$ and $l_3 = 2.725m$). Before proceeding

further, it is worth mentioning that, since two fluid are involved in the present canonical test case (i.e. air and water), Eq. (4) alongside the Eq. (6) namely $\varphi + \lambda = 1$ are utilized for capturing the moving interface while Eqs. (7) and (8) are employed for the approximation of the physical properties of working fluid across the whole enclosure. The simulation is performed on the uniform grid resolution of 750×375 and the predicted results in forms of volume fraction field and pressure contours are portrayed in Fig. 3. As carefully documented and fundamentally scrutinized by Park et al. [70] and Issakhov et al. [71], the morphological evolution and free-surface dynamics of dam failure phenomenon can be differentiated into four distinct stages . Stage 1 encompass shoaling event where under the action of the gravity force, the stored water collapses downward to form the flooding wave. Later, the stress wave propagates freely over the initially dry bed until the bore reaches the downstream wall. Stage 2 accounts for the liquid-solid interaction where due to the impingement of wave front onto the end wall, an intensive up-willing jet is formed within the computational domain. Stage 3 involves the significant deterioration in the momentum of the ascending jet under restoring action of the gravity force which manifests itself through the emergence of the reverse plunging breaker and subsequent air pocket formation. The last stage covers the post-breaking regime which is characterized by complex reconnection process of rolling jet from the water surface. Note that, in the violent free-surface flows, this stage is typically accompanied by the initiation of splash-up scenario and subsequent air-water mixing. Based on the above arguments, it is evident from Fig. 3 that, immediately after opening the virtual gate, the water column falls down over a horizontal duct due to gravity and spreads freely towards the downstream region. As time elapses ($0 \le T \le 2.389$), the resultant steep wave undergoes sever elongation which indicates that it is predominantly driven by both shear and gravity forces. At this juncture, it should be mentioned that, this stage of the evolution is also governed by the surface

wave motion and internal recirculating vortices which develop longitudinally beneath the free surface. Later, the fluid accelerates and eventually the tip of the surge wave touches the opposite wall with maximum velocity of $u_f \approx 2\sqrt{\mathbf{g}H}$ (supercritical flow) which is twice the theoretical wave celerity ($c_0 = \sqrt{\mathbf{g}H}$) [70,72]. After impingement onto the rigid wall, the water front toe starts to fragment and deflect upward, leading to the appearance of the rising jet in that area. It is not surprising that, as a consequence of the abrupt alteration in the direction of the main flow, the quasi stagnation point with related fluid trapping phenomenon are appeared in the impact zone. This flow pattern which corresponds to the initiation of the first peak pressure ($P_{\max,R1} = 1.822$) at $T = t\sqrt{g/H} = 2.547$ (see also Figs. 4-6) also generates a secondary clockwise circulation which is responsible for the unsteady *flow bifurcation* in the bottom-right corner of the enclosure where quasi-hydrostatic pressure distribution is dominated [73]. It should be noted that from the ocean engineering viewpoint, the first impact pressure and its impulse force are of great importance for the optimization design of critical infrastructure facilities, offshore structures and bridge pier to mitigate detrimental effects of tsunami hazards and coastal flooding [74,75]. However, as time progresses ($2.389 < T \le 4.779$), due to the steady oncoming flow and retarding effects of gravity force, the intensity of the CW rotating eddy declines and consequently it starts to weaken and grow in size. Meanwhile, the motion of the reflected wave slows down and begins to detach from the stationary rigid wall which implies that the adverse pressure gradient and third stage of the dam break evolution are coming into the picture. In fact, the development of this plunging breaker is closely related to the separation of boundary layer and attenuation of the inertial effects which cause the ascending solitary jet to return and fold back into the main water body. After the run-up and run-down the cycle, the newly generated rolling jet hits the ambient water and forms the second stress wave which rebounds from the wetted bed and travels obliquely towards the

upstream region. Accompanied by this morphological change, the second impact pressure ($P_{\max,R1}=0.884, P_{\max,R2}=0.644$) at $T=t\sqrt{g/H}\approx 6.348$ and a closed loop entrapping air are developed in the immediate vicinity of the plunging point which mark the inception of the fourth stage. Note that, during this process, one part of kinetic energy is used from the water surface to build up the second rising jet and rest of the mechanical energy is dissipated viscously by the mean velocity/pressure gradients to create the second pressure shock [76].

Qualitative and quantitative comparison of obtained results with numerical works of Lobovský et al. [68], Zhang et al. [69] and Park et al. [70] in Figs. 4-6 show that the global characteristics of the dam break flow in terms of the surge front location (X_{front}), jet amplification, re-entering of the overturning jet into the water surface, impact position and cavity formation are well predicted by the proposed VOF model, verifying the accuracy of the numerical modifications. Combining the findings of Figs. 4-6, one can observe that, the pressure field across the interface is smooth and free of spurious fluctuations which in turn prove the robustness and effectiveness of the proposed MPISO algorithm in dealing with the physical discontinuities in multiphase flows with high density contrast. However, the close inspection of the results in Figs. 5 and 6 reveal that, there exists some level of discrepancies between outcomes of the proposed model with those predicted by SPH model [69] which can be attributed to the absence of the secondary phase (i.e. air) in the classical Lagrangian particle method and partially due to the implementation of the low-order differencing scheme used for the discretization of the governing equations in the SPH framework. Finally, it can be seen that, although the time history of the impact pressure load monitored by sensor 2 is slightly overestimated, the global trend satisfactory matches the experimental measurements provided in Refs [77,78].

5.2.Oil spill from the stationary damaged container (Case 2)

Oil leakages from the damaged tank as a major potential hazard to the ocean environment can result in extensive damage to marine life and human health, causing tremendous economic loss [79]. During the last decade, a large number of theoretical, numerical and experimental studies have been devoted to elucidating the underlying mechanisms behind the oil spills [79]. However, as highlighted by Jeong et al. [80], the prediction of the spread of crude oil in the early stages is of a great importance to analyze or eliminate its environmental impacts. Thus, in this subsection, the problem of oil spill from the damaged container introduced by Duan et al. [81,82] in context of Lagrangian MPS model is reproduced here using the Eulerian VOF model. As portrayed in Fig. 1, the calculation is carried out in the rectangular container with dimensional size of $L = 0.6m$ and $D = 0.3m$ where a column of oil ($\mu_{Oil} = 0.05 kg\, m^{-1}s^{-1}$ and $\rho_{Oil} = 897\, kgm^{-3}$) with width and height of $W = 0.1m$ and $H = 0.25m$ is initially stored in the left side of the enclosure and is connected to the downstream wet bed with initial water depth of $B = 0.4H = 0.1m$ ($\mu_{Water} = 0.001 kg\, m^{-1}s^{-1}$ and $\rho_{Water} = 1000\, kgm^{-3}$). The rest of the enclosure is occupied by air as a third phase with nominal density and viscosity of $\mu_{Air} = 1.7 \times 10^{-5} kg\, m^{-1}s^{-1}$ and $\rho_{Air} = 1.0\, kgm^{-3}$, respectively. The simulation is performed on the uniform grid resolution of 600×300 and the surface tension coefficient is set as $\sigma = 0.0152\ Kgs^{-2}$. The primary and secondary phases (Oil and Water) are initially separated by the presence of rigid wall which is installed at $x = 0.1m$. The opening length of the leaking hole is $R_1 = 0.08H = 0.02m$ and its distance from the bottom wall of the container is set as $R_2 = 0.16H = 0.04m$. The snapshots of the predicted results at five different non-dimensional time instants ($T = t\sqrt{g/H}$) are displayed in Fig. 7. Generally, the floating processes of oil spilling from the ruptured tank and its migration toward the free-surface area under the action of the bouyancy force can be splitted into two distinct stages namely: (I)

drifting (plume jet stage) and (II) rising (buoyancy diffusion stage). In drifting stage, due to the existence of pressure gradient and hydraulic imbalances, the oil phase starts to penetrate into the water phase and propagates horizontally until the submerged oil parcel reaches its maximum horizontal distance. This mechanism results in the significant attenuation in the magnitude of the kinetic energy and considerable augmentation in the hydraulic balance of the system. However, due to the drag force and hydraulic resistances between interacting fluids, the initial momentum of the system is exhausted and consequently the motion of the oil front decelerates. During the deceleration period, the buoyancy force induced by the density gradient causes the oil phase to change its direction and deviates upward towards the free-surface area where high level of mixing process occurs. Based on the above description, one can observed from Fig. 7 that, after opening the virtual breach, owing to the head difference between primary and secondary phases, the oil jet flows out from the cargo tank through the internal hole and moves horizontally toward the downstream area. During this process, because of the interaction between leaked oil and surrounding still water, a pair of recirculating eddies are developed on both sides of the plume, leading to the appearance of the mushroom-like twin-vortex structure inside the container. As time progresses, the horizontal-displacement motion and migration velocity of oil flow slow down and tails of the oil plume start to fold inward. This mechanism which is mainly attributed to the small density differences (i.e. low Atwood number, $At = (\rho_{Water} - \rho_{Oil})/(\rho_{Water} + \rho_{Oil}) \approx 0.055$) between oil and water fluids, causes the transport phenomenon becomes unstable to the Kelvin-Helmholtz Instability. At the same time, under the rising action of the buoyancy force, the mixture oily water spreads obliquely toward the free-surface region and some secondary vortices are formed on sides of advancing oil wave. The corresponded pressure field shows that this process is accompanied by the moderate enhancement in the hydrostatic pressure distribution and the establishment of the

surging wave which travels toward the downstream end wall. Meanwhile, the small-scale breaking/collapsing wave (i.e. plunging vortex) is appeared on rear of the tidal surge and consequently the interfaces undergoes sever deformation with twisting. The comparison of the obtained results from the current study with those reported by in Fig. 8 demonstrates that, the topological characteristics and hydrodynamic peculiarities of the oil spill is well predicted and good agreements are found between two numerical outcomes. The enlarged views of the oil-water interface at five different snapshots show that, the sharpness of the interface region is well preserved, certifying the accuracy and capability of the proposed high-order NVD scheme in minimizing false-diffusion errors in strongly coupled multiphase problems. Moreover, the smoothness of the pressure contours across the interfaces in Fig. 7 proves that, the velocity-pressure coupling is efficiently treated by the proposed MPISO algorithm. Finally, the time variations of oil and water level heights at three different sites are provided in Fig. 8 as additional information which have not been reported in Refs [81,82].

5.3.Two-phase Rayleigh-Taylor Instability (Case 3)

As highlighted earlier, the development of Rayleigh-Taylor Instability (RTI) can provide adequate complexities to challenge the stability and consistency of existing interface-capturing methods. Thus, a single-mode two-phase RTI problem pioneered by Zuzio et al. [83] in the context of Level-Set model and reproduced by Cao et al. [84], Haghshenas et al. [85] and Ling et al. [86] using the Coupled Level-Set-VOF (CLSVOF) is chosen here as the third benchmark test case. As schematically shown in Fig. 1, this canonical example consists of two immiscible fluids with nominal densities of $\rho_H = 1.225 kgm^{-3}$ and $\rho_L = 0.1694 kgm^{-3}$ which are initially enclosed inside a rectangular domain of $[H, 4H]$ with $H = 1.0\, m$ being width of the enclosure. Both fluids have the

same dynamic viscosity of $\mu_H = \mu_L = 0.00313\ kg\,m^{-1}s^{-1}$ and the initial perturbation across the horizontal axial midline of the cavity is defined by a cosine wave of $y = 2.0 + 0.05\cos(2\pi x)$. According to the aforementioned physical properties, the non-dimensional Reynolds and Atwood numbers may be defined as $\mathrm{Re} = \rho_H H\sqrt{gH}\,/\,\mu_H = 1225.81$ and $At = (\rho_H - \rho_L)/(\rho_H + \rho_L) = 0.757$ with $U = \sqrt{gH}$ denotes the reference velocity. The numerical simulation is performed on uniform 250×1000 grid resolution. Periodic boundary condition is applied to the vertical walls whereas no-slip impermeable velocity boundary condition is enforced on the horizontal walls. Similar to Ref. [85], the effects of surface tension force is taken into consideration ($\sigma = 0.001337\,Nm^{-1}$), giving rise to the Weber number of $We = \rho_H gH^2/\sigma = 8988.22$. The transient evolution of the RTI at different dimensionless time instants ($T = t\sqrt{g/H}$) is plotted in Fig. 9. Generally, due to the small perturbation and spatial-density contrast across the interface, the hydraulic equilibrium between two fluids destabilizes and lighter fluid moves upward in form of bubble and denser fluid falls down as spikes, leading to the formation of two counter-rotating vortices within the computational domain ($0 \le T \le 1.44$). With the continuous development of RTI process, the disturbance increases and consequently the tails of the spikes start to roll inward giving rise to the appearance of vortex shedding. As time progresses ($1.44 < T \le 1.879$), the strength of the fluid flow intensifies and thus a significant twisting of the interface occurs, indicating the onset of Kelvin-Helmholtz Instability (KHI) [87]. In fact, the appearance of the KHI can be regarded as the strong interaction between buoyancy and shear (viscous) forces which causes the interface to stretch and fold into very complicated shape. As the heavy and lighter fluids propagate further towards the boundary layers of bottom and top walls ($1.879 < T \le 2.818$), the acceleration of the mixing process declines and consequently dual-mode spiral vortices are formed in close proximity

of the falling spikes which causes the tiles of the heavy fluid to transform into the thin filaments. This flow pattern obviously proves the considerable amplification in KHI and nonlinearity of the flow regime which are also responsible for augmented interfacial deformation.

The qualitative and quantitative comparison of the predicted results from the current study with numerical work of Cao et al. [84] in Figs. 9 and 10 vividly demonstrate the accuracy and robustness of the proposed VOF model in capturing the topology of complex spatial scenes and key features of the RTI development. Thanks to the proposed third-order NVD convection scheme alongside the MPISO algorithm, the obtained results on the uniform grid spacing are in satisfactory agreement with results of Coupled Level-Set-VOF (CLSVOF) aided by Local Adaptive Mesh Refinement (LAMR). In fact, this observation clearly confirm the robustness and effectiveness of the proposed modification and superiority of the present consistent/conservative VOF method over the CLSVOF in handling multi-fluid flows with large deformation and fragmentation without applying additional treatment such as LAMR. The zoomed-in views of the interface at two different time instants illustrate that the interface thickness is efficiently restricted to the maximum 2-3 grid spacings throughout the evolution which is the strong indication of the alleviating false-diffusion errors.

5.4. Single rising bubble (Case 4)

The transient evolution of the single rising bubble in quiescent liquid is examined here as a third benchmark problem. The initial configuration of the benchmark test case (t=0) is identical with numerical work of Zhao et al. [88] and Yu et al. [89] where a circular bubble ($R_0 = 0.25m$) with

nominal density and viscosity, of $\rho_L = 2.0\,Kgm^{-3}$, $\mu_L = \sqrt{2}/100\ Kgm^{-1}s^{-1}$ is centered at $[0.5m, 0.37m]$ in a rectangular duct $[1m, 1.62m]$ filled with heavier fluid with physical properties of $\rho_H = 10.0\,Kgm^{-3}$ and $\mu_H = \sqrt{2}/20\ Kgm^{-1}s^{-1}$. The morphological alterations and hydrodynamic behavior of the transport phenomenon are governed by Reynolds and Weber numbers defined as $\mathrm{Re} = \rho_H \sqrt{g}(2R)^{3/2}/\mu_H = 100$ and $We = \rho_H g(2R)^2/\sigma = 200$, respectively. The no-slip boundary condition ($\mathbf{u} = 0$) is imposed on all rigid walls. The simulation is conducted on uniform 250×405 grid resolution and the effects of surface tension force ($\sigma = 0.05\,Nm^{-1}$) are taken into consideration. The temporal evolution of the shape of the bubble at different non-dimensional time instants ($T = t\sqrt{g/R}$) is depicted in Fig. 11. It can be seen that, in general, due to the existence of density gradient and buoyancy force, the bubble ascends freely in an upward direction while the heavy fluid moves downward along the vertical walls of the column to satisfy the need for mass-conservation. This mechanism leads to the development of a pair of counter-rotating streamwise vortices and wake shedding phenomenon near the rear of the bubble ($0 \le T \le 2.4$). As time evolves ($2.4 < T \le 5.52$), due to the presence of surface tension and viscous forces, the bubble undergoes moderate dynamical change to form a mushroom-shaped structure. This stage is also accompanied by the acceleration of the downward liquid jet that squeezes the bubble in the vertical direction, causing an increase in drag and a moderate reduction in bubble velocity. This mechanism with the aid of unsteady vortex shedding cause the tails of the bubble to fold back on itself and elongate in the *y* axis. The consequence of this folding is visible in Fig. 11 where the skirt-like shape starts to appear behind the rising bubble. After an early-stage acceleration ($5.52 < T \le 6.64$), the movement of the skirted bubble slows down and ultimately begins to evolve into cap- or disk-shaped structure. It is evident that, with further increase in time ($6.64 < T$), the thickness of the skirt decreases and

consequently a pair of long, thin, gas filaments is developed on peripheries of the bubble which eventually breaks apart, forming two small satellite bubbles in the wake area of the main bubble. A close inspection of Fig. 11 reveals that during the period of $T \le 4.48$, due to the effects of inertia and unbalanced forces, the bubble undergoes severe shape deformation whereas at $4.48 < T$ it tends to become more flatter and remain almost unchanged which indicates that the bubble starts to enter the terminal condition (or reach the terminal velocity) where all relevant forces acting on the bubble (i.e. drag, gravitational, and buoyant forces) are in equilibrium. It is interesting to compare the predicted results from the current work with those computed using the Level-Set and VOF methods by Zhao et al. [88] and Yu et al. [89]. It is evident from Fig. 12 that although both methods can efficiently predict the bubble growth deformation at the early stages ($0 \le T \le 4.0$), the present method do a much better job in handling complex interface rupture especially at the final stage of the nonlinear process where some secondary small daughter bubbles are emerged in the wake of a leading bubble ($4 < T \le 8$). The maximum position of the bubble front is compared with numerical work of Zhao et al. [88] in Fig. 12 and good agreement is found.

5.5.Merging of two rising bubbles (Case 5)

To further illustrate the validity and versatility of the proposed model in handling multiphase flows with large topological changes and interface coalescence, breakup and reconnections, the problem of merging of two rising bubbles subjected to an external acceleration is examined here. This challenging benchmark test case was originally introduced and analyzed by Smolianski [90] using the Level-Set method and then successfully reproduced by Vahabi et al. [91] by means of Smoothed Particle Hydrodynamics (SPH) method. The initial configuration of the geometry under consideration is displayed in Fig. 1 where a pair of circular bubbles with nominal diameters of $D_1 = 2R_1 = 0.4m$ and $D_2 = 2R_2 = 0.5m$ is sequentially arranged along the vertical centerline of the

enclosure at $Y_1 = 0.5H = 0.5m$ and $Y_2 = H = 1.0m$, respectively with $H = 1.0m$ being width of the enclosure. The physical properties of the primary and secondary phases are $\rho_H = 100\,kgm^{-3}$, $\rho_L = 1.0\ kgm^{-3}$, $\mu_H = 4.2857\,kg\,m^{-1}s^{-1}$ and $\mu_L = 0.42857\,kg\,m^{-1}s^{-1}$, respectively, giving rise to the density and viscosity ratios of $\rho_H/\rho_L = 100$ and $\mu_H/\mu_L = 10$. Based on the above pertinent parameters, the Reynolds and Bond numbers can be defined according to the radius of the larger bubble as $\mathrm{Re} = \rho_H(2R_2)\sqrt{2gR_2}/\mu_H = 35$ and $Bo = \rho_H g(2R_2)^2/\sigma = 250$. The surface tension force coefficient is set equal to $\sigma = 1.8\ Kgs^{-2}$. The no-slip boundary condition is applied on all rigid walls of the enclosure. The numerical calculation is carried out on the uniform structured grid (301×603) and predicted results in forms of volume fraction and pressure fields are depicted in Fig. 13 at three different non-dimensional time instants ($T = t\sqrt{g/D_2}$). As observed from the figure, during the early stage of the evolution ($0 \le T \le 0.48$), owing to the existence of density gradient between two phases, both bubbles go up simultaneously under the influence of the buoyancy force while the denser fluid descends downward in form of the liquid jets near the vertical walls to fulfill the need for mass conservation constraints. This flow pattern results in the formation of a pair of streamwise counter-rotating vortices with opposite signs which causes the shape of the circular bubbles to deform gradually into the saucer structure (or quasi-elliptical shape). As the smaller bubble moves in the wake of the larger bubble, the tails of the upper bubble folds inward and start to tightly envelop the skirted bubble. As time passes ($0.48 < T \le 0.96$), the lower bubble is gradually absorbed into the cavity below the leading bubble and subsequently the thickness of the liquid film between two bubbles gets thinner and thinner. A further scrutiny of the evolution in Fig. 13 reveals that, due to the invigorating effect of drag and viscous forces, the rise velocity of the leading bubble quickly reaches its terminal state and doesn't alter dramatically. On

the other hand, due to the presence of the wake region between two bubbles (which is responsible for decrement of drag force and increment of buoyancy force), the lower bubble is being accelerated and undergoes sever deformation [92]. However, as time progressed to the later stage of the development ($0.96 < T \leq 2.28$), the interface between liquid filament and rising bubbles ruptures and ultimately two bubbles meet each other and merge into a bubble cluster.

Qualitative comparison between results of the present study and those reported by Smolianski [90] and Vahabi et al. [91] in Fig. 13 displays that the whole rising, bursting and merging processes of two rising bubbles are well predicted by the improved VOF model. However, unlike the previous section, it is apparent that, the calculated results are more consistent with the SPH solution in comparison with the pure Finite-element Level-set model implemented by Smolianski [90]. These differences may be attributed to the implementation of the discretization schemes defined in the Euilerian and Lagrangian frameworks for solving the governing equations. More precisely, Smolianski [90] used the first-order Upwind scheme to discretize the convection term in the governing equation. However, as highlighted in section 4, this scheme cannot effectively resolve vorticity interface filamentation and are inherently characterized by false-diffusion errors, leading to the substantial loss of accuracy and excessive numerical diffusion around the bubble interface (i.e. interface smearing). Furthermore, the enlarged snapshot of the interface filamentation before merging of two bubbles at T=0.96 in Fig. 14 shows that, the thickness of the interface is successfully restricted to the maximum 2-3 grid spacings which in turn demonstrate the robustness and capability of the proposed NVD convection scheme in suppressing numerical diffusion and preserving the sharpness of the material discontinuities. Finally, it is worth to mention that, the time histories of the maximum position of the interface is given in Fig. 14 as a supplementary data which has not been reported in previous published references [90,91].

6. Results and discussion

Within the previous section, the accuracy and performance of the proposed modifications in handling multi-fluid flows with complex topological changes were systematically verified against a series of challenging test cases. In this part of the study, three new benchmark solutions namely (1) three-fluid Rayleigh-Taylor Instability (cases 6 and 7), (2) coalescence of two consecutive bubbles inside the partially filled enclosure (case 8), and (4) oil/water spilling from the damaged tank (cases 9 and 10) are simulated by the verified VOF model, aiming to provide a high-quality validation data for CFD simulations.

6.1.Three-phase Rayleigh-Taylor Instability (Cases 6 and 7)

The concept of the mixing of two immiscible fluids under the influence of gravity force was originally pioneered by Rayleigh [93] and later generalized and extended by Taylor [94]. However, as highlighted by Zhang [95] and Luo et al. [96], for a system with small Atwood number, the nonlinear evolution of Rayleigh-Taylor Instability can provide adequate complexities to challenge the existing Eulerian CFD approaches and shed more light on the general capabilities, advantages and also limitations of the open source and commercial softwares. Thus, within this section, two additional benchmark solutions namely three-phase Rayleigh-Taylor Instability will be introduced and then analyzed using the improved VOF method, aiming to establish the dataset not only for CFD validation but also for better understanding of underlying physics behind the Coupled Rayleigh-Taylor-Kelvin-Helmholtz Instability development.

As schematically illustrated in Fig. 1, the configuration consists of three distinct immiscible fluids with nominal densities of $\rho_H = 4.0$, $\rho_M = 2.0$ and $\rho_L = 1.0$ which are sequentially superposed from the upper to lower portions of the rectangular box with dimensional size of $[H, 3H]$ where

H=1m denotes the width of the container. The subscripts H, M and L represent the heavy, middle (or host) and lighter fluids, respectively. No-slip Dirichlet boundary condition is set on all rigid walls and the effects of surface tension force are not taken into account. The interfaces between two adjacent incompressible fluids in both cases in lower half of the enclosures are disturbed by cosine function given by $y_1 = 1.0 - 0.1 \times \cos(2\pi x)$ while the interface between Middle and Heavy fluids in upper half of the containers are perturbed by $y_2 = 2.0 - 0.1 \times \cos(2\pi x)$ and $y_2 = 2.0 + 0.1 \times \cos(2\pi x)$ in case 6 and case 7, respectively. The instability is described by two non-dimensional parameters namely Reynolds ($\mathrm{Re} = \rho_H H\sqrt{gH}\,/\,\mu_H = 420$) and Atwood ($At_{HL} = (\rho_H - \rho_L)/(\rho_H + \rho_L) = 3/5$) numbers where $\mu_H = 0.04$ stands for the dynamic viscosity of the dense fluid, respectively [97]. It is worthwhile mentioning that, contrary to the classical two-fluid Rayleigh-Taylor Instability problem (i.e. case 3), due to the presence of three fluids in present cases, two other Atwood numbers can be introduced based on the two adjacent fluids namely: $At_{ML} = (\rho_M - \rho_L)/(\rho_M + \rho_L) = 1/3$ and $At_{HM} = (\rho_H - \rho_M)/(\rho_H + \rho_M) = 1/3$. The kinematic viscosity of the working fluids is assumed to be identical ($\nu_H = \nu_M = \nu_L = 0.01$). Prior to the commencement of the calculations, it is important to note that, since three different phases are involved in cases 6 and 7, Eqs. (4) and (5) together with Eq. (6) (i.e. $\varphi + \lambda + \gamma = 1$) are employed for computing the volume fraction of each fluid while Eqs. (9) and (10) are used to approximate their physical properties. The simulation is carried out on uniform 300×900 meshes and predicted results at different non-dimensional time instants ($T = t\sqrt{g/H}$) are plotted in Figs. 15-18. As highlighted before, in generally, the hydrodynamic characteristics of RTI development can be classified into three distinct stages. Stage 1 encompass linear regime where the initial perturbation of the interfaces remains totally symmetrical with respect to the center of the enclosure and fluid

flow is primarily governed by buoyancy force [95]. Stage 2 involves the appearance of Kelvin-Helmholtz instability where shear/ viscous forces are comparable in magnitude to buoyancy force and fluid flow is characterized by formation of vortex shedding. Note that, this stage in the literature is commonly labeled as a weakly nonlinear regime of evolution where the symmetrical features begins to die out and drag force comes into play [98]. Stage 3 accounts for the fully non-linear regime and hydraulic equilibrium state where the fluid flow reaches its terminal velocity and mixing process takes place in a manner analogous to gradient diffusion [99]. According to the above explanation, one can observe from Fig. 15 that during the period of $0 \le T \le 2.52$, since the interfaces in case 6 are perturbed in the same directions and the solution is symmetric about the vertical midline of the container, the buoyancy force induced by density differences causes the lighter (ρ_L) fluid to ascend upward along the centerline of the enclosure while the denser (ρ_H) fluid falls down in close proximity of vertical wall. This mechanism leads to squeezeing of the host fluid (middle fluid, ρ_M). Meanwhile, as a consequence of mass conservation, the middle fluid (ρ_M) penetrates simultaneously into the vicinity fluids, resulting in the formation of a pair of spike-bubble structures within the enclosure. The corresponded velocity contours in Fig. 17 at T=0.945 show that, since the penetration rate of the heavy fluid into the middle fluid is similar to what happens between middle and lighter ones, the reversal and amplification of spike-bubble structures remain symmetrical about the horizontal midline of the domain which implies that, the flow regime is in the linear stage of perturbation growth. Beyond the initial stage ($2.52 < T \le 3.465$), however, the RTI exhibits the emergence of the rolling vortices and vortex shedding which signifies the inception of the Kelvin-Helmholtz Instability (KHI) and weakly non-linear flow regime, accordingly. It can be observed from Fig. 15 that, the transition from the linear flow regime to the weakly nonlinear one is also accompanied by significant enhancement in magnitude of the

velocity components which in turn explains the anticipated disappearance of symmetrical Hopf bifurcation structure and formation of the pseudo-terminal velocity [97]. More precisely, by close inspection of Fig. 17, on can found that, during the early stages of the evolution ($0 \le T \le 2.52$), the longitudinal flow velocity increases from $V = 0.0$ to 0.15, whereas this trend is continued by $V = 0.15$ to 1.3 during the second stage of the development ($2.52 < T \le 3.465$). These values vividly quantify the initiation of anisotropy and weak non-linearity in RTI mixing which are strong indications of the onset of a pseudo-terminal velocity. It is evident that during this period of evolution, the bubble of the lighter fluid gradually penetrates into the denser fluid, leading to the appearance of tulip-shaped structure (or harpoon-like pattern) within the computational domain. Meanwhile, the spikes of the dense fluid descend downward and start to envelop the ascending fluid, resulting in the emergence of amorphous-like structure. Note that, the terminology of spike and bubble was originally used by He et al. [87] and Tryggvason [100] to distinguish the movement of the ascending/descending fluids. However, as time proceeds ($3.465 < T \le 4.515$), the strength of the viscous and drag forces become more intense and subsequently the amount of fluid mixing and degree of nonlinearity increase. Under these circumstances, more and more secondary eddies are emerged along the sides of the spike-bubble structures and heterogeneity in the velocity distribution enhances. This mechanism is also responsible for the advection of plume vortices and hence any departure from the quasi-symmetry. The corresponded longitudinal velocity contours in Fig. 17 also reveal that, due to the imposition of the lower/upper no-through flow boundary, the intensity of fluid flow during the time period of $4.515 < T \le 5.25$ remains almost unaltered which conveys that the RTI development is reached its steady terminal velocity. This flow pattern is also consistent with the significant distortion of the interfaces in Fig. 15 where the RTI development

undergoes remarkable morphological changes such that the moving interfaces are elongated longitudinally and folded into very complicated structure.

However, Fig. 16 illustrates that by changing the orientation of the initial perturbation from $y_2 = 2.0 - 0.1\times\cos(2\pi x)$ to $y_2 = 2.0 + 0.1\times\cos(2\pi x)$ between the dense and host fluids in the upper half of the container, a different scenario takes place in case 7. As anticipated, during the linear stage of the interactions ($0 \le T \le 2.52$), the "*blob*" of dense fluid sinks towards the center of the enclosure while the light fluid moves upward in opposite direction under the influence of buoyancy force, resulting in the occurrence of plume-shaped structures. Meanwhile, the contracted host medium (ρ_M) begins to intrude simultaneously into the adjacent bulk fluids as the impulsive wave to fill the rooms that have been left by upwelling and downwelling plumes, giving rise to the formation of the second pair of spike-bubble structure in the right and left halves of the container. It can be seen from Fig. 18 that, the corresponded velocity distributions is totally symmetrical with respect to horizontal mid-plane of the cavity ($y = 1.5m$) which indicates that buoyancy/gravity forces are dominant and consequently the effects of drag and viscous forces are trivial. However, as time elapses ($2.52 < T \le 3.465$), the role of shear force gets more prominent and subsequently the interfaces become gradually unstable to Kelvin-Helmholtz shear Instability (KHI). To a certain extent, beside the four primary recirculating eddies, some small-scale inner vortices are provisionally appeared and disappeared at the edges of the spike-bubble structures, thereby causing the symmetrical feature to die out. In fact, the onset of the mushroom-shaped pattern together with the intensification of convective flow inside the cavity caused by inward/outward currents is strong indication of the deviation from the Linear Stability Theory (LST) [96] (see also Fig. 16). This physical mechanism which manifests itself through broadening and rolling-up/rolling-down of the interfaces is also responsible for invigorating drag force and initiation of quasi-terminal condition.

However, by comparing Figs. 15 and 16, one can deduce that, contrary to case 6 in which the working fluid freely travel toward the horizontal end walls, in case 7 due to the blockage and impeding effects of rising lighter fluid, the longitudinal interpenetration of the dense and lighter mediums is slowed down and ultimately crippled. It's apparent that with an increase in time ($3.465 < T \leq 5.250$), the tendency of the lighter fluid to obstruct and cover the falling heavy fluid is progressively invigorated until the RTI evolution reaches its terminal velocity and stagnation condition where the magnitude of the vertical velocity component doesn't change significantly. This assertion alongside the augmentation in mushrooming deformation of spike-bubble structures is well supported by Fig. 18 where due to the occurrence of the fluid trapping phenomenon and the establishment of the stagnation zone, the flow intensity remains nearly constant.

A scrutiny of Figs. 17 and 18 demonstrate that, the velocity fields across the density/viscosity jumps throughout the entire simulations in both cases are smooth and free of unphysical noises which vividly confirm promising robustness and applicability of the proposed semi-iterative MPISO algorithm in treating the velocity-pressure coupling in the incompressible multi-fluid flows. Furthermore, the zoomed-in views of the grids near the moving interfaces at two different time instants in Fig. 19 reveal that, the interfaces smearing is well suppressed and thickness/sharpness of the physical discontinuities is controlled and maintained to the maximum of 2-3 grid stencils, certifying the capability of proposed third-order NVD convection scheme in mitigating false diffusion errors due to the numerical truncation errors. Finally, as expected, the time histories of maximum and minimum positions of the interfaces in Fig. 19 show that, due to the mutual retarding effects of the ascending and descending fluids in case 7, the extreme positions of the lighter and denser fluids in this case are considerably lower than those of case 6. Take as an illustration at T=5.25, the maximum and minimum positions of the interfaces in case 6 are

respectively equal to $y_{\max,6}=2.871$ $y_{\min,6}=0.647$ whereas these values in case 7 are $y_{\max,7}=2.308$ $y_{\min,7}=1.037$. In addition, in case 6, the upwelling and downwilling fluids meet each other approximately at $T=2.70$ and $y_{H,L,6}=1.49$ whereas this event in case 7 is postponed at $T=3.17$ and $y_{H,L,7}=1.4$.

6.2. Coalescence of two consecutive bubbles inside the partially filled enclosure (Case 8)

Motion and coalescence of two rising bubbles within the rectangular enclosure partially filled with air and water is numerically investigated in this section as a first benchmark solution. Fig. 1 shows the schematic diagram of the numerical apparatus. As schematically displayed, the two-dimensional space domain is set as $[H,2H]$ where $H=1.0\,m$ is the width of the enclosure. Two bubbles with density and dynamic viscosity of $\rho_M=200$ and $\mu_M=2$ are initially centered at $X_{b1}=X_{b2}=0.5H=0.5\,m$, $Y_{b1}=0.5H=0.5\,m$ and $Y_{b2}=1.1H=1.1m$ from the bottom wall. The upper part of the enclosure is filled by air ($\rho_L=1.0$ and $\mu_L=0.01$) while the lower portion is occupied by water ($\rho_H=1000$, $\mu_H=10$) with initial depth of $W=1.6H=1.6\,m$. In the above physical properties the subscripts *L*, *M* and *H* denote the light, middle and dense fluids which here are air, oil and water, respectively. The flow regime is governed by Froude and Reynolds numbers defined as $Fr=U/\sqrt{gD}=1$ and $\mathrm{Re}=\rho_H D\sqrt{gD}/\mu_H=100$ where $U=\sqrt{gD}$ represents the reference velocity, respectively. The bubbles diameter is set to $D=2R=0.5\,m$. Similar to works of Pan et al. [101] and Garoosi et al. [102], for the sake of simplicity, the surface tension effect has not been considered in this study. The grid resolution used in present simulation corresponds to 350×700 grid points and no-slip boundary condition is applied on both vertical and horizontal walls. The evolution of the shape, lateral coalescence, breakup process of two rising bubbles

together with the corresponding velocity contours at various non-dimensional times ($T = t\sqrt{g / D}$) is shown in Figs. 20 and 21. According to the obtained results at beginning of the evolution ($0 \le T \le 1.48$), both bubbles travel upward simultaneously from rest under the influence of buoyancy force whereas the liquid film developed between the bubbles and the vertical walls of the chamber sinks downward due to the gravity force, leading to the formation of two primary recirculating cells together with some small secondary vortices within the computational domain. By this mechanism, a dramatic increase in rising velocity occurs as portrayed in Fig. 21. However, it can be seen that contrary to the morphological changes of individual Taylor bubble, the presence of the upper bubble in this case can remarkably influence the liquid flow around the lower bubble. That is to say, owing to the development of the inertia force and wake region beneath the leading bubbles, the trailing bubble is drawn into the wake of the upper one and consequently undergoes significant shear deformation/twisting as it continuously accelerates upward. This behavior can be attributed to the fact that, the hydrodynamic fluid flow formed by the upper bubble establishes a strong fluid shear effect on the lower bubble which causes the lower bubble to elongate significant in the longitudinal direction [103]. In fact, one can deduce that during this process, due to the upward flow generated by the wake of the leading bubble and two vortex rings around two bubbles, the wake region acts like an extensional flow which causes the trailing bubble accelerates and ascends faster than the leading one. As time goes on ($1.48 < T \le 2.48$), the underlying lower surface of the leading bubble is progressively indented and eventually deformed into an oblate ellipsoidal cap structure. Aided by this mechanism and the intensification of the adverse pressure gradients, the trailing bubble is ultimately enveloped by the leading bubble and deformed into the prolate-shaped structure. During this time period, the top portion of the leading bubble remains round shaped whereas the top part of the trailing bubble experiences notable distortion, that is, its tip first

narrows and then gradually widens transversely. One of the intriguing features to mention is that the region of high curvature occurs on the skirt of the trailing bubble where the second wake region appears which can be attributed to the vortical flow emerged in that area. The corresponding velocity contours in y-direction illustrate that, as a result of the distortion of the trailing bubble, some recirculation eddies with moderate intensity are established on the tails of the trailing bubble and liquid film around it becomes quite thick. It can be seen from Fig. 21, as the trailing bubble approaches the leading one, it decelerates and its velocity components decline which implies that the role of the viscous and drag forces become more prominent. As the system evolves with time ($2.48 < T \leq 4.0$), the distance between the bubbles decreases and ultimately the nose of the trailing bubble gets attached to the bottom of the leading one, indicating the inception of the merging process. The newly coalesced bubble moves upward until it meets the air-water surface area. Shortly after their collision, the liquid jet appears and starts to pinch off the united bubble and shreds satellite bubbles as displayed in Fig. 20. This observation is consistent with numerical findings of Kumar et al. [104] who highlighted the emergence of the skirted bubble and detachment of some daughter bubbles from the main body during the process of merging of two rising bubbles. Moreover, the appearance of two satellite bubbles at the lower extremities of the united bubble was also observed by Nagrath et al. [105] who numerically investigated the hydrodynamic characteristics of the bubble-bubble collision process in a quiescent liquid. However, as the time progress ($4.0 < T \leq 6.0$), the newly generated arrow-shaped jet gets much stronger and starts to split the bubbles from the bottom into two separate segments. This phenomenon is more pronounced at $T \geq 4.72$ where the bifurcation process occurs. The magnitude of the velocity components in x- and y-directions in Fig. 21 demonstrates that, the strength of the fluid flow decreases and approaches a constant value which indicates that the inertia is balanced by viscous

and drag forces. In fact this flow pattern conveys the initiation of terminal condition where the main important forces governing the motion of the bubbles (i.e. drag, gravity, buoyancy and viscous) are in hydrodynamic equilibrium.

The overall examination of the results shows that, the proposed numerical model preserves the smooth geometrical description of the moving interfaces involving stretching/tearing and successfully predicts the processes of propagation, approach, interaction, coalescence and eventual fragmentation/breakup of the united bubble. The zoomed-in view of interface at T=4.0 in Fig. 22 also confirms that the regularity of the moving interfaces are accurately maintained by the model. Thanks to the proposed third-order NVD convection scheme and Modified PISO algorithm (MPISO), both pressure and velocity fields are smooth and free of any spurious fluctuations. The time variation of maximum and minimum positions of rising bubbles before and after colliding is presented in Fig. 22b as supplementary data for the quantitative validation of the CFD codes.

6.3.Oil/Water spilling from the damaged tank (Cases 9 and 10)

Generally, the release of crude oils and petroleum products into the environment can take place due to equipment failure, human error, corrosion of container, third party activity and sabotage, causing huge environmental damage, serious economic impacts and major losses to the aquatic biodiversity [106]. Despite the acknowledgement of the importance of such phenomenon, little effort has been made to explore transient features of buoyancy-driven oil spills from the damaged pipes/containers [107]. Motivated by works of Jeong et al. [80], Zhu et al. [108] and Zhang et al. [109], the main objective of this sub-section is to establish two novel benchmark solutions in the context of multi-fluid flows, aiming to systematically scrutinize the morphological alterations of oil/water leakage from the fixed damaged tank. However, it is appropriate to say that, the main purpose is not to examine the transition between the regimes, but to visually demonstrate interface

breaking and air-entrapment events and determine the evolution of the interface location before, during and after the process of wave breaking.

The geometric parameters which are pertinent to the oil/water flow from the stationary container are schematically portrayed in Fig. 1. As it can be observed, the rectangular enclosure $[2H, H]$ (with H=1m being the height of the container) is occupied by three distinct immiscible fluids with nominal densities of $\rho_H = 1000$ (water), $\rho_M = 600$ (oil) and $\rho_L = 1.0$ (air). The Froude and Reynolds numbers are set to $Fr = U/\sqrt{gR} = 1$ and $\mathrm{Re} = R\sqrt{gR}/\nu = 77.618$ where $\mathbf{g} = 9.81$ and $R = 0.085m$ stand for the gravity acceleration and lateral opening length of the cargo tank vent, keeping the kinematic viscosity the same for the three fluids ($\nu_H = \nu_M = \nu_L = 0.001$). In both cases, the lower portion of the primary flume is occupied by liquid at rest (which is water in case 9 and oil in case 10) with initial depth of $D = 0.4m$. The cargo tank is positioned at $S_1 = 0.3m$ and $S_2 = 0.1m$ above the wetted bed while it is filled with the secondary liquid with free surface altitude and width of $L = W = 0.4m$. The rest of the enclosure is filled by air and no-slip boundary condition is applied on all rigid walls. The effect of surface tension force is neglected and the corresponding computational domain is discretized into a 700×350 uniform grid. Generally, as documented by Liu et al. [76], the jet plunging into liquid cushion generated by orifice can be divided into three distinct stages namely: (I) the generation of submerged jet and subsequent tidal-shaped structure, (II) the formation of impact pressure and subsequent lateral jetting flow, and (III) the emergence of submerged hydraulic jump. More precisely, the fluid flow in stage (I) is characterized by the establishment of the submerged jet where mean velocity of the jet declines linearly with time. This stage is also followed by the development of closed loop cavity and surge wave, resulting in vorticity concentrations adjacent

to the mixing layer. Note that, the process of tearing the liquid cushion is known as *cavitation* which rapidly occurs in conjunction with large deformation of the free-surface area at this stage. Stage (II) (shock pressure zone or impingement region) manifests itself through the deviation of the pressure distribution from the hydrostatic law where the impingement of the top face of the incident jet produces intense local pressure and stagnation zone in vicinity of the wetted bed. Note that, the region adjacent to the shock zone is the stagnation point where the jet is slowed by the bottom wall [110]. By this mechanism, the main jet undergoes substantial deflection and consequently the pressure shock occurs in vicinity of the pool floor. The processes of secondary vorticity generation and free-surface distortion are likely take place in this circumstance where the magnitude of the velocity lessens rapidly and pressure value rise dramatically, producing quite large impact pressure and velocity gradients adjacent to the pool bed. In fact, an abrupt change in the direction of the falling jet and subsequent formation of impact pressure are two main factors in failure of floor slabs as highlighted by Gou et al. [111]. In stage (III), the flow characteristics closely resemble that of the "*submerged wall jet*", where the fluid flow propagates horizontally and diffuses along the pool floor, inducing vortex motion either side of the impingement point. The initiation of stage (III) is accompanied by the monotonic reduction in the magnitude of pressure shock. Based on the above discussion, one can observe from Figs. 23 and 24 that in both cases, once the vent is opened, due to the effect of gravity force the incident jet is developed and ejected from the orifice. During the time period of $0 \le T \le 0.5s$, the jet travels obliquely and eventually strikes on the upper surface of the pool and starts penetrating through it, giving rise to the formation of a hole around the jet which in turn helps the entrainment of the captured air. As time elapses ($0.5s < T \le 0.78s$), owing to the drilling action of the descending jet, a pair of surge waves are created and propagate horizontally toward upstream and downstream parts of the

reservoir, forming the large tidal-shaped structures and some satellite air rollers within the pool. It is evident that, the hole developed by the jet gets larger and the pressure characteristics vary significantly, indicating the commencement of the second stage (II) where the shock pressure occurs. It should be underlined that, the onset of surface breaking is followed by the jet deceleration in vicinity of the bottom wall which manifests itself through the formation of a long mixing layer. As expected at this stage, the pressure distribution becomes increasingly non-hydrostatic and more air is entrained, corroborating the development of localized strong cores of positive and negative vorticity around the falling jet. It is therefore not surprising that, the resultant pressure time histories (as depicted in Figs. 23 and 24) get more irregular and exhibit oscillatory behavior with several peaks. At late times ($0.78s < T \leq 1.46s$), the reflected wave moves backward with low-to-moderate fluid inertia and air pockets become more scattered and elongated around the stagnation point due to the extensive strain field. By this mechanism, more complex circulation structures are induced and subsequently the interface layer between free-falling jet and liquid pool becomes more twisted. This physical behavior can be attributed to the heterogeneity of the mean velocity profile of the jet and energy dissipation of falling jet which causes the macro-recirculating zones to continuously break down into small scale eddies until viscosity ultimately dissipates them [76]. This mechanism causes the jet to slow down, leading to the significant attenuation of the pressure shock and high level of fluid mixing. However, due to difference in the magnitude of the buoyancy force induced by density contrast between the falling jet and plunge pool, different scenarios occur in cases 9 and 10. It can be seen that, due to low buoyancy force induced by density gradient in case 9 ($\rho_M / \rho_H = 0.6$), the oil jet penetrates moderately into the water pool and starts floating on the pool surface. In view of this, the resultant immersed jet never meets the bottom wall, leading to the moderate pressure shock as compared to case 10. On the other hand, it is evident that in case

10 the falling water jet pierces the oil pool and moves obliquely until it encounters the pool bed where the stagnation point occurs. This observation is compatible with the time history of the pressure variations recorded at the plunge pool floor in Fig. 25. As anticipated, the intensity of the pressure shock (i.e. peak pressure) in case 9 is significantly lower than that of case 10 which indicates that the initial liquid depth in case 10 is sufficiently high to protect the plunge pool floor from the destructive/erosive power of oil flow. It is worthwhile mentioning that, the time variations of the oil/water level heights in cargo tank in cases 9 and 10 are also provided as complementary data which can be utilized by scholars for the validation and verification of the computational CFD-VOF software platform.

The overall examination of the calculated results in Figs. 23 to 25 illustrates that, the proposed numerical model is able to handle extremely violent multi-fluid flows involving spilling, surging, and plunging breaking processes. That is to say, interface position is captured precisely and corresponding pressure distribution is smooth without unphysical oscillation, affirming the effectiveness of the proposed third-order NVD scheme and semi-iterative MPISO algorithm in mitigating false-diffusion errors and spurious density oscillations.

7. Conclusion

In the current work, two crucial drawbacks related to the classical Volume-Of-Fluid (VOF) method namely: (1) interface smearing arising from the false-diffusion errors and (2) spurious velocity fluctuation in vicinity of the physical discontinuities were systematically resolved. The validity of the developed computational model was tested against five challenging benchmark cases including dam-break flow over the dry bed, oil spill from the damaged container, single bubble rising, merging of two rising bubbles and two-phase Rayleigh-Taylor Instability problems. Having

verified the accuracy and versatility of the CFD code, it was then applied to analyze 3 new benchmark solutions. The important findings from the present study can be summarized as follows:

- The predicted results revealed that, the Modified PISO algorithm (MPISO) can efficiently alleviate unphysical velocity oscillation and consequently produce smoother and continuous velocity/pressure distributions in vicinity of the physical discontinuities.
- The results showed that, the newly constructed NVD-TVD convection scheme can successfully control and restrict the thickness of the interfaces to a maximum of 2-3 computational grids.
- The results showed that, the improved VOF method can successfully mitigate the false-diffusion errors on the uniform grids without the necessity to apply local mesh-refinement technique.
- The comparison of the predicted results with the conventional Lagrangian particle method vividly showed that, the mesh-free SPH model cannot accurately retain the sharpness of the interface and is also characterized by the problem so-called "*particle clustering*".
- It was found that, the traditional Lagrangian SPH model cannot effectively capture small recirculation regions.
- The predicted results showed that, the newly developed third-order NVD-TVD convection scheme can effectively eliminate the undesirable interface smearing due to numerical dissipation and mitigate unfavorable effects of false-diffusion errors.
- The numerical simulations of series of challenging real-life problems including oil/water leakage from the damaged container, merging of two rising bubbles and three-phase

Rayleigh-Taylor Instability problems clearly proved the versatility and robustness of the improved VOF model in handling multi-fluid flows with low and high density contrasts.

- The accurate prediction of the dam failure problem clearly illustrated the performance and effectiveness of the proposed modifications in addressing the problem of numerical smearing when flow-to-grid skewness is substantial.
- The results showed that in case of two rising bubbles, the shape evolution of the trailing bubble is dramatically affected by the movement and wake region of the leading bubble.

This developed coded based on the VOF model provides basis for future research on the phase change problems (i.e. solidification) and turbulent multi-fluid flows with more complex interface deformation.

CRediT authorship contribution statement

Tarek Merabtene: Conceptualization, Methodology, Validation, Writing-review & editing.

Faroogh Garoosi: Conceptualization, Methodology, FORTRAN Code development, Validation, Visualization, Writing-original draft.

Tew-Fik Mahdi: Supervision, Conceptualization, Methodology, Funding acquisition, Validation, Writing- review & editing.

Supplementary material

In order to provide a comprehensive understanding of physical behavior behind the nine canonical test cases, some video files are provided as supplementary material.

Acknowledgment

This research was funded, in part, by a National Science and Engineering Research Council (NSERC) Discovery Grant for the co-author Tew-Fik Mahdi, application No: RGPIN-2021-03272.

Appendix A (Modified PISO algorithm for solving pressure-velocity linked equation)

Along this appendix, a modified version of the non-iterative PISO algorithm [49] (MPISO) is introduced through incorporating the third pressure correction equation into the methodology, aiming to establish a robust and efficient pressure-based solver for the treatment of the pressure-velocity coupling and to eliminate non-physical velocity fluctuations from the computational domain in highly multiphase convection-dominated flows. As outlined in section 4, the newly developed third-order NVD-TVD bounded scheme together with the second-order central differencing scheme are utilized for the discretization of the convection and diffusion terms in the momentum equations. The transient terms ($\partial\rho\mathbf{u}/\partial t$) in the momentum equations is treated using the backward first-order Euler while the central differencing scheme from neighbouring nodes located on the *u*- and *v*-control volume boundaries are employed to approximate the pressure gradient terms (∇p) [58]. The implementation of the above differencing schemes results in a system of linear algebraic equations as

$$a_{ip}\mathbf{u}_p = \sum a_{np}\mathbf{u}_{np} + S_u + S_t - A_p(p_p - p_{np}) \tag{A1}$$

where subscripts *p* and *np* stand for the values at the central and neighboring nodes of the computational cell while the term $\sum a_{np}\mathbf{u}_{np}$ represents the operator which reflects the contribution of the neighboring velocities surrounding node "*p*". The coefficient a_{np} contains combinations of the convective flux per unit mass and the diffusive conductance at *u*- and *v*-control volume cell

faces where its summation over the neighbor points can produce the diagonal coefficient $a_p = \sum a_{np}$ [49]. However, by substituting the implicit backward Euler scheme in Eq. (A1):

$$\frac{\partial \rho \mathbf{u}}{\partial t} = \frac{(\rho \mathbf{u})_p^{n+1} - (\rho \mathbf{u})_p^n}{\Delta t} \tag{A2}$$

the diagonal coefficient a_{ip} can be modified as follows:

$$a_{ip} = a_p + \frac{\rho_p^{n+1}}{\Delta t} \Delta x \Delta y \tag{A3}$$

where a_p is the central coefficient arising from the discretization of the governing equations in the steady state condition [112]. Now, the source term S_t in Eq. (A1) can be written as:

$$S_t = \frac{(\rho \mathbf{u})_p^n}{\Delta t} \Delta x \Delta y \tag{A4}$$

The source term S_u in Eq. (A1) includes "*deferred correction*" and all the remaining body forces such as gravity and surface tension. To initiate the MPISO algorithm, the initial guesses for the velocity components ($\mathbf{u}^*$) are used. Generally, the discretized momentum equation (Eq. (A1)) based on the correct pressure value (p^{n+1}) and guess velocity field can produce the correct velocity distribution as follows:

$$a_{ip} \mathbf{u}_p^{n+1} = (\sum a_{np} \mathbf{u}_{np}^*) + S_u + S_t - A_p (p_p^{n+1} - p_{np}^{n+1}) \tag{A5}$$

However, since the pressure information in most engineering and industrial problems is completely unknown, one can introduce a guessed pressure (p^*) and substitute it into the Eq. (A1) as:

$$a_{ip} \mathbf{u}_p^{**} = (\sum a_{np} \mathbf{u}_{np}^*) + S_u + S_t - A_p (p_p^* - p_{np}^*) \tag{A6}$$

Before proceeding further, it should be noted that, all constant coefficients in Eq. (A6) including a_{np} and a_{ip} are estimated using the guesses velocity at the current time level [113]. In the above

equation, $\mathbf{u}^{**}$ is termed as predicted velocity which cannot satisfy the local continuity conservation in the boundary control volume. By subtracting Eq. (A6) from (A5) and introducing the incremental pressure and velocity variables (p' and $\mathbf{u}'$), the following formulations can be obtained:

$$a_{ip}(\mathbf{u}_p^{n+1} - \mathbf{u}_p^{**}) = \sum a_{np}(\mathbf{u}_{np}^{*} - \mathbf{u}_{np}^{*}) - A_p[(p_p^{n+1} - p_p^{*}) - (p_{np}^{n+1} - p_{np}^{*})] \tag{A7}$$

$$p^{n+1} = p^{*} + \alpha_{p1} p' \tag{A8}$$

$$\mathbf{u}^{n+1} = \mathbf{u}^{**} + \mathbf{u}'$$

$$(\mathbf{u}'_p) = -\frac{A_p}{a_{ip}}[p'_p - p'_{np}] \tag{A9}$$

where α_{p1} is the first under-relaxation factor which sets as unity in the present work. Substitution of the corrected velocities of equations (A8)–(A9) into the following discretised continuity equation:

$$[(\rho u A)_e - (\rho u A)_w] + [(\rho v A)_n - (\rho v A)_s] = 0 \tag{A10}$$

leads to the first pressure-correction equation as:

$$\begin{aligned} &a_{i,j}P'_{i,j} = a_{i+1,j}P'_{i+1,j} + a_{i-1,j}P'_{i-1,j} + a_{i,j+1}P'_{i,j+1} + a_{i,j-1}P'_{i,j-1} + b_{i,j} - \left(\frac{\rho_p^{n+1} - \rho_p^{n}}{\Delta t \rho_p^{n+1}}\Delta x \Delta y\right) \\ &a_{i,j} = a_{i+1,j} + a_{i-1,j} + a_{i,j+1} + a_{i,j-1} \\ &a_{i+1,j} = d_{i+1,j}\Delta y, \quad a_{i-1,j} = d_{i,j}\Delta y \\ &a_{i,j+1} = d_{i,j+1}\Delta x, \quad a_{i,j-1} = d_{i,j}\Delta x \\ &b_{i,j} = u_{i,j}^{**}\Delta y - u_{i+1,j}^{**}\Delta y + v_{i,j}^{**}\Delta x - v_{i,j+1}^{**}\Delta x \end{aligned} \tag{A11}$$

Once the pressure correction equation is solved, the velocity and pressure fields can be modified through Eq. (A8). Before proceeding further, it is important to stress that, contrary to the non-iterative version of the standard PISO algorithm, in order to reach satisfactory level of accuracy, the prescribed number of iteration is required. On the other hand, unlike the standard fully-iterative PISO solver, in order to save the computational cost, the first iterative loop is applied to system of

Eq. (A11) rather than extending it throughout the algorithm. However, in order to further enhance the consistency and stability of the solution, we assume that the corrected pressure and velocity fields obtained from Eqs. (A8) and (A11) still cannot satisfy the continuity constraint and therefore further modifications are needed. To this end, the superscript on the corrected pressure and velocity variables is changed from ($p^{n+1}, \mathbf{u}^{n+1}$) to ($p^{**}, \mathbf{u}^{***}$). By substituting the semi-corrected values of p^{**} and $\mathbf{u}^{***}$ into the Eq. (A1), the second predicted velocities ($\mathbf{u}^{***}$) can be obtained as:

$$a_{ip}\mathbf{u}_p^{***} = \sum a_{np}\mathbf{u}_{np}^{***} + S_u + S_t - A_p(p_p^{**} - p_{np}^{**}) \tag{A12}$$

On the other hand, the discretised momentum equations with second intermediate velocities ($\mathbf{u}^{***}$) and true pressure field (p^{n+1}) can lead to:

$$a_{ip}\mathbf{u}_p^{n+1} = \sum a_{np}\mathbf{u}_{np}^{***} + S_u + S_t - A_p(p_p^{n+1} - p_{np}^{n+1}) \tag{A13}$$

In the above equation, the $\mathbf{u}^{n+1}$ is a twice-corrected velocity field which can rigorously ensure the continuity condition ($\nabla \cdot \mathbf{u}^{n+1} = 0$). At this stage, it is worthwhile mentioning that, unlike the classical standard PISO algorithm, due to the implementation of the semi-corrected velocity and pressure values ($p^{**}, \mathbf{u}^{***}$) in Eqs. (A12) and (A13), the central (a_{ip}) and neighbor (a_{np}) coefficients in these equations are replaced by updated coefficients a_{ip} and a_{np}, respectively. Our results have revealed that, although this modification is minor, it has a remarkable influence on the convergence rate of numerical simulation when it comes to cope with incompressible multiphase flows.

By subtracting Eq. (A13) from (A12) and defining the second incremental pressure variable (p'') as the difference between correct pressure field (p^{n+1}) and the semi-corrected one (p^{**}), the following relationships can be derived:

$$\mathbf{u}^{n+1} - \mathbf{u}_p^{***} = \frac{\sum a_{np}\mathbf{u}_{np}^{***} + S_u + S_t}{a_{ip}} - \frac{\sum a_{np}\mathbf{u}_{np}^{***} + S_u + S_t}{a_{ip}} - \frac{A_p(p_p^{n+1} - p_{np}^{n+1})}{a_{ip}} + \frac{A_p(p_p^{**} - p_{np}^{**})}{a_{ip}} \quad \text{(A14)}$$

$$p^{n+1} = p^{**} + \alpha_{p2} p'' \quad \text{(A15)}$$

$$\mathbf{u}^{n+1} = \mathbf{u}_p^{***} + \frac{\sum a_{np}(\mathbf{u}_{np}^{***} - \mathbf{u}_{np}^{***})}{a_{ip}} - \frac{A_p(p_p'' - p_{np}'')}{a_{ip}} \quad \text{(A16)}$$

In the above equation, the coefficient α_{p2} is the second under-relaxation factor which is taken as unity. Substitution of $\mathbf{u}^{n+1}$ in the discretized continuity equation yields the second Pressure-Poisson Equation for the incremental pressure as:

$$a_{i,j}P''_{i,j} = a_{i+1,j}P''_{i+1,j} + a_{i-1,j}P''_{i-1,j} + a_{i,j+1}P''_{i,j+1} + a_{i,j-1}P''_{i,j-1} + \hat{b}_{i,j} + \hat{\hat{b}}_{i,j} - \frac{\rho_p^{n+1} - \rho_p^n}{\Delta t \rho_p^{n+1}}\Delta x \Delta y \quad \text{(A17)}$$

$$\begin{aligned}
&a_{i,j} = a_{i+1,j} + a_{i-1,j} + a_{i,j+1} + a_{i,j-1} \\
&a_{i+1,j} = d_{i+1,j}\Delta y, \quad a_{i-1,j} = d_{i,j}\Delta y \\
&a_{i,j+1} = d_{i,j+1}\Delta x, \quad a_{i,j-1} = d_{i,j}\Delta x \\
&\hat{b}_{i,j} = u_{i,j}^{***}\Delta y - u_{i+1,j}^{***}\Delta y + \hat{v}_{i,j}^{***}\Delta x - \hat{v}_{i,j+1}^{***}\Delta x \\
&\hat{\hat{b}}_{i,j} = \left(\frac{\sum a_{np}(u_{np}^{***} - u_{np}^{***})}{a_{ip}}\right)_{i,j}\Delta y - \frac{\sum a_{np}(u_{np}^{***} - u_{np}^{***})}{a_{ip}}\Bigg)_{i+1,j}\Delta y \\
&+ \frac{\sum \widehat{a_{np}}(\hat{v}_{np}^{***} - v_{np}^{***})}{\widehat{a_{ip}}}\Bigg)_{i,j}\Delta x - \frac{\sum \widehat{a_{np}}(\hat{v}_{np}^{***} - v_{np}^{***})}{\widehat{a_{ip}}}\Bigg)_{i,j+1}\Delta x
\end{aligned} \quad \text{(A18)}$$

Having determined the second incremental pressure distribution (p''), the true pressure field and velocity components can be calculated via Eqs. (A15) and (A16). Note that, similar to the first pressure correction equation (i.e. Eq. (A11)), the second iterative loop with limited number of iteration is also imposed to the system of Eq. (A18). At this stage, it is relevant to mention that, in

the standard PISO-algorithm proposed by Issa [49], the author ideally assumed that the second intermediate velocities ($\mathbf{u}^{***}$) appeared as a source term ($\hat{b}_{i,j}$) on the right hand side of Eq. (A18) is sufficiently accurate to satisfy continuity ($\nabla \cdot \mathbf{u}^{***} = 0,\ \hat{b}_{i,j} = 0$). However, our results reveal that this assumption is not necessarily valid in the nonlinear multi-fluid flows so that the strict enforcement of mass continuity via the direct imposition of $\nabla \cdot \mathbf{u}^{***} = 0$ (or $\hat{b}_{i,j} = 0$) in Eq. (A18) may lead to the pressure/velocity fluctuations across the moving interfaces. Toward the last stage of the methodology, once again, we assume that the modified pressure and velocity field obtained from Eqs. (15) and (16) still cannot guarantee mass conservation and thus further improvements are needed to reach the desired level of accuracy. For this purpose, once again, the superscript of the corrected pressure and velocity variables is changed from ($p^{n+1}, \mathbf{u}^{n+1}$) to ($p^{***}, \mathbf{u}^{****}$). By substituting the twice-corrected values of p^{***} and $\mathbf{u}^{****}$ into the Eq. (A1), the third predicted velocities ($\mathbf{u}^{*****}$) can be obtained as:

$$a_{ip}\mathbf{u}_p^{*****} = \sum a_{np}\mathbf{u}_{np}^{*****} + S_u + S_t - A_p(p_p^{***} - p_{np}^{***}) \tag{A19}$$

On the other hand, the discretised momentum equations with second intermediate velocities ($\mathbf{u}^{***}$) and true pressure field (p^{n+1}) can lead to:

$$a_{ip}\mathbf{u}_p^{n+1} = \sum a_{np}\mathbf{u}_{np}^{*****} + S_u + S_t - A_p(p_p^{n+1} - p_{np}^{n+1}) \tag{A20}$$

In the above equation, the $\mathbf{u}^{n+1}$ is a thrice-corrected velocity field which can efficiently satisfy the continuity condition ($\nabla \cdot \mathbf{u}^{n+1} = 0$). As expected, since the updated velocity and pressure values are used in Eqs. (A19) and (A20), the central (a_{ip}) and neighbor (a_{np}) coefficients in these equations are replaced by the new coefficients of a_{ip} and a_{np}, respectively. By subtracting Eq. (A20) from

(A19) and defining the third incremental pressure variable (p''') as the difference between correct pressure field (p^{n+1}) and the twice-corrected one (p^{***}), the following relationships can be derived:

$$\mathbf{u}^{n+1} - \mathbf{u}_p^{****} = \frac{\sum a_{np}\mathbf{u}_{np}^{****} + S_u + S_t}{a_{ip}} - \frac{\sum a_{np}\mathbf{u}_{np}^{****} + S_u + S_t}{a_{ip}} - \frac{A_p(p_p^{n+1} - p_{np}^{n+1})}{a_{ip}} + \frac{A_p(p_p^{***} - p_{np}^{***})}{a_{ip}} \quad \text{(A21)}$$

$$p^{n+1} = p^{***} + \alpha_{p3} p''' \quad \text{(A22)}$$

$$\mathbf{u}^{n+1} = \mathbf{u}_p^{****} + \frac{\sum a_{np}(\mathbf{u}_{np}^{****} - \mathbf{u}_{np}^{****})}{a_{ip}} - \frac{A_p(p_p''' - p_{np}''')}{a_{ip}} \quad \text{(A23)}$$

In the above equation, the coefficient $\alpha_{p3} = 1.0$ is the third under-relaxation factor. Substitution of $\mathbf{u}^{n+1}$ in the discretized continuity equation yields the third Pressure-Poisson Equation for the incremental pressure as:

$$a_{i,j}P_{i,j}''' = a_{i+1,j}P_{i+1,j}''' + a_{i-1,j}P_{i-1,j}''' + a_{i,j+1}P_{i,j+1}''' + a_{i,j-1}P_{i,j-1}''' + \hat{b}_{i,j} + \hat{\hat{b}}_{i,j} - \frac{\rho_p^{n+1} - \rho_p^n}{\Delta t \rho_p^{n+1}}\Delta x \Delta y \quad \text{(A24)}$$

$$a_{i,j} = a_{i+1,j} + a_{i-1,j} + a_{i,j+1} + a_{i,j-1}$$

$$a_{i+1,j} = d_{i+1,j}\Delta y, \quad a_{i-1,j} = d_{i,j}\Delta y$$

$$a_{i,j+1} = d_{i,j+1}\Delta x, \quad a_{i,j-1} = d_{i,j}\Delta x$$

$$\hat{b}_{i,j} = u_{i,j}^{****}\Delta y - u_{i+1,j}^{****}\Delta y + \hat{v}_{i,j}^{****}\Delta x - \hat{v}_{i,j+1}^{****}\Delta x \quad \text{(A25)}$$

$$\hat{\hat{b}}_{i,j} = \left(\frac{\sum a_{np}(u_{np}^{****} - u_{np}^{****})}{a_{ip}}\right)_{i,j}\Delta y - \left(\frac{\sum a_{np}(u_{np}^{****} - u_{np}^{****})}{\widehat{a_{ip}}}\right)_{i+1,j}\Delta y$$

$$+ \left(\frac{\sum \widehat{a_{np}}(\hat{v}_{np}^{****} - v_{np}^{****})}{\widehat{a_{ip}}}\right)_{i,j}\Delta x - \left(\frac{\sum \widehat{a_{np}}(\hat{v}_{np}^{****} - v_{np}^{****})}{\widehat{a_{ip}}}\right)_{i,j+1}\Delta x$$

Having computed the third incremental pressure distribution (p'''), the final velocity and pressure fields can be calculated through Eqs. (A22) and (A23). Once the correct $\mathbf{u}^{n+1}$ and p^{n+1} are determined, the volume fraction equations (i.e. Eq. (4) and (5)) will be solved and the simulation

is then transferred to the next time step where the updated physical quantities ($p^{n+1}, \mathbf{u}^{n+1}$) will be employed as an initial guess values at the beginning of the next time step. However, before closing this appendix, it is noteworthy to mention that, due to the existence of two pressure correction equations at the beginning and middle of the algorithm (i.e. Eqs. (A11) and (A17-18)), the values of $\overset{****}{\mathbf{u}}_{np}$ and $\mathbf{u}_{np}^{****}$ become very close to each other ($\overset{****}{\mathbf{u}}_{np} \approx \mathbf{u}_{np}^{****}$). This observation implies that in order to boost computing speed and save the computational effort, the source term $\hat{\hat{b}}_{i,j}$ in Eq. (A25) and summation operator $\sum a_{np}(\overset{****}{\mathbf{u}}_{np} - \mathbf{u}_{np}^{****})$ in Eq. (A23) can be removed from the algorithm for sake of simplification without sacrificing too much accuracy. However, in some cases characterized by heat/pressure shock, this term ($\hat{\hat{b}}_{i,j}$) may not be equal to zero and should be taken into consideration.

References

[1] K. Whang, Y. Shin, W. Baek, Y. Jo, J.H. Hwang, J. Min, D. Kim, T. Kang, Direct and precise determination of volumetric mass transfer coefficient of carbon monoxide for miniaturized gas-liquid reactors via sensitive probing of raman transitions, Chem. Eng. J. 429 (2022) 132260.

[2] G. Tryggvason, R. Scardovelli, S. Zaleski, Direct Numerical Simulations of Gas–Liquid Multiphase Flows, Cambridge university press, 2011.

[3] I. Khan, M. Wang, M.A. Basit, W. Tian, G. Su, S. Qiu, CFD modeling of liquid entrainment through vertical T-junction of fourth stage automatic depressurization system (ADS-4), Ann. Nucl. Energy. 159 (2021) 108317.

[4] G.H. Yeoh, J. Tu, Computational techniques for multiphase flows, Butterworth-Heinemann, 2019.

[5] F. Gibou, D. Hyde, R. Fedkiw, Sharp interface approaches and deep learning techniques for multiphase flows, J. Comput. Phys. 380 (2019) 442–463.

[6] M. Sussman, P. Smereka, S. Osher, A level set approach for computing solutions to incompressible two-phase flow, J. Comput. Phys. 114 (1994) 146–159.

[7] C.W. Hirt, B.D. Nichols, Volume of fluid (VOF) method for the dynamics of free boundaries, J. Comput. Phys. 39 (1981) 201–225.

[8] J. Luo, S.-Y. Wu, L. Xiao, Z.-L. Chen, Parametric influencing mechanism and control of contact time for droplets impacting on the solid surfaces, Int. J. Mech. Sci. 197 (2021) 106333.

[9] I.U. Vakarelski, F. Yang, S.T. Thoroddsen, Effects of interface mobility on the dynamics of colliding bubbles, Curr. Opin. Colloid Interface Sci. 57 (2022) 101540.

[10] C. Mulbah, C. Kang, N. Mao, W. Zhang, A.R. Shaikh, S. Teng, A review of VOF methods for simulating bubble dynamics, Prog. Nucl. Energy. 154 (2022) 104478.

[11] X. Zhang, Z. Lin, S. Mancini, Z. Pang, P. Li, F. Liu, Numerical investigation into the effect of the internal opening arrangements on motion responses of a damaged ship, Appl. Ocean Res. 117 (2021) 102943.

[12] S. Booshi, M.J. Ketabdari, Modeling of solitary wave interaction with emerged porous breakwater using PLIC-VOF method, Ocean Eng. 241 (2021) 110041.

[13] H. Eshgarf, A.A. Nadooshan, A. Raisi, A review of multi-phase and single-phase models in the numerical simulation of nanofluid flow in heat exchangers, Eng. Anal. Bound. Elem. 146 (2023) 910–927.

[14] X. Zhang, S. Draper, H. Wolgamot, W. Zhao, L. Cheng, Eliciting features of 2D greenwater overtopping of a fixed box using modified dam break models, Appl. Ocean Res. 84 (2019) 74–91.

[15] R. Kumar, L. Cheng, Y. Xiong, B. Xie, R. Abgrall, F. Xiao, THINC scaling method that bridges VOF and level set schemes, J. Comput. Phys. 436 (2021) 110323.

[16] K.G. Lyras, B. Hanson, M. Fairweather, P.J. Heggs, A coupled level set and volume of fluid method with a re-initialisation step suitable for unstructured meshes, J. Comput. Phys. 407 (2020) 109224.

[17] N. Scapin, P. Costa, L. Brandt, A volume-of-fluid method for interface-resolved simulations of phase-changing two-fluid flows, J. Comput. Phys. 407 (2020) 109251.

[18] B.S. de Lima, L. de Souza Meira, F.J. de Souza, Numerical simulation of a water droplet splash: Comparison between PLIC and HRIC schemes for the VoF transport equation, Eur. J. Mech. 84 (2020) 63–70.

[19] B.P. Leonard, Simple high-accuracy resolution program for convective modelling of discontinuities, Int. J. Numer. Methods Fluids. 8 (1988) 1291–1318.

[20] P.H. Gaskell, A. Lau, Curvature-compensated convective transport: SMART, a new boundedness-preserving transport algorithm, Int. J. Numer. Methods Fluids. 8 (1988) 617–641.

[21] S.K. Choi, H.Y. Nam, M. Cho, A comparison of higher-order bounded convection schemes,

Comput. Methods Appl. Mech. Eng. 121 (1995) 281–301.

[22] J. Zhu, On the higher-order bounded discretization schemes for finite volume computations of incompressible flows, Comput. Methods Appl. Mech. Eng. 98 (1992) 345–360.

[23] J. Zhu, W. Rodi, A low dispersion and bounded convection scheme, Comput. Methods Appl. Mech. Eng. 92 (1991) 87–96.

[24] M. Zijlema, On the construction of a third-order accurate monotone convection scheme with application to turbulent flows in general domains, Int. J. Numer. Methods Fluids. 22 (1996) 619–641.

[25] T. Wacławczyk, T. Koronowicz, Comparison of CICSAM and HRIC high-resolution schemes for interface capturing, J. Theor. Appl. Mech. 46 (2008) 325–345.

[26] M.A. Alves, P.J. Oliveira, F.T. Pinho, A convergent and universally bounded interpolation scheme for the treatment of advection, Int. J. Numer. Methods Fluids. 41 (2003) 47–75.

[27] O. Ubbink, R.I. Issa, A method for capturing sharp fluid interfaces on arbitrary meshes, J. Comput. Phys. 153 (1999) 26–50.

[28] I. Malgarinos, N. Nikolopoulos, M. Gavaises, Coupling a local adaptive grid refinement technique with an interface sharpening scheme for the simulation of two-phase flow and free-surface flows using VOF methodology, J. Comput. Phys. 300 (2015) 732–753.

[29] V.R. Gopala, B.G.M. van Wachem, Volume of fluid methods for immiscible-fluid and free-surface flows, Chem. Eng. J. 141 (2008) 204–221.

[30] A. Arote, M. Bade, J. Banerjee, An improved compressive volume of fluid scheme for capturing sharp interfaces using hybridization, Numer. Heat Transf. Part B Fundam. 79 (2020) 29–53.

[31] A. Harten, High resolution schemes for hyperbolic conservation laws, J. Comput. Phys. 135 (1997) 260–278.

[32] P.K. Sweby, High resolution schemes using flux limiters for hyperbolic conservation laws, SIAM J. Numer. Anal. 21 (1984) 995–1011.

[33] B. Van Leer, Towards the ultimate conservative difference scheme. V. A second-order sequel to Godunov's method, J. Comput. Phys. 32 (1979) 101–136.

[34] B. van Albada, G. van Leer, A comparative study of computational methods in cosmic gas dynamics, Astron. Astrophys. 108 (1982) 76–84.

[35] P.L. Roe, M.J. Baines, Algorithms for advection and shock problems, Numer. Methods Fluid Mech. (1982) 281–290.

[36] B. Van Leer, Towards the ultimate conservative difference scheme. II. Monotonicity and conservation combined in a second-order scheme, J. Comput. Phys. 14 (1974) 361–370.

[37] B. Van Leer, Towards the ultimate conservative difference scheme. IV. A new approach to

numerical convection, J. Comput. Phys. 23 (1977) 276–299.

[38] N.P. Waterson, H. Deconinck, A unified approach to the design and application of bounded higher-order convection schemes, Numer. Methods Laminar Turbul. Flow. 9 (1995) 203–214.

[39] D. Zhang, C. Jiang, D. Liang, L. Cheng, A review on TVD schemes and a refined flux-limiter for steady-state calculations, J. Comput. Phys. 302 (2015) 114–154.

[40] H. Jasak, H.G. Weller, A.D. Gosman, High resolution NVD differencing scheme for arbitrarily unstructured meshes, Int. J. Numer. Methods Fluids. 31 (1999) 431–449.

[41] J.A. Heyns, A.G. Malan, T.M. Harms, O.F. Oxtoby, Development of a compressive surface capturing formulation for modelling free-surface flow by using the volume-of-fluid approach, Int. J. Numer. Methods Fluids. 71 (2013) 788–804.

[42] C.P. Zanutto, E.E. Paladino, F. Evrard, B. van Wachem, F. Denner, Modeling of interfacial mass transfer based on a single-field formulation and an algebraic VOF method considering non-isothermal systems and large volume changes, Chem. Eng. Sci. 247 (2022) 116855.

[43] M. Akhlaghi, V. Mohammadi, N.M. Nouri, M. Taherkhani, M. Karimi, Multi-Fluid VoF model assessment to simulate the horizontal air–water intermittent flow, Chem. Eng. Res. Des. 152 (2019) 48–59.

[44] R.F.L. Cerqueira, E.E. Paladino, F. Evrard, F. Denner, B. van Wachem, Multiscale modeling and validation of the flow around Taylor bubbles surrounded with small dispersed bubbles using a coupled VOF-DBM approach, Int. J. Multiph. Flow. 141 (2021) 103673.

[45] D. Wang, S. Dong, M. Ning, A. Incecik, Extended variable-time-step Adams–Bashforth–Moulton method for strongly coupled fluid–structure interaction simulation, Ocean Eng. 219 (2021) 108335.

[46] S. Radman, C. Fiorina, A. Pautz, Development of a novel two-phase flow solver for nuclear reactor analysis: algorithms, verification and implementation in OpenFOAM, Nucl. Eng. Des. 379 (2021) 111178.

[47] T.Q.D. Pham, S. Choi, Numerical analysis of direct contact condensation-induced water hammering effect using OpenFOAM in realistic steam pipes, Int. J. Heat Mass Transf. 171 (2021) 121099.

[48] G. Tretola, K. Vogiatzaki, S. Navarro-Martinez, Implementation of a probabilistic surface density volume of fluid approach for spray atomisation, Comput. Fluids. (2021) 105121.

[49] R.I. Issa, Solution of the implicitly discretised fluid flow equations by operator-splitting, J. Comput. Phys. 62 (1986) 40–65.

[50] H. Wang, H. Wang, F. Gao, P. Zhou, Z.J. Zhai, Literature review on pressure–velocity decoupling algorithms applied to built-environment CFD simulation, Build. Environ. 143 (2018) 671–678.

[51] D.L. Youngs, Time-dependent multi-material flow with large fluid distortion, Numer. Methods Fluid Dyn. 24 (1982) 273–85.

[52] J.E. Pilliod Jr, E.G. Puckett, Second-order accurate volume-of-fluid algorithms for tracking material interfaces, J. Comput. Phys. 199 (2004) 465–502.

[53] F. Garoosi, T. Mahdi, Presenting a novel higher-order bounded convection scheme for simulation of multiphase flows and convection heat transfer, Int. J. Heat Mass Transf. 172 (2021) 121163.

[54] E.G. Puckett, A.S. Almgren, J.B. Bell, D.L. Marcus, W.J. Rider, A high-order projection method for tracking fluid interfaces in variable density incompressible flows, J. Comput. Phys. 130 (1997) 269–282.

[55] G.Y. Soh, G.H. Yeoh, V. Timchenko, An algorithm to calculate interfacial area for multiphase mass transfer through the volume-of-fluid method, Int. J. Heat Mass Transf. 100 (2016) 573–581.

[56] J.U. Brackbill, D.B. Kothe, C. Zemach, A continuum method for modeling surface tension, J. Comput. Phys. 100 (1992) 335–354.

[57] X. Yin, I. Zarikos, N.K. Karadimitriou, A. Raoof, S.M. Hassanizadeh, Direct simulations of two-phase flow experiments of different geometry complexities using Volume-of-Fluid (VOF) method, Chem. Eng. Sci. 195 (2019) 820–827.

[58] H.K. Versteeg, W. Malalasekera, An Introduction To Computational Fluid Dynamics: The Finite Volume Method, Pearson Education, 2007.

[59] M. Sheikholeslami, Numerical investigation of solar system equipped with innovative turbulator and hybrid nanofluid, Sol. Energy Mater. Sol. Cells. 243 (2022) 111786.

[60] F. Garoosi, K. Hooman, Numerical simulation of multiphase flows using an enhanced Volume-of-Fluid (VOF) method, Int. J. Mech. Sci. 215 (2022) 106956.

[61] W. Gao, H. Li, Y. Liu, A high resolution NV/TVD Hermite polynomial upwind scheme for convection-dominated problems, Math. Methods Appl. Sci. 36 (2013) 1107–1122.

[62] T. Chourushi, A High Resolution Equi-Gradient scheme for convective flows, Appl. Math. Comput. 338 (2018) 123–140.

[63] S. Bidadi, S.L. Rani, Quantification of numerical diffusivity due to TVD schemes in the advection equation, J. Comput. Phys. 261 (2014) 65–82.

[64] M.S. Darwish, A new high-resolution scheme based on the normalized variable formulation, Numer. Heat Transf. Part B Fundam. 24 (1993) 353–371.

[65] N.P. Waterson, H. Deconinck, Design principles for bounded higher-order convection schemes–a unified approach, J. Comput. Phys. 224 (2007) 182–207.

[66] W. Gao, H. Li, Y. Liu, Y.-J. Jian, An oscillation-free high order TVD/CBC-based upwind scheme for convection discretization, Numer. Algorithms. 59 (2012) 29–50.

[67] M.S. Darwish, F.H. Moukalled, Normalized variable and space formulation methodology for high-resolution schemes, Numer. Heat Transf. 26 (1994) 79–96.

[68] L. Lobovský, E. Botia-Vera, F. Castellana, J. Mas-Soler, A. Souto-Iglesias, Experimental investigation of dynamic pressure loads during dam break, J. Fluids Struct. 48 (2014) 407–434.

[69] C. Zhang, X.Y. Hu, N.A. Adams, A weakly compressible SPH method based on a low-dissipation Riemann solver, J. Comput. Phys. 335 (2017) 605–620.

[70] I.-R. Park, K.-S. Kim, J. Kim, S.-H. Van, Numerical investigation of the effects of turbulence intensity on dam-break flows, Ocean Eng. 42 (2012) 176–187.

[71] A. Issakhov, A. Borsikbayeva, The impact of a multilevel protection column on the propagation of a water wave and pressure distribution during a dam break: Numerical simulation, J. Hydrol. 598 (2021) 126212.

[72] G. Lauber, W.H. Hager, Experiments to dambreak wave: Horizontal channel, J. Hydraul. Res. 36 (1998) 291–307.

[73] C. Zhuo, C. Zhong, X. Guo, J. Cao, Numerical investigation of four-lid-driven cavity flow bifurcation using the multiple-relaxation-time lattice Boltzmann method, Comput. Fluids. 110 (2015) 136–151.

[74] W. Yang, Q. Zhu, W. Lai, F. Li, Study on anti-tsunami optimization design of bridge pier: A new type bridge pier, Ocean Eng. 213 (2020) 107701.

[75] P. Xie, V.H. Chu, The impact of tsunami wave force on elevated coastal structures, Coast. Eng. 162 (2020) 103777.

[76] P. Liu, J. Gao, Y. Li, Experimental investigation of submerged impinging jets in a plunge pool downstream of large dams, Sci. China Ser. E Technol. Sci. 41 (1998) 357–365.

[77] E. Daly, S. Grimaldi, H.H. Bui, Explicit incompressible SPH algorithm for free-surface flow modelling: A comparison with weakly compressible schemes, Adv. Water Resour. 97 (2016) 156–167.

[78] A.H. Kashani, A.M. Halabian, K. Asghari, A numerical study of tuned liquid damper based on incompressible SPH method combined with TMD analogy, J. Fluids Struct. 82 (2018) 394–411.

[79] J. Lu, Z. Yang, H. Wu, W. Wu, F. Liu, S. Xu, H. Yang, S. Yan, Model experiment on the dynamic process of oil leakage from the double hull tanker, J. Loss Prev. Process Ind. 43 (2016) 174–180.

[80] S.-M. Jeong, J.-W. Nam, S.-C. Hwang, J.-C. Park, M.-H. Kim, Numerical prediction of oil amount leaked from a damaged tank using two-dimensional moving particle simulation method, Ocean Eng. 69 (2013) 70–78.

[81] G. Duan, S. Koshizuka, A. Yamaji, B. Chen, X. Li, T. Tamai, An accurate and stable

multiphase moving particle semi-implicit method based on a corrective matrix for all particle interaction models, Int. J. Numer. Methods Eng. 115 (2018) 1287–1314.

[82] G. Duan, B. Chen, X. Zhang, Y. Wang, A multiphase MPS solver for modeling multi-fluid interaction with free surface and its application in oil spill, Comput. Methods Appl. Mech. Eng. 320 (2017) 133–161.

[83] D. Zuzio, J.L. Estivalezes, An efficient block parallel AMR method for two phase interfacial flow simulations, Comput. Fluids. 44 (2011) 339–357.

[84] Z. Cao, D. Sun, J. Wei, B. Yu, A coupled volume-of-fluid and level set method based on multi-dimensional advection for unstructured triangular meshes, Chem. Eng. Sci. 176 (2018) 560–579.

[85] M. Haghshenas, J.A. Wilson, R. Kumar, Algebraic coupled level set-volume of fluid method for surface tension dominant two-phase flows, Int. J. Multiph. Flow. 90 (2017) 13–28.

[86] K. Ling, S. Zhang, P.-Z. Wu, S.-Y. Yang, W.-Q. Tao, A coupled volume-of-fluid and level-set method (VOSET) for capturing interface of two-phase flows in arbitrary polygon grid, Int. J. Heat Mass Transf. 143 (2019) 118565.

[87] X. He, S. Chen, R. Zhang, A lattice Boltzmann scheme for incompressible multiphase flow and its application in simulation of Rayleigh–Taylor instability, J. Comput. Phys. 152 (1999) 642–663.

[88] Y. Zhao, H.H. Tan, B. Zhang, A high-resolution characteristics-based implicit dual time-stepping VOF method for free surface flow simulation on unstructured grids, J. Comput. Phys. 183 (2002) 233–273.

[89] C.H. Yu, Z.T. Ye, T.W.H. Sheu, Y.T. Lin, X.Z. Zhao, An improved interface preserving level set method for simulating three dimensional rising bubble, Int. J. Heat Mass Transf. 103 (2016) 753–772.

[90] A. Smolianski, Finite-element/level-set/operator-splitting (FELSOS) approach for computing two-fluid unsteady flows with free moving interfaces, Int. J. Numer. Methods Fluids. 48 (2005) 231–269.

[91] M. Vahabi, H. Hadavandmirzaei, B. Kamkari, H. Safari, Interaction of a pair of in-line bubbles ascending in an Oldroyd-B liquid: A numerical study, Eur. J. Mech. 85 (2021) 413–429.

[92] X. Wen, W. Zhao, D. Wan, A multiphase MPS method for bubbly flows with complex interfaces, Ocean Eng. 238 (2021) 109743.

[93] R. Lord, Investigation of the character of the equilibrium of an incompressible heavy fluid of variable density, Sci. Pap. (1900) 200–207.

[94] G.I. Taylor, The instability of liquid surfaces when accelerated in a direction perpendicular to their planes. I, Proc. R. Soc. London. Ser. A. Math. Phys. Sci. 201 (1950) 192–196.

[95] Q. Zhang, The motion of a single bubble or spike in Rayleigh-Taylor unstable interfaces, IMPACT Comput. Sci. Eng. 3 (1991) 277–304.

[96] T. Luo, J. Wang, C. Xie, M. Wan, S. Chen, Effects of compressibility and Atwood number on the single-mode Rayleigh-Taylor instability, Phys. Fluids. 32 (2020) 12110.

[97] J.-L. Guermond, L. Quartapelle, A projection FEM for variable density incompressible flows, J. Comput. Phys. 165 (2000) 167–188.

[98] A. Celani, A. Mazzino, P. Muratore-Ginanneschi, L. Vozella, Phase-field model for the Rayleigh–Taylor instability of immiscible fluids, J. Fluid Mech. 622 (2009) 115–134.

[99] J. Glimm, X. Li, A.-D. Lin, Nonuniform approach to terminal velocity for single mode Rayleigh-Taylor instability, Acta Math. Appl. Sin. 18 (2002) 1–8.

[100] G. Tryggvason, Numerical simulations of the Rayleigh-Taylor instability, J. Comput. Phys. 75 (1988) 253–282.

[101] D. Pan, C. Chang, The capturing of free surfaces in incompressible multi-fluid flows, Int. J. Numer. Methods Fluids. 33 (2000) 203–222.

[102] F. Garoosi, T.-F. Mahdi, Numerical simulation of three-fluid Rayleigh-Taylor instability using an enhanced Volume-Of-Fluid (VOF) model: New benchmark solutions, Comput. Fluids. 245 (2022) 105591.

[103] M. Cheng, J. Hua, J. Lou, Simulation of bubble–bubble interaction using a lattice Boltzmann method, Comput. Fluids. 39 (2010) 260–270.

[104] A. Kumar, B. Ray, G. Biswas, Dynamics of two coaxially rising gas bubbles, Phys. Fluids. 33 (2021) 52106.

[105] S. Nagrath, K.E. Jansen, R.T. Lahey Jr, Computation of incompressible bubble dynamics with a stabilized finite element level set method, Comput. Methods Appl. Mech. Eng. 194 (2005) 4565–4587.

[106] K.N. Aroh, I.U. Ubong, C.L. Eze, I.M. Harry, J.C. Umo-Otong, A.E. Gobo, Oil spill incidents and pipeline vandalization in Nigeria: impact on public health and negation to attainment of Millennium Development Goal: the Ishiagu example, Disaster Prev. Manag. An Int. J. (2010).

[107] D. De Padova, M. Mossa, S. Sibilla, A multi-phase SPH simulation of oil spill diffusion in seawater currents, Acta Mech. Sin. 39 (2023) 722230.

[108] H. Zhu, P. Lin, Q. Pan, A CFD (computational fluid dynamic) simulation for oil leakage from damaged submarine pipeline, Energy. 64 (2014) 887–899.

[109] S. Zhang, J. Lian, Y. Yao, J. He, F. Liu, B. Ma, Characteristics of waves generated by submerged jets from rectangular orifices, Exp. Therm. Fluid Sci. 140 (2023) 110757.

[110] R. Duarte, A.J. Schleiss, A. Pinheiro, Influence of jet aeration on pressures around a block embedded in a plunge pool bottom, Environ. Fluid Mech. 15 (2015) 673–693.

[111] W. Gou, H. Li, Y. Du, H. Yin, F. Liu, J. Lian, Effect of sediment concentration on hydraulic characteristics of energy dissipation in a falling turbulent jet, Appl. Sci. 8 (2018) 1672.

[112] Ž. Tuković, M. Perić, H. Jasak, Consistent second-order time-accurate non-iterative PISO-algorithm, Comput. Fluids. 166 (2018) 78–85.

[113] S. MacNamara, G. Strang, Operator splitting, in: Split. Methods Commun. Imaging, Sci. Eng., Springer, 2016: pp. 95–114.

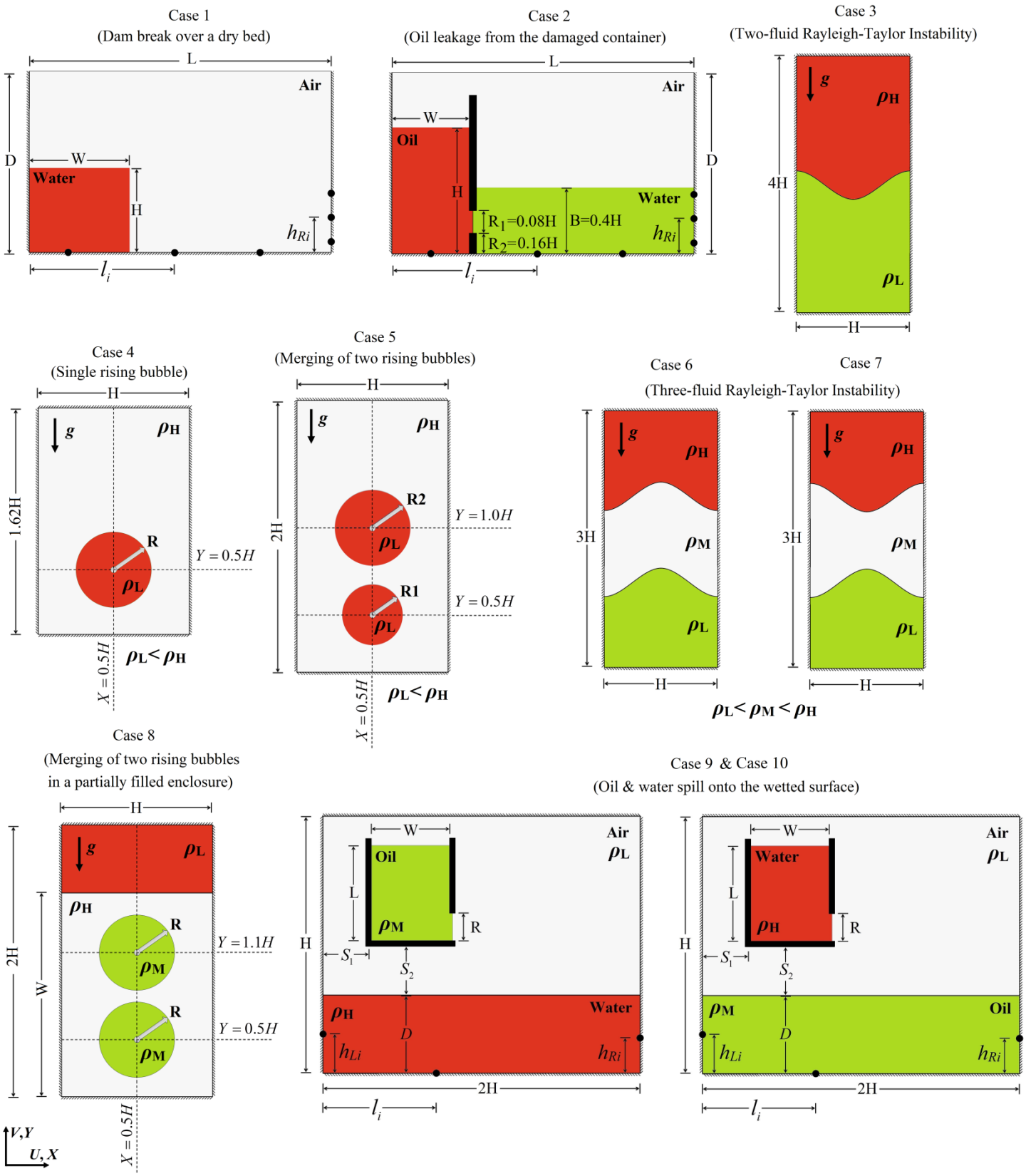

Fig. 1. Schematic diagram of ten different physical models under consideration with associated boundary conditions and coordinate system.

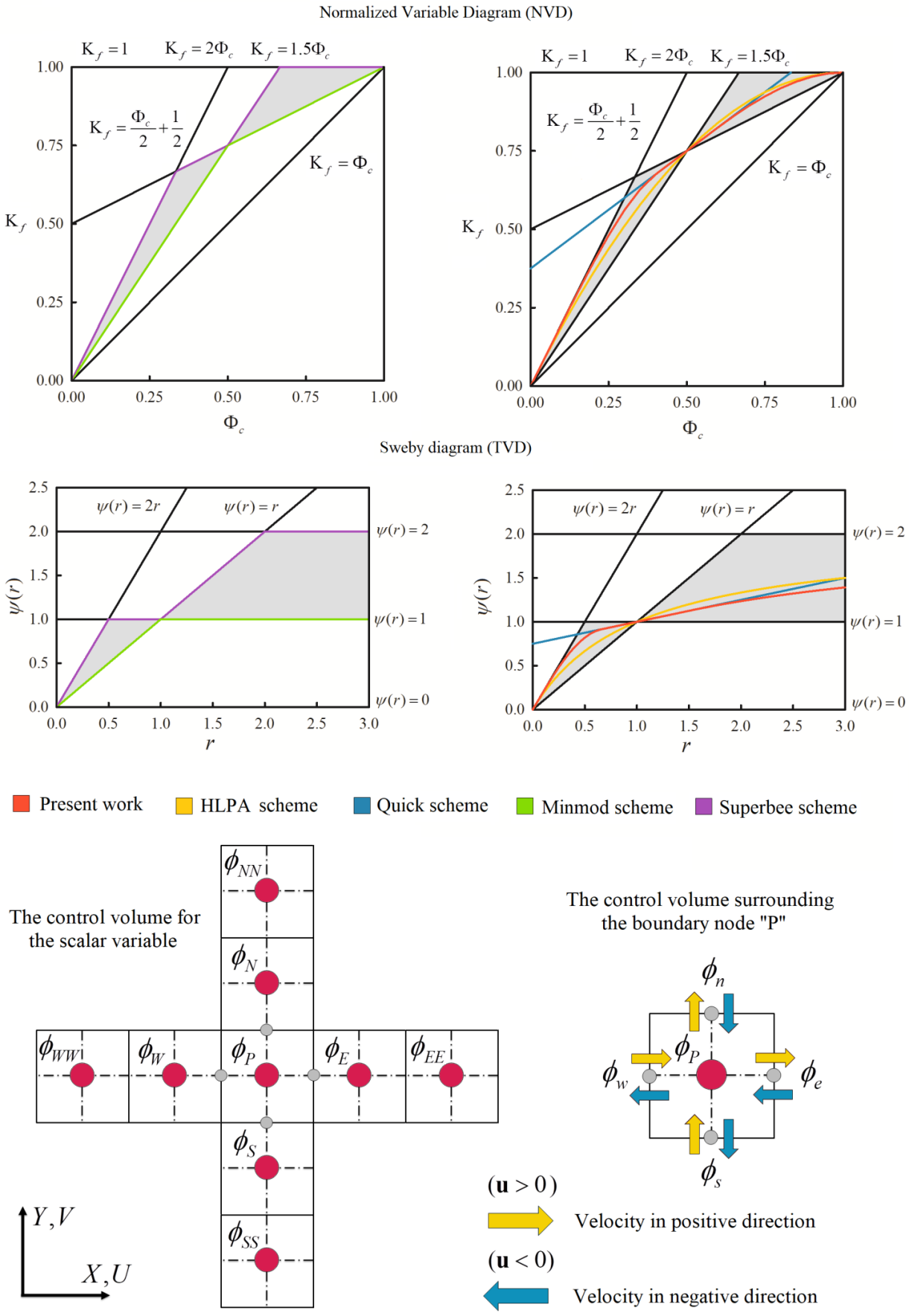

Fig. 2. (a) Normalized Variable and Sweby diagrams showing the proposed TVD-NVD model along with the four other classical convection schemes (the shaded areas stands for the TVD area). (b) The 2D staggered grid system used for discretization of the proposed bounded convection scheme.

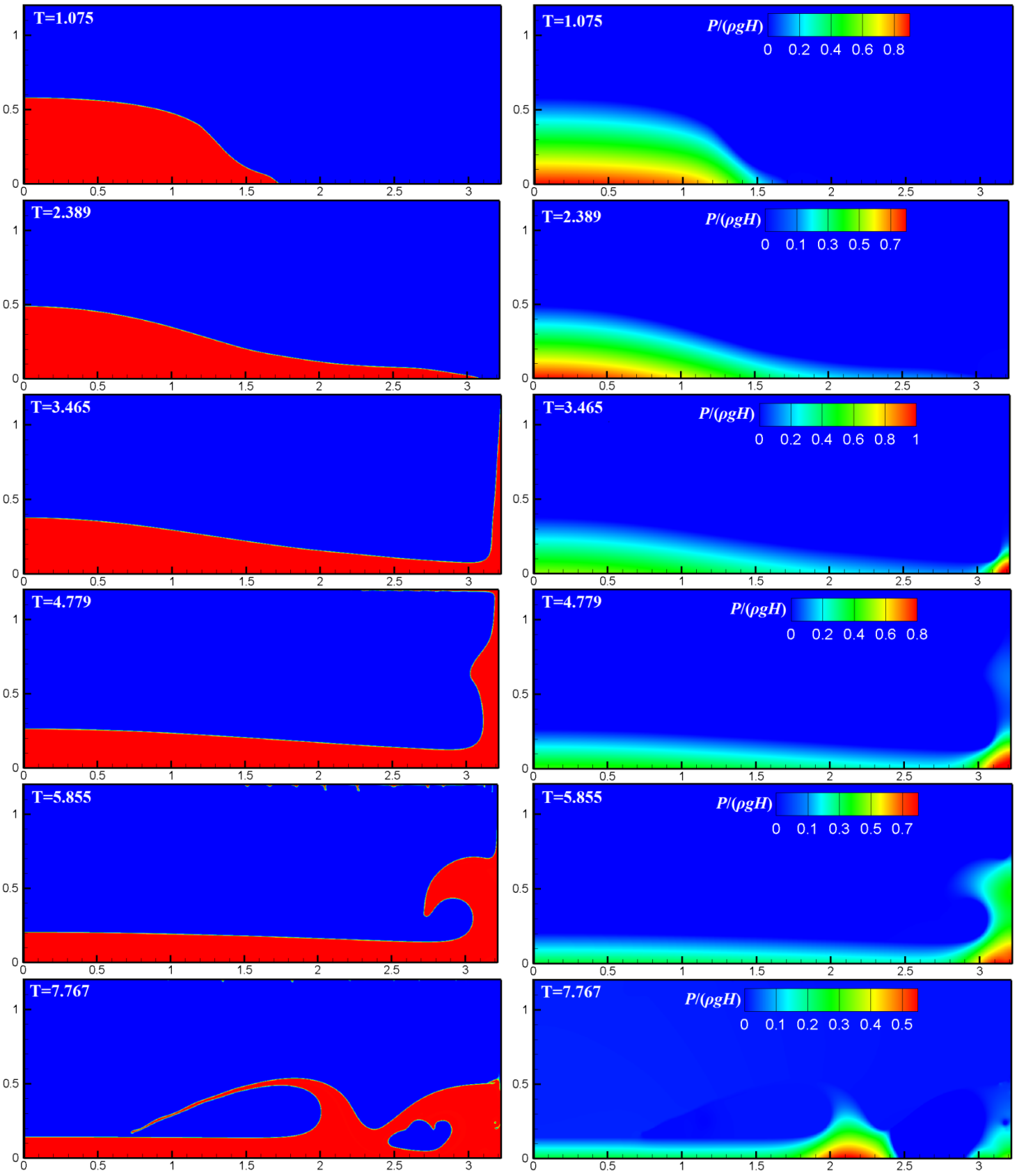

Fig. 3. Time evolution of dam-break flow (case 1) in terms of the volume-fraction and pressure contours predicted from the present work at different time instants.

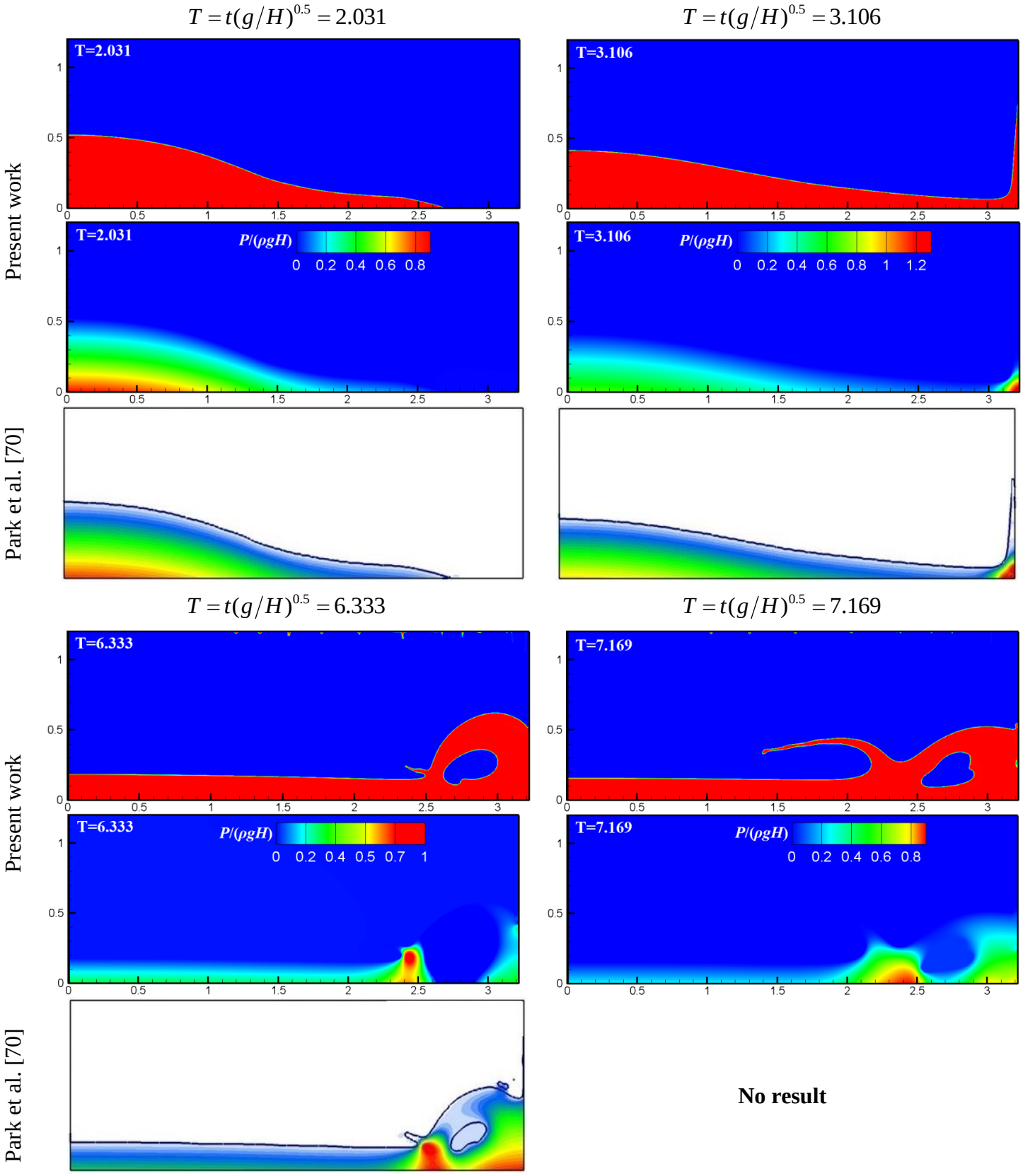

Fig. 4. Qualitative comparison of the predicted results from the current work with numerical data of Park et al. [70] in case 1.

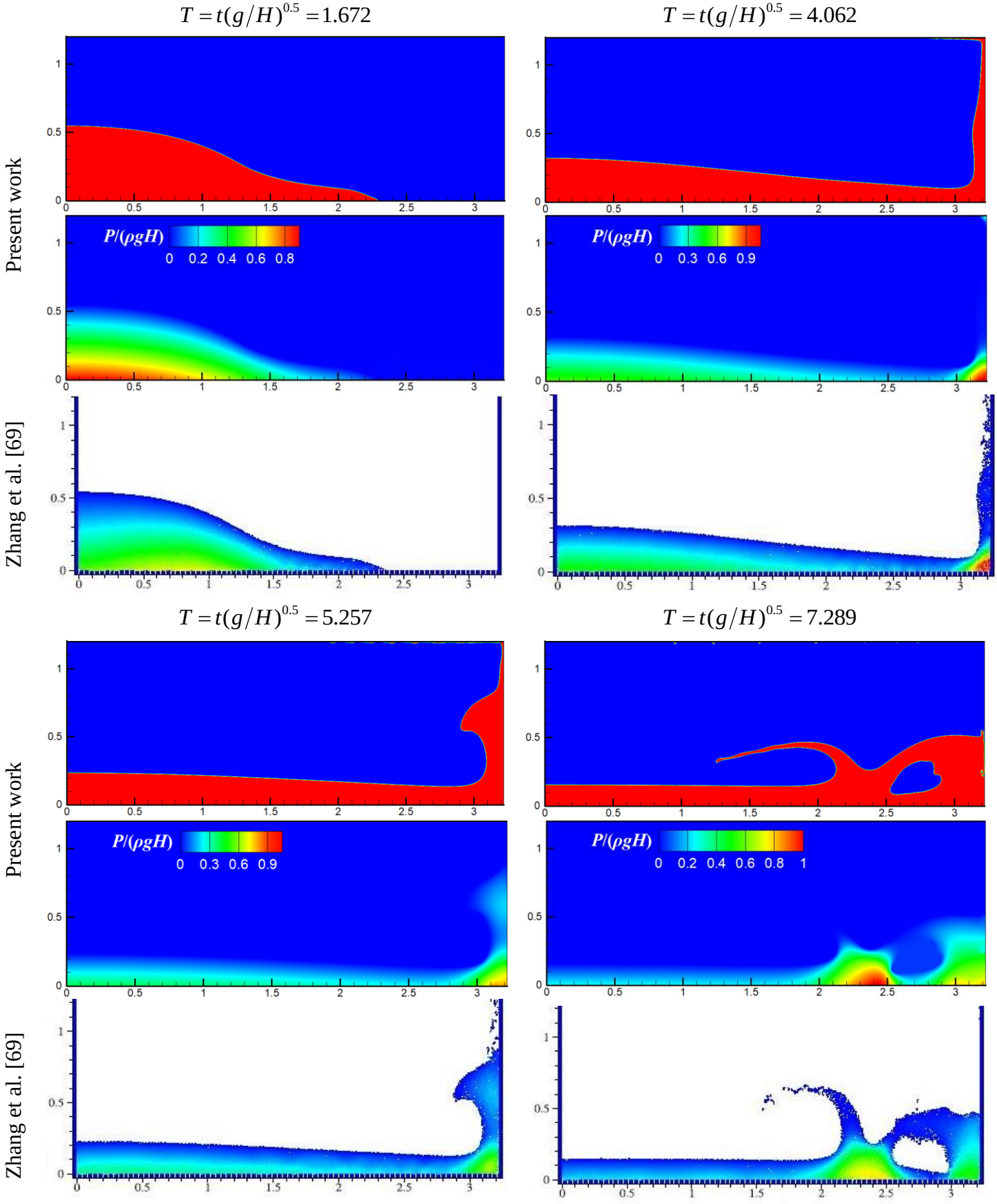

Fig. 5. Qualitative comparison of the predicted results from the current work with numerical data of Zhang et al. [69] in case 1.

(a) Time variation of water level height at section l_1=0.6m

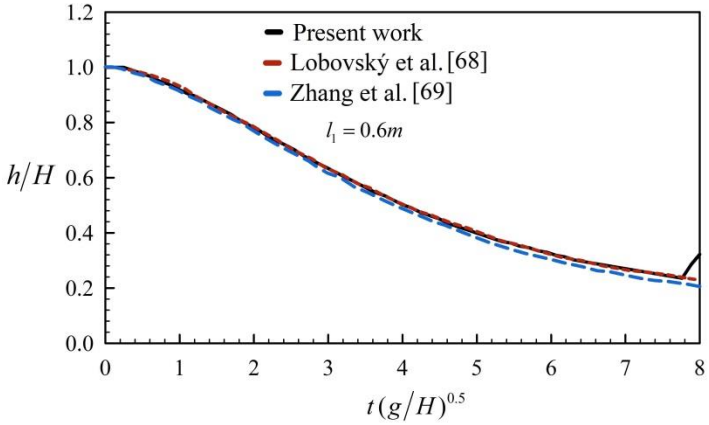

(b) Time variation of water level height at section l_2=2.228 m

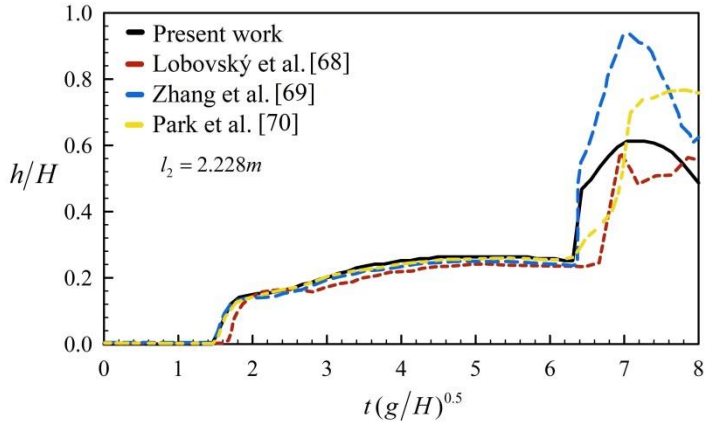

(c) Time variation of water level height at section l_3=2.725 m

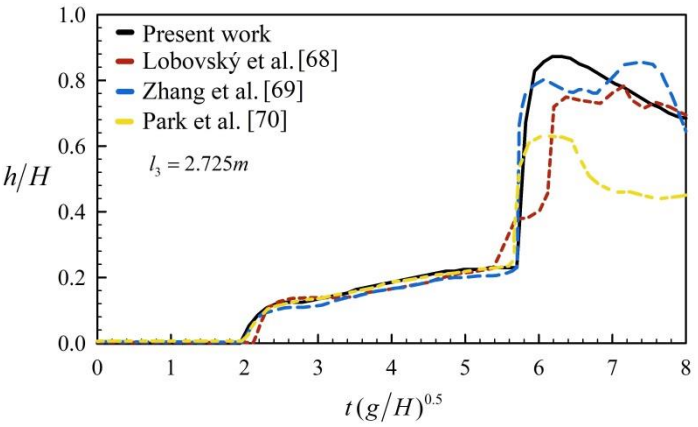

(d) Time history of pressure variations on the right wall recorded by sensor 1 (h_{R1}=0.03m)

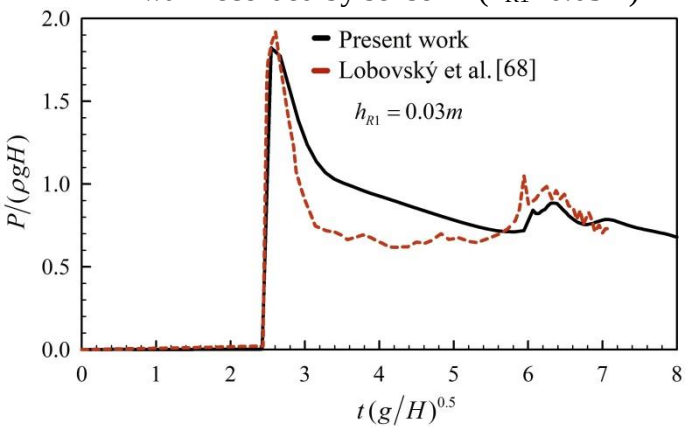

(e) Time history of pressure variations on the right wall recorded by sensor 2 (h_{R2}=0.16m)

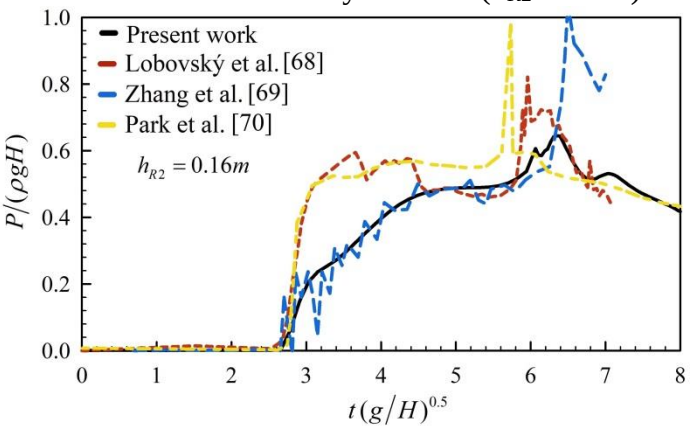

(f) Time history of wave front location

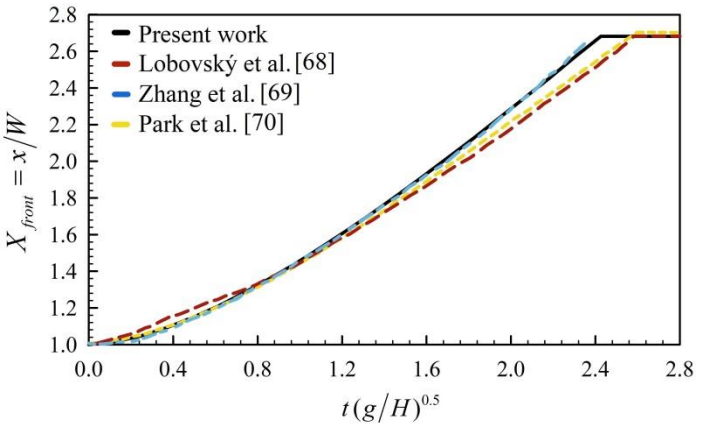

Fig. 6. Quantitative comparison of the obtained results in terms of time histories of water level height at three different sections, wave front position, and pressure variations on the right wall at two different marked points with numerical data of Park et al. [70], Zhang et al. [69] and Lobovský et al. [68] in case 1.

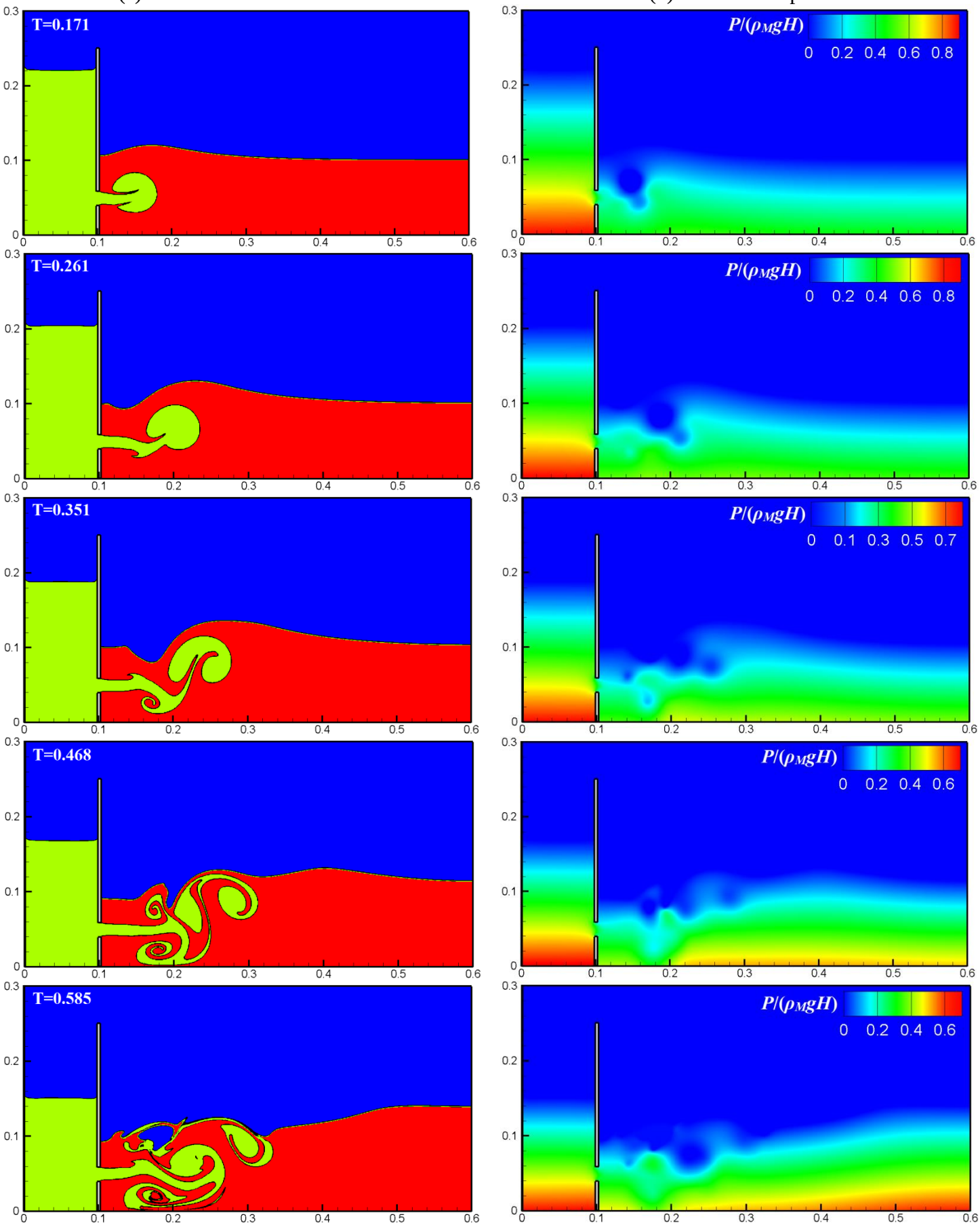

Fig. 7. Time evolution of oil spill from a damaged container (case 2) in terms of the volume-fraction and pressure fields computed from the present work at different dimensional time (*s*) instants.

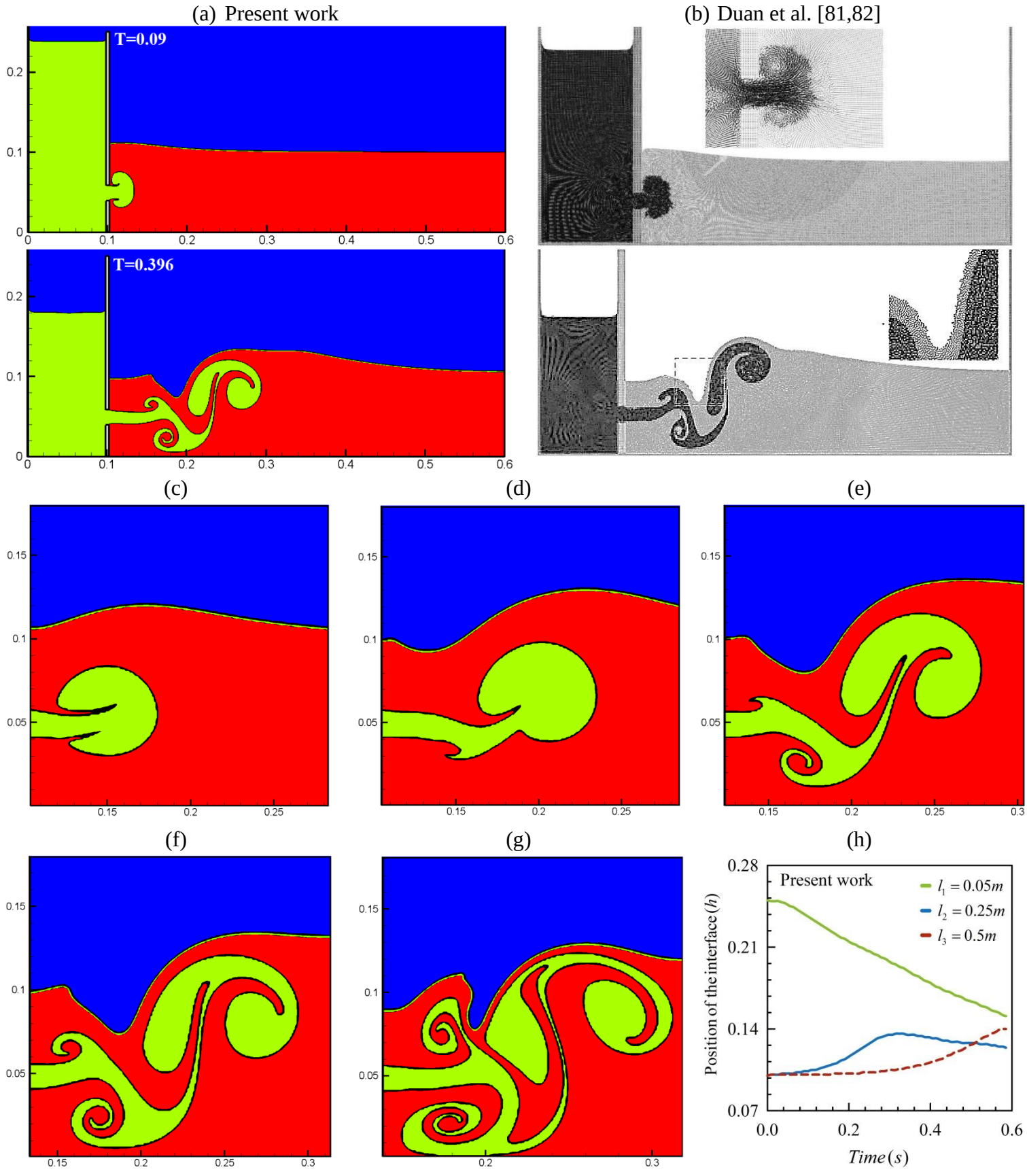

Fig. 8. (a) and (b) Qualitative comparison of the predicted results from the present work with numerical data of Duan et al. [81,82], (c) to (g) close-up views of the interface at five different time instants (i.e. T=0.171s, T=0.261s, T=0.351s, T=0.396s and T=0.468s), and (h) maximum position of the interface between liquid and gas at three different sections namely: l_1=0.05m (oil-air), l_2=0.25m (water-air), l_3=0.5m (water-air).

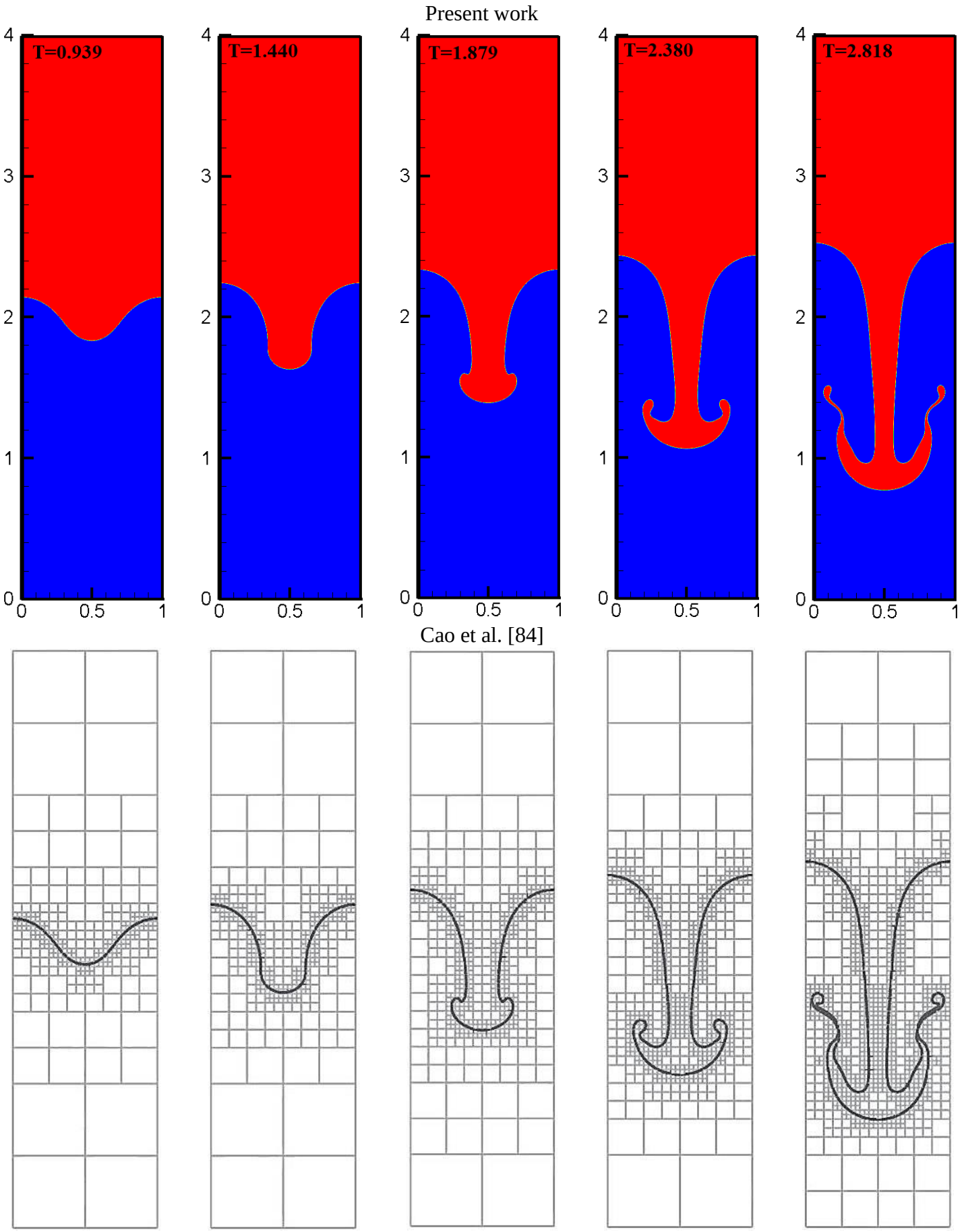

Fig. 9. Qualitative comparison of the obtained results in terms of volume fraction field with numerical work of Cao et al. [84] for case 3 (Two-fluid Rayleigh-Taylor Instability).

(a) Zoomed-in view of interface at T=2.818

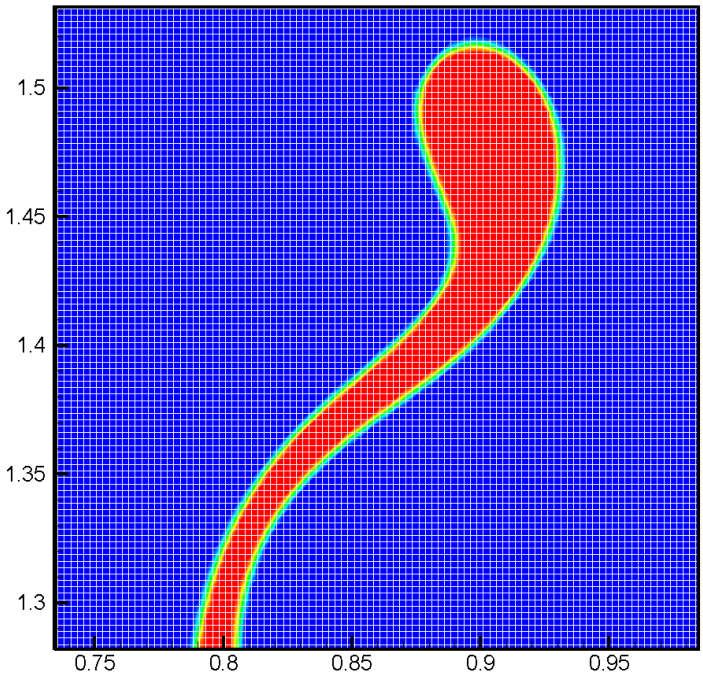

(b) Maximum and minimum position of the interface

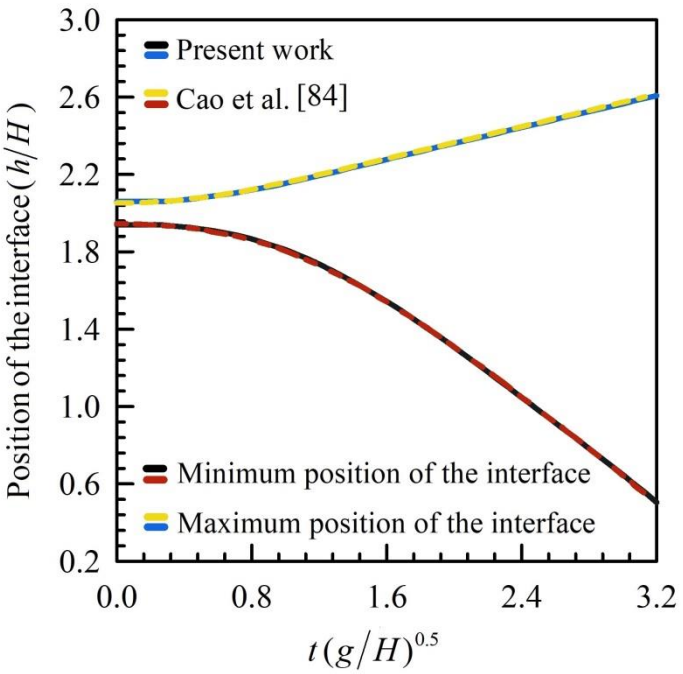

Fig. 10. (a) zoomed-in views of interface at T= 2.818 time instant and (b) quantitative comparison of the obtained results in terms of maximum and minimum location of the interface with numerical work of Cao et al. [84] for case 3 (Two-fluid Rayleigh-Taylor Instability).

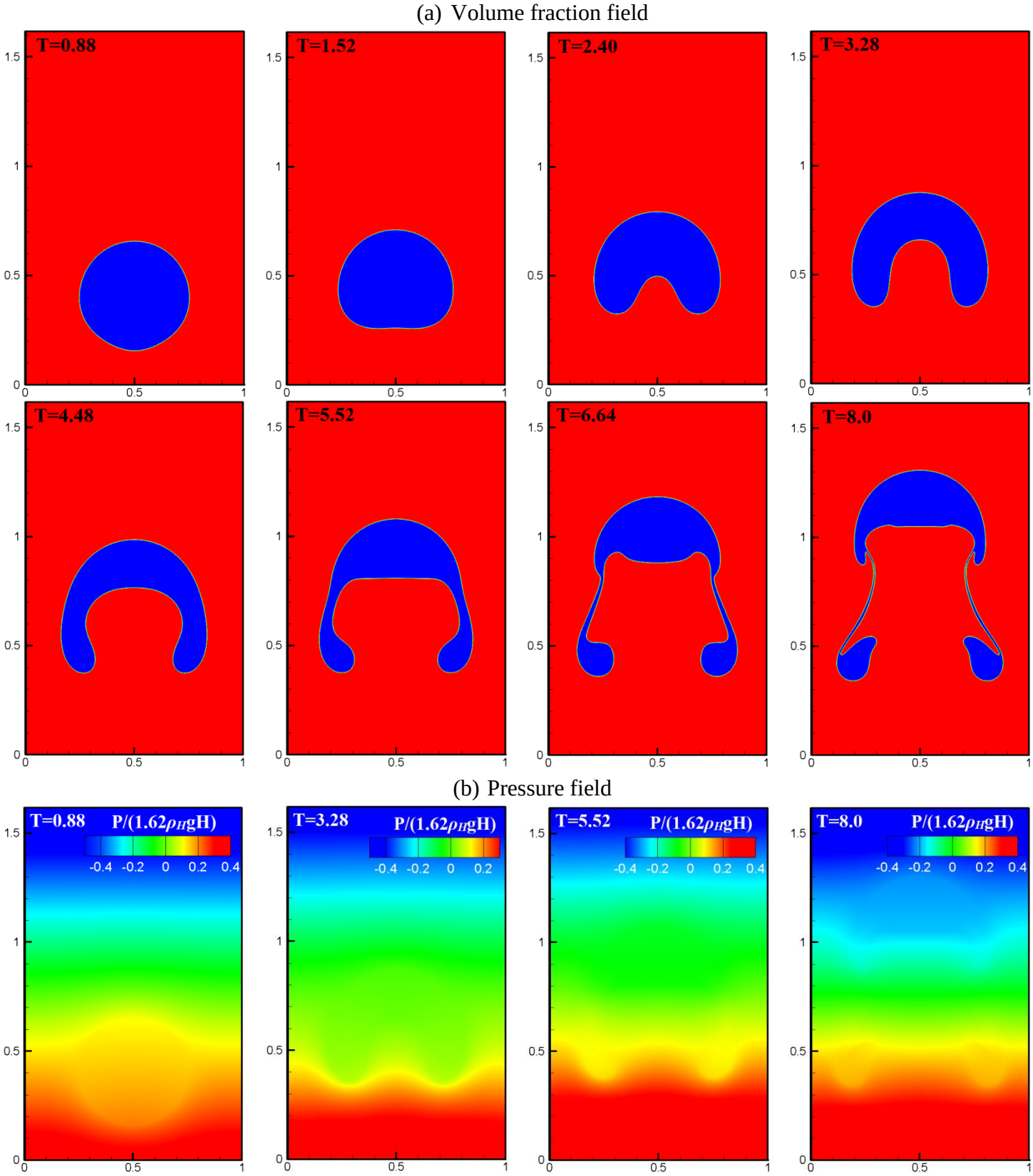

Fig. 11. Time evolution of the single rising bubble (case 4) in terms of the volume-fraction and pressure fields predicted from the present work at different time instants.

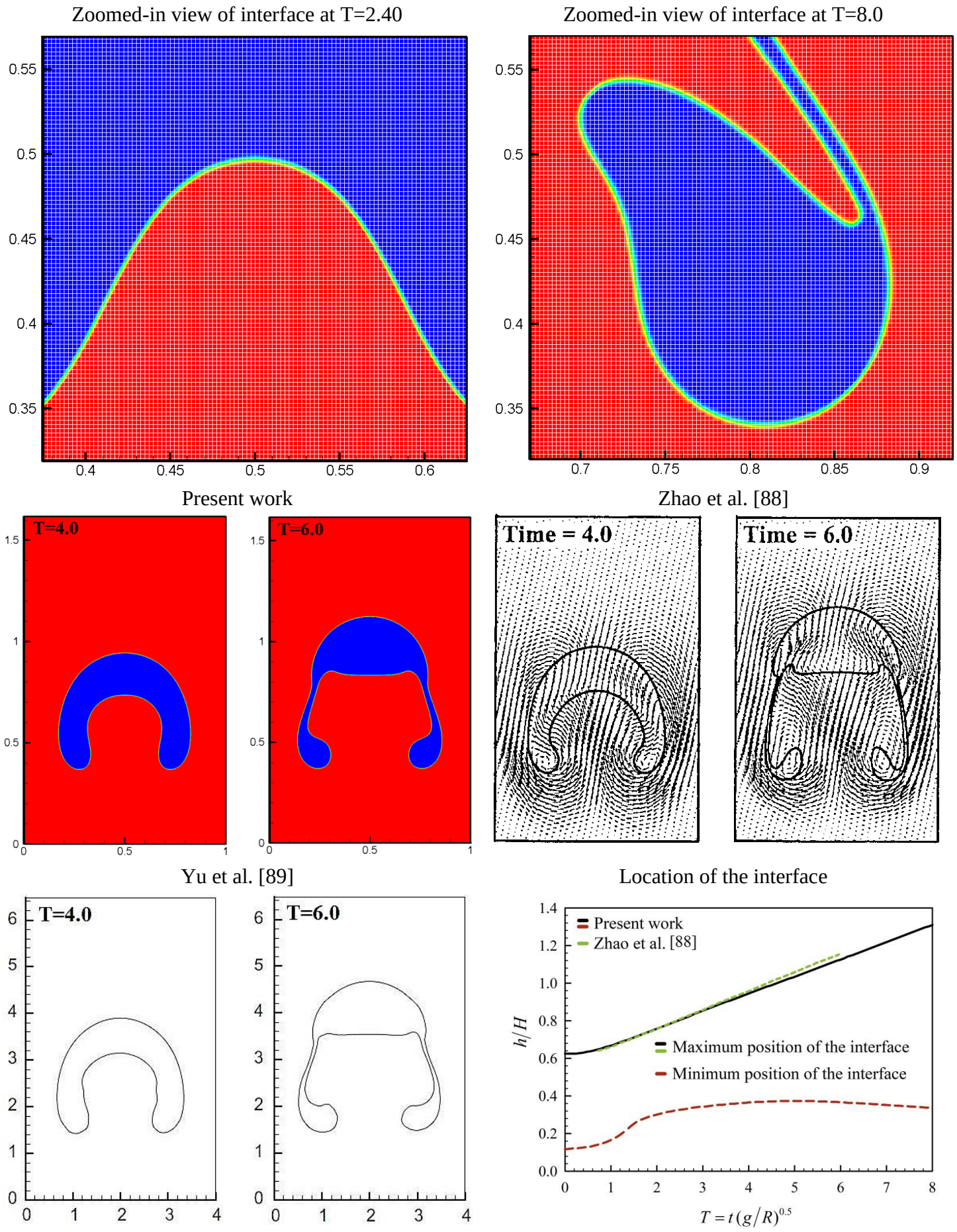

Fig. 12. Comparison of the obtained results with numerical data of Zhao et al. [88] and Yu et al. [89] for case 4.

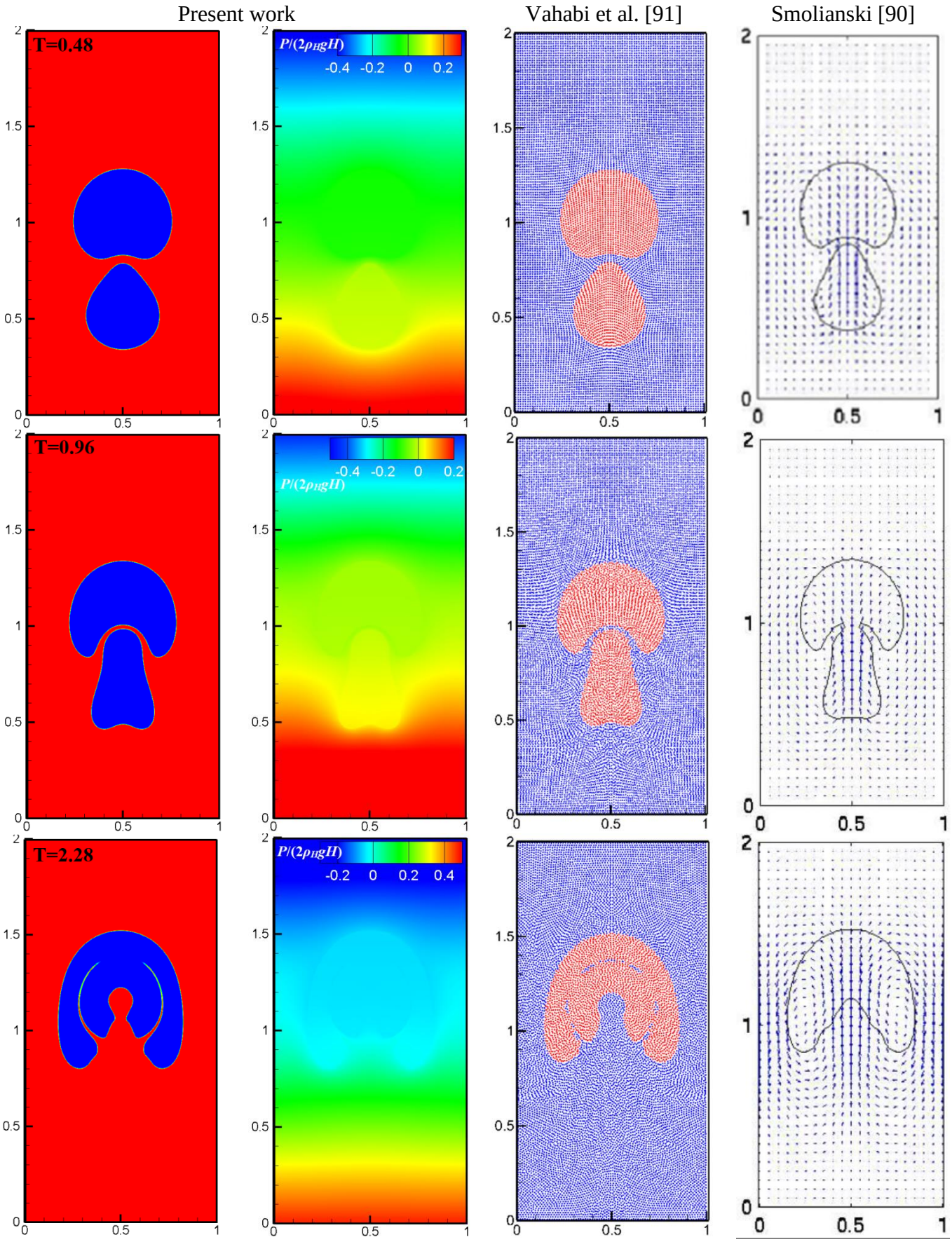

Fig. 13. Qualitative comparison of the obtained results in terms of volume fraction and pressure fields with numerical works of Vahabi et al. [91] and Smolianski [90] for case 5 (merging of two rising bubbles).

(a) Zoomed-in view of interface at T=0.96

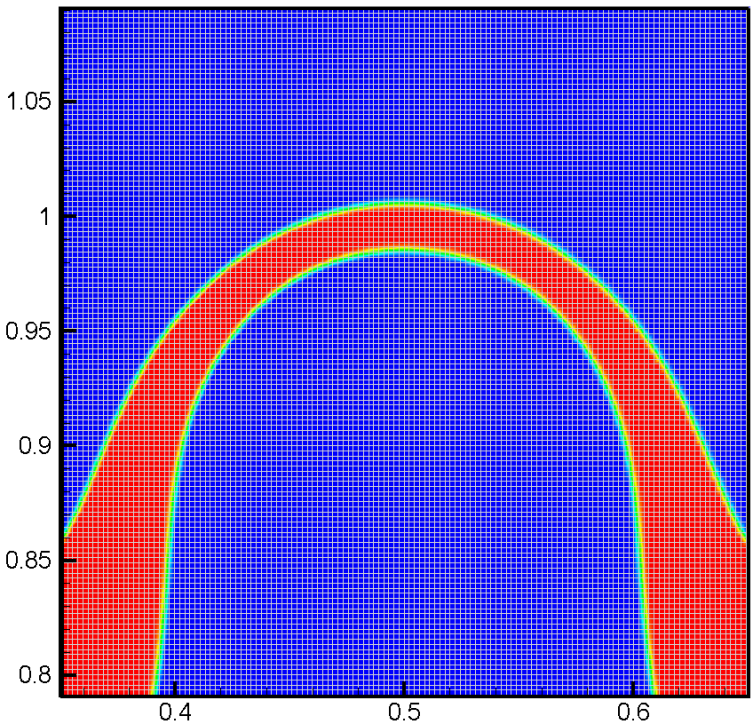

(b) Maximum and minimum location of the interface

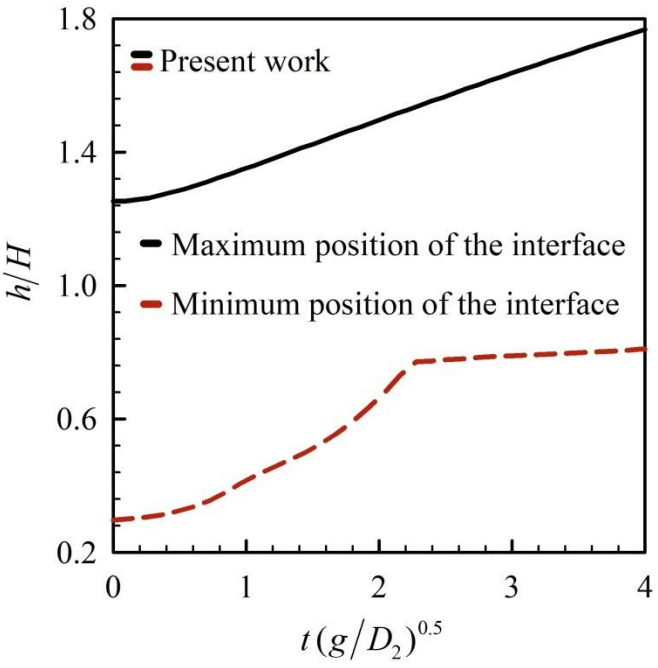

Fig. 14. (a) Zoomed-in view of the bubble interface and (b) the time histories of maximum and minimum positions of the interface predicted from the present study in case 5.

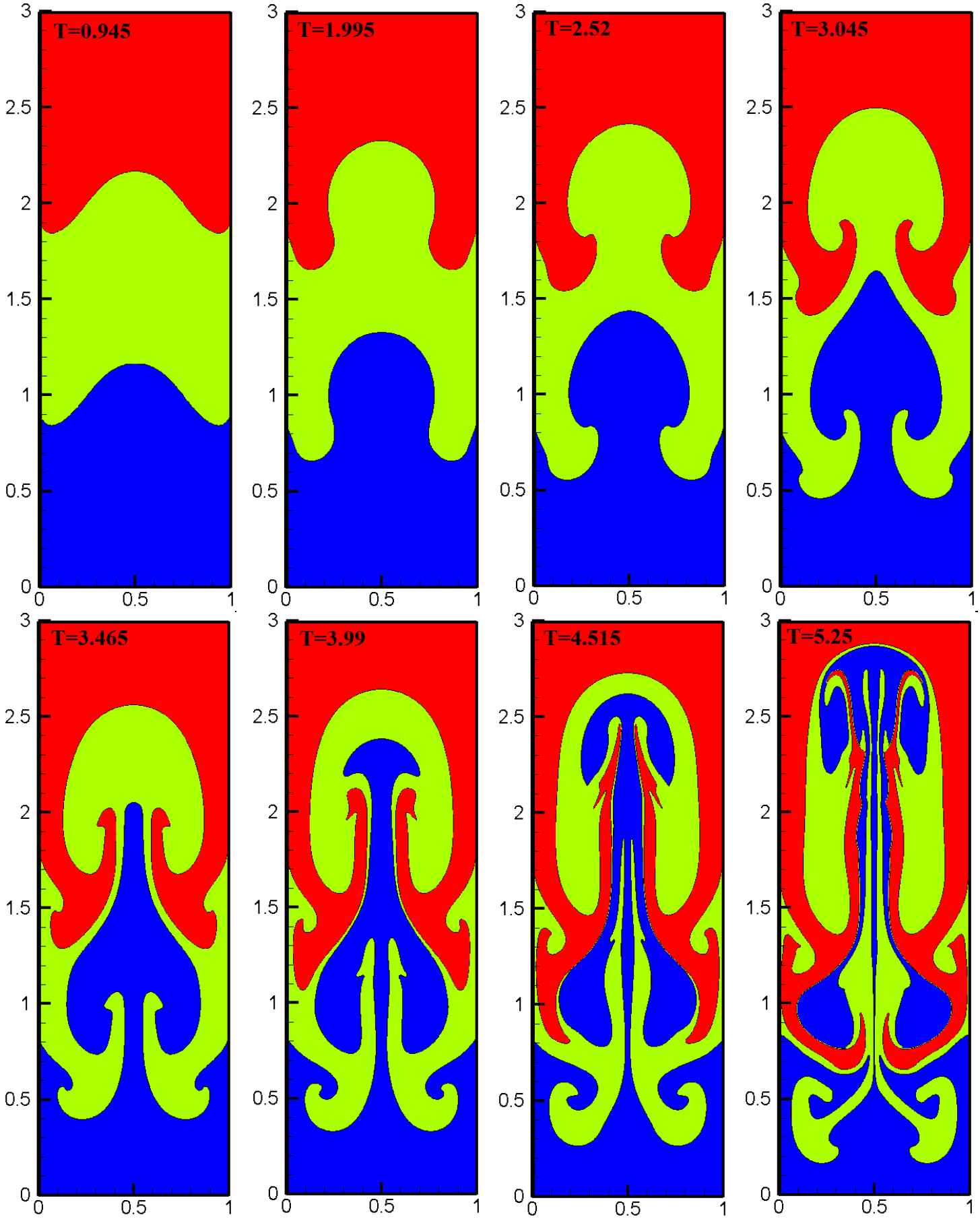

Fig. 15. Time evolution of three-fluid Rayleigh-Taylor Instability (case 6) in terms of the volume-fraction field predicted from the present work at different time instants.

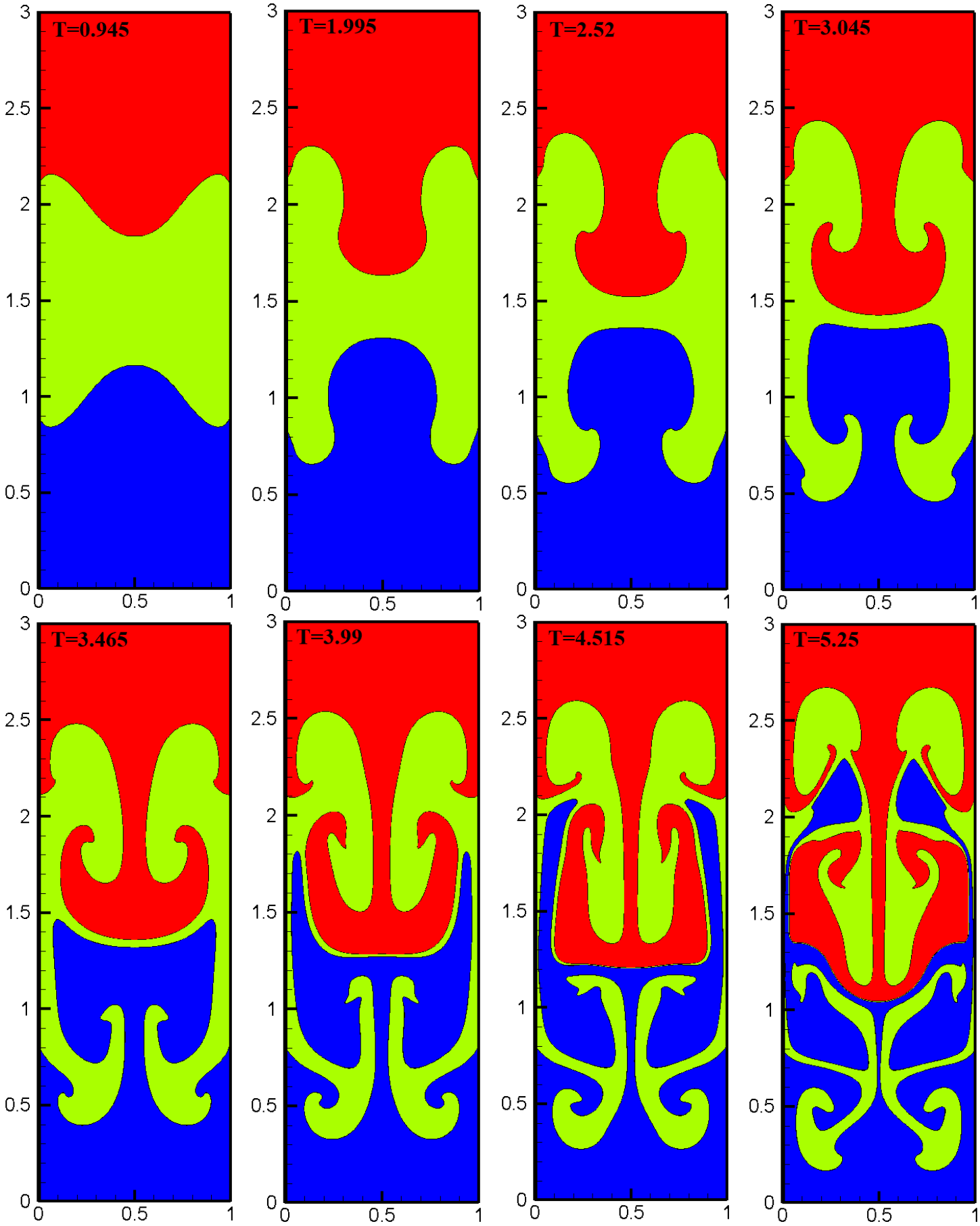

Fig. 16. Time evolution of three-fluid Rayleigh-Taylor Instability (case 7) in terms of the volume-fraction field predicted from the present work at different time instants.

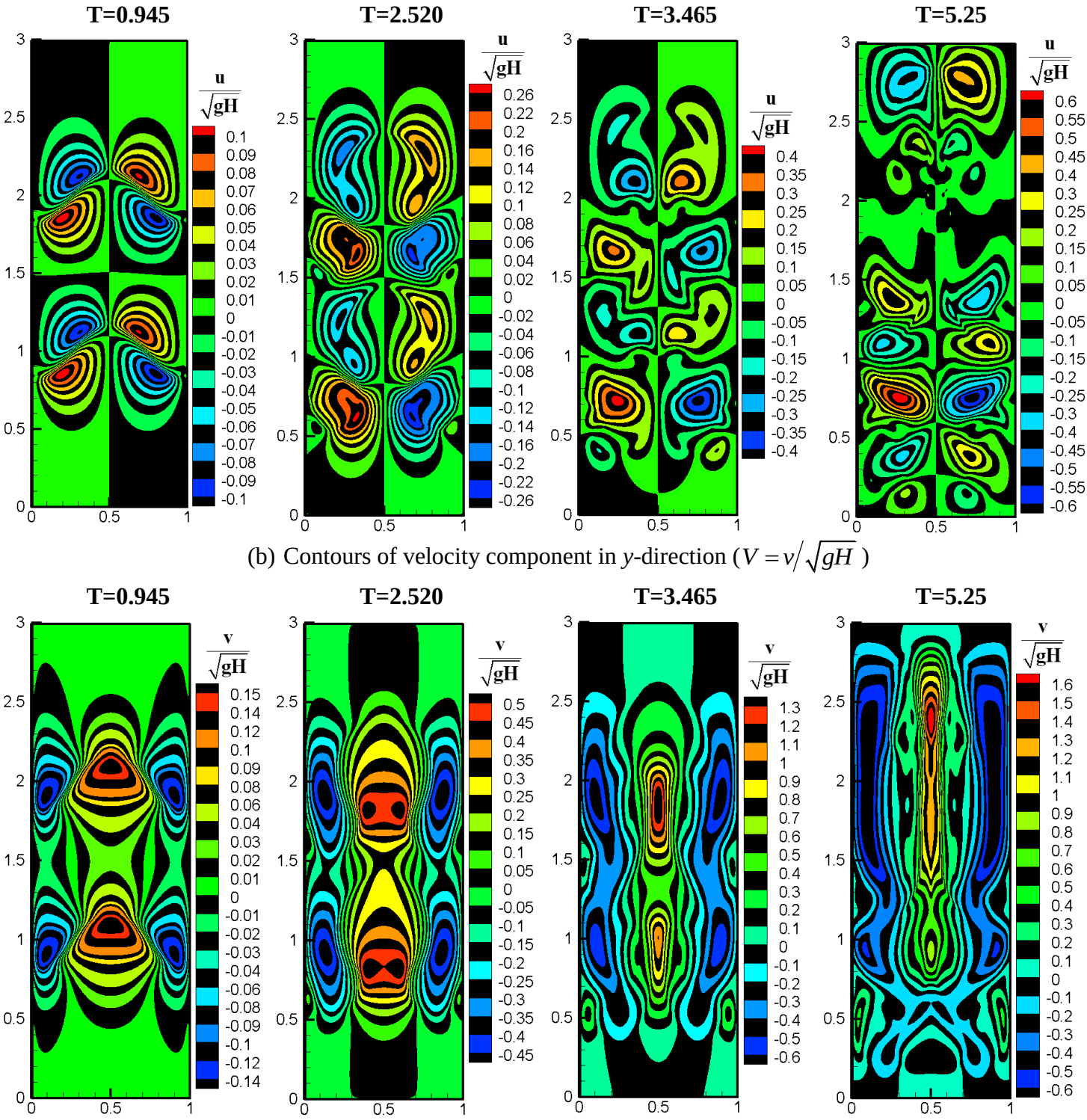

Fig. 17. Contours of velocity components in the x and y-directions (u,v) for three-fluid Rayleigh-Taylor instability problem. Case 6 (perturbed interfaces in the same directions).

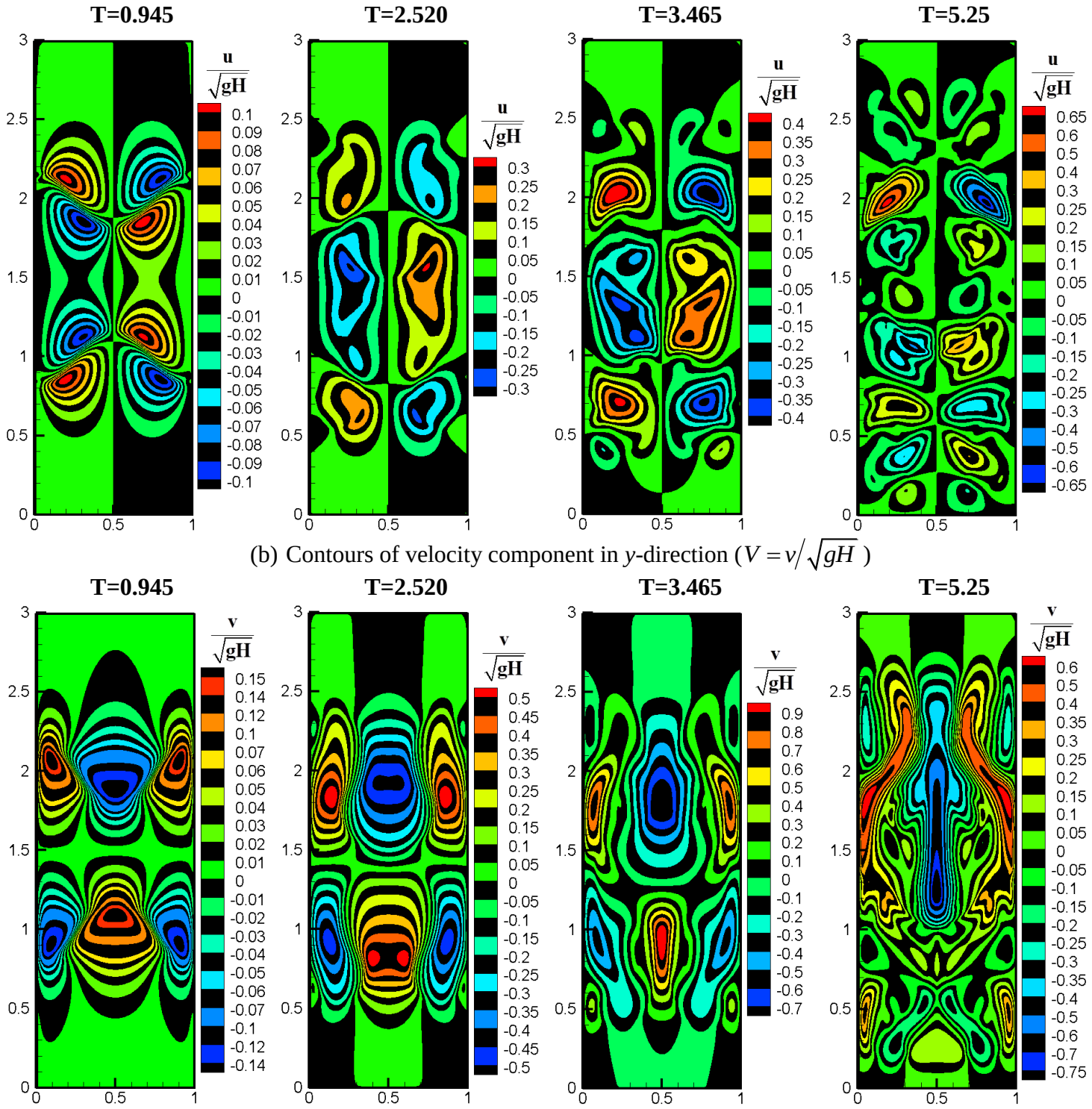

Fig. 18. Contours of velocity in the x and y-directions (u,v) for three-fluid Rayleigh-Taylor instability problem. Case 7 (perturbed interfaces in the opposite directions).

(a) Zoomed-in view of the interfaces at T=3.99 in case 6

(b) Zoomed-in view of the interfaces at T=5.25 in case 7

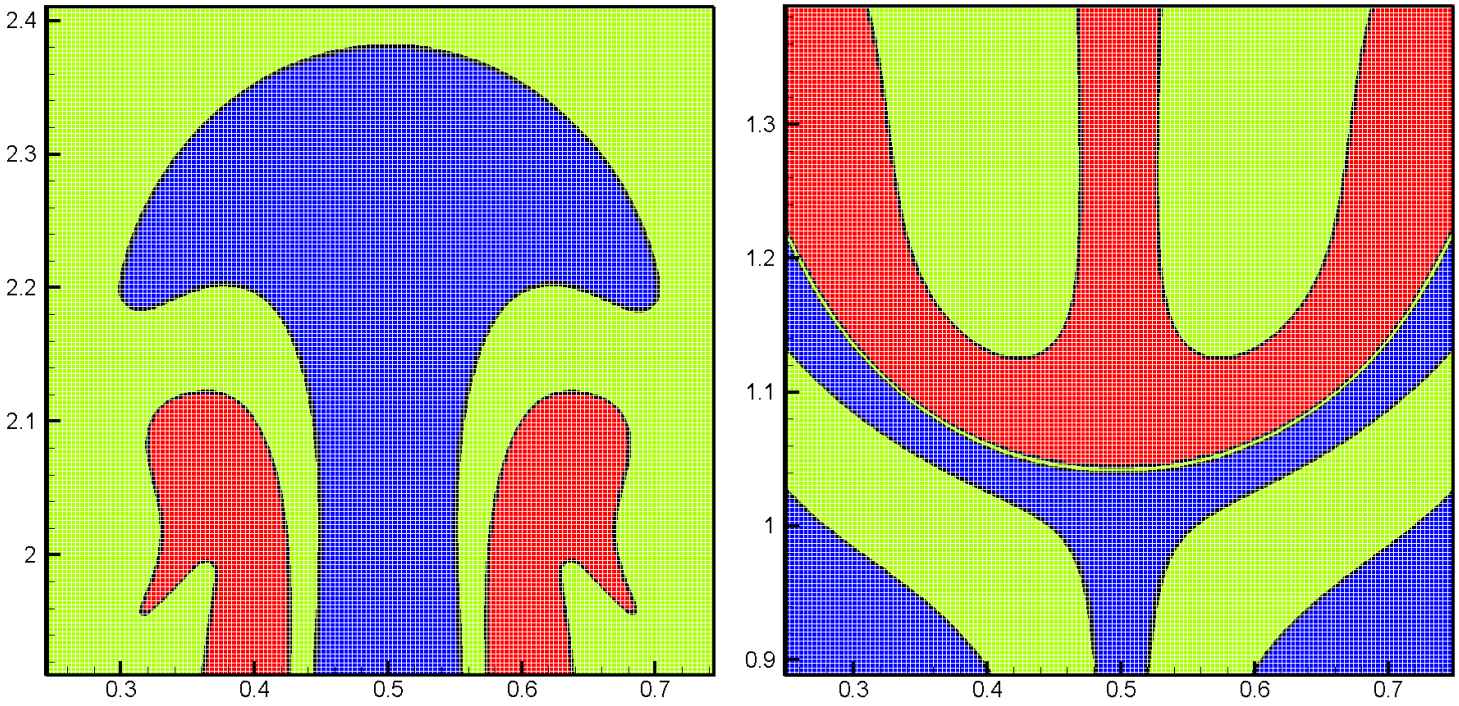

(c) Location of the interfaces in case 6

(d) Location of the interfaces in case 7

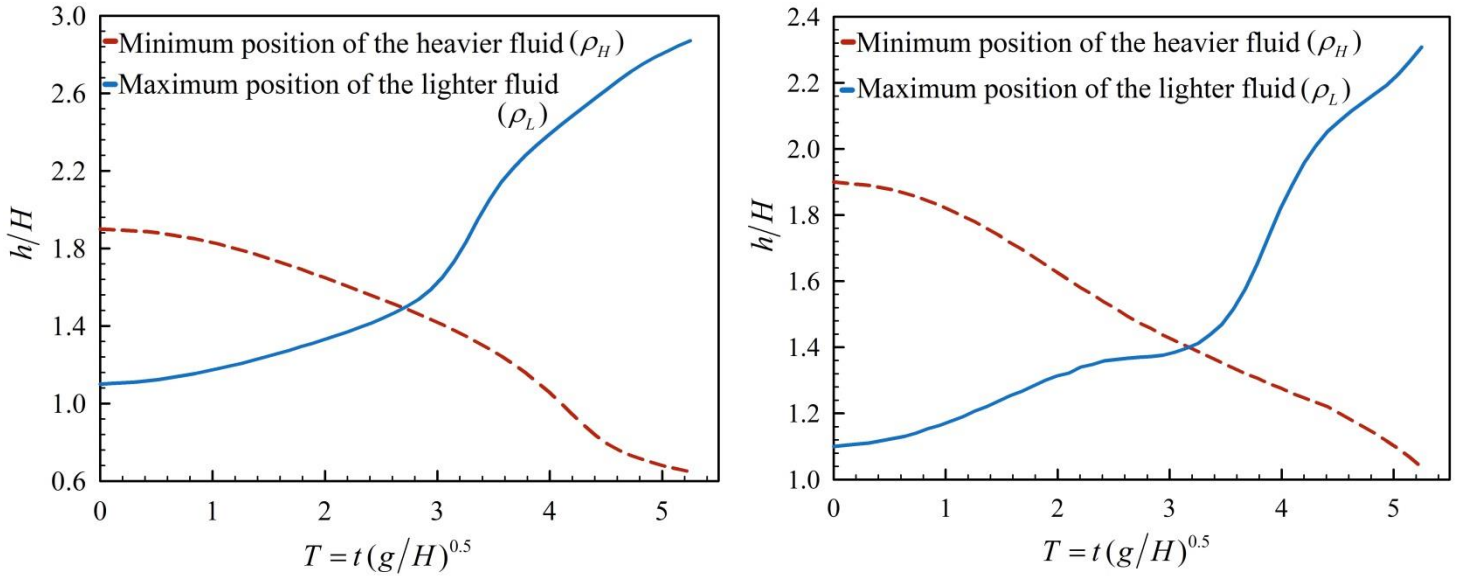

Fig. 19. (a) and (b) enlarged views of the interface in cases 6 and 7, (c) and (d) the time histories of maximum and minimum positions of the heavier (ρ_H) and lighter (ρ_L) fluids in cases 6 and 7.

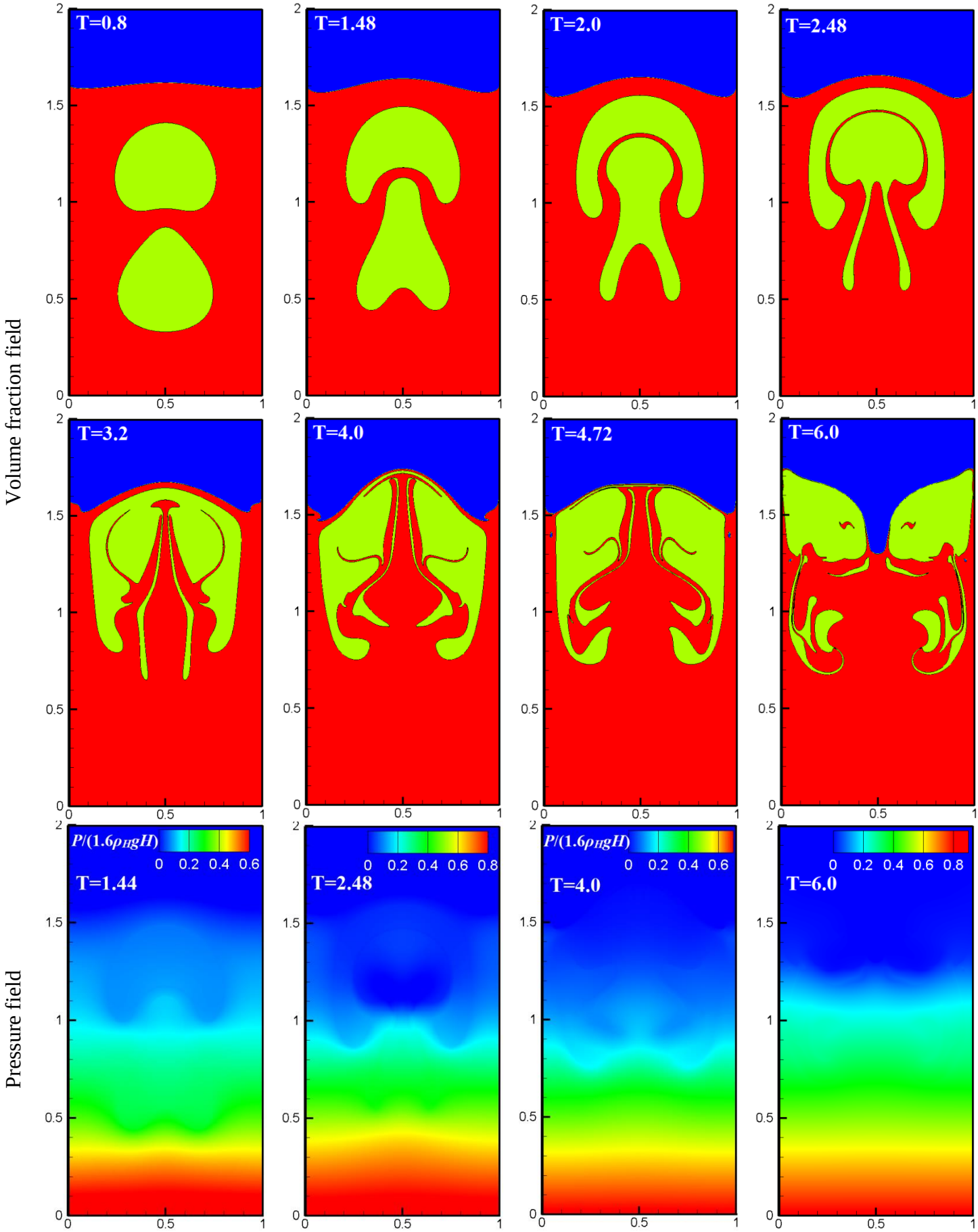

Fig. 20. Time evolution of two rising bubbles in partially filled enclosure (case 8) in terms of volume-fraction and pressure fields predicted from the present work at different time instants.

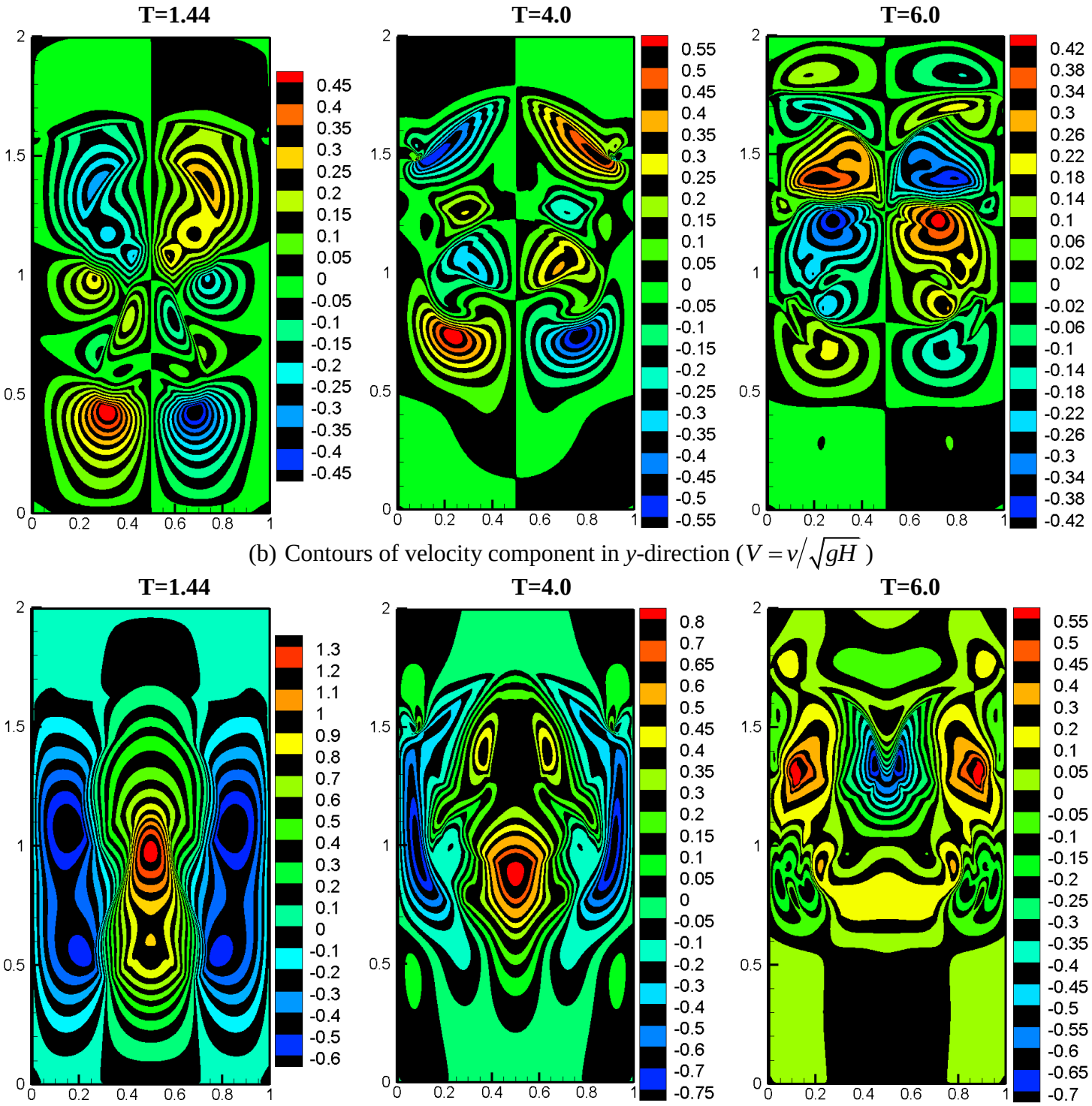

Fig. 21. Contours of velocity in the *x* and *y*-directions (*u*,*v*) in case 8 (coalescence of two consecutive bubbles inside the partially filled enclosure).

(a) Zoomed-in view of interface at T=4.0

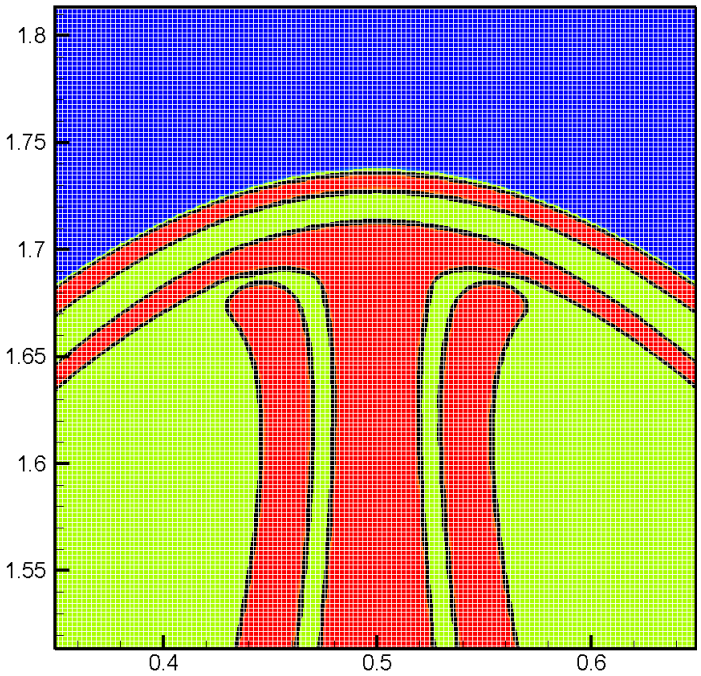

(b) Time variation of maximum and minimum positions of rising bubbles

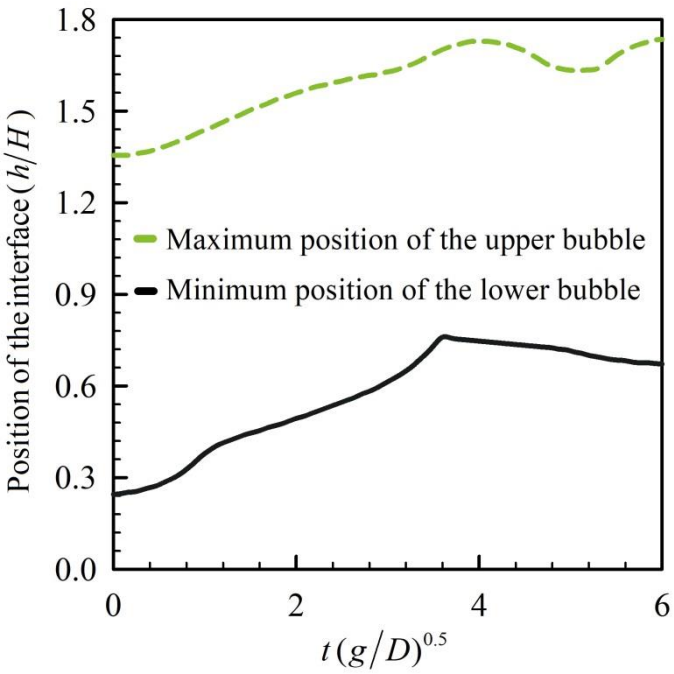

Fig. 22. (a) Enlarged view of the interface evolution in case 8 at T=4.0 and (b) time variation of maximum and minimum positions of rising bubbles.

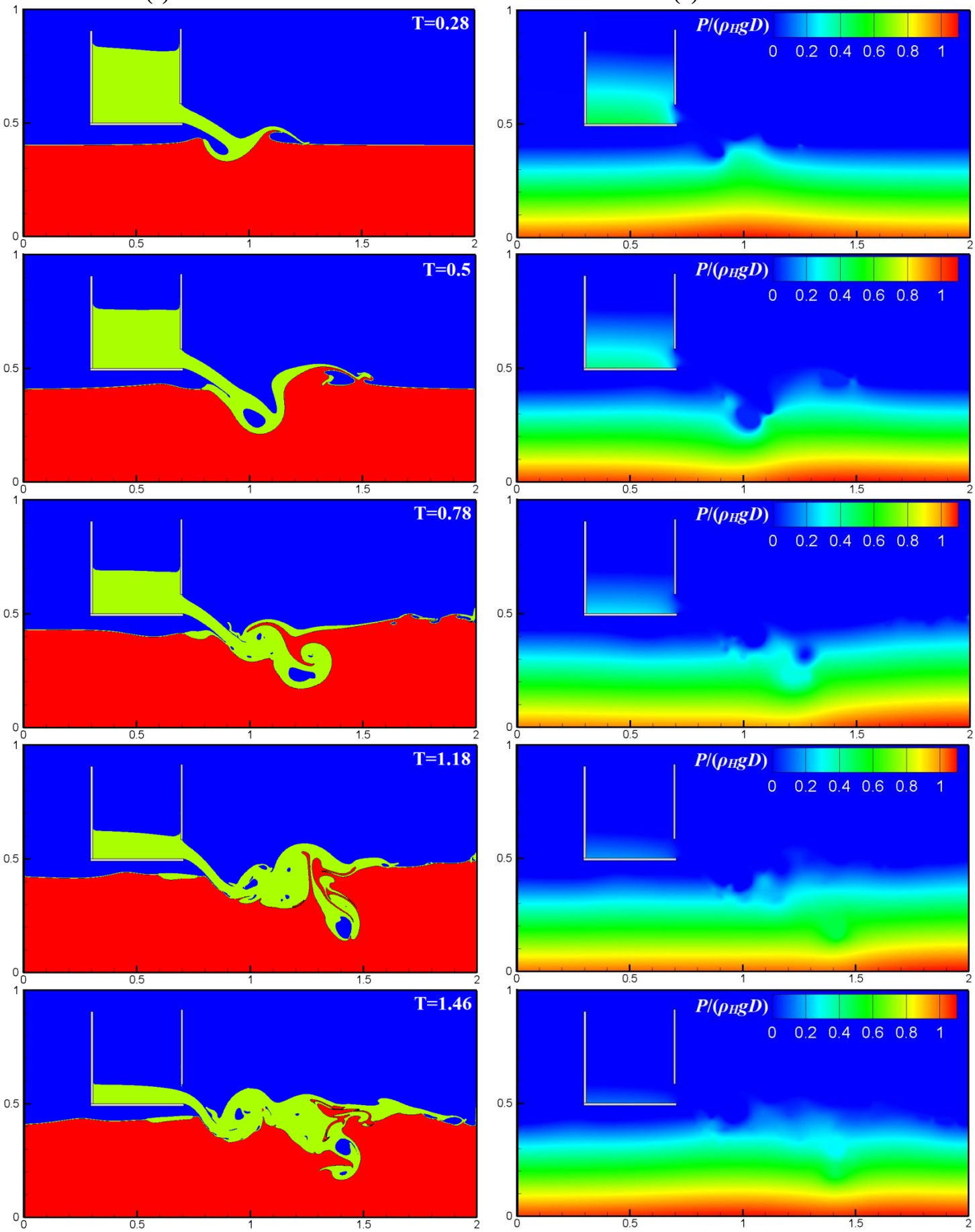

Fig. 23. Time evolution of the oil spill onto the wetted water surface at different time instants (case 9).

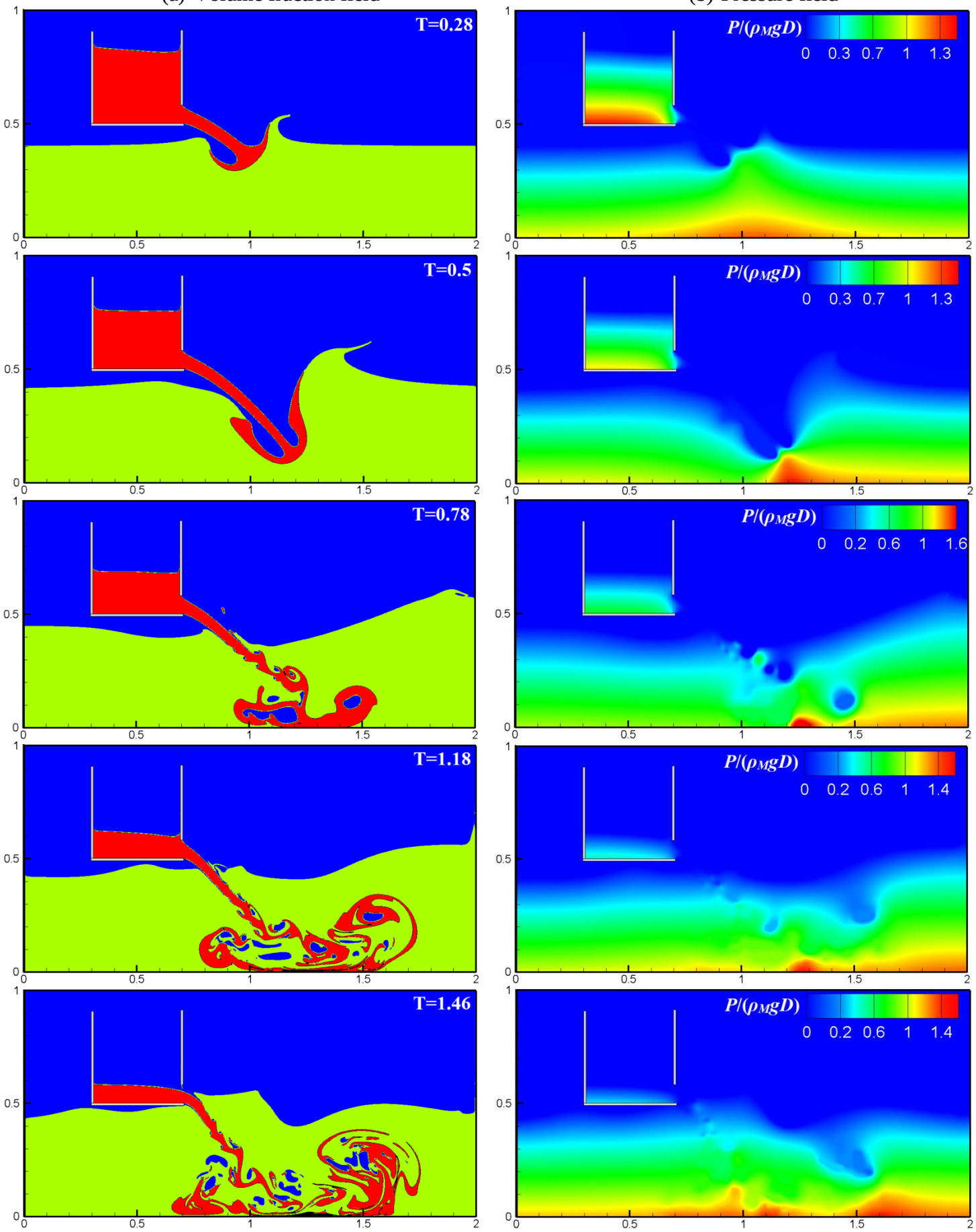

Fig. 24. Time evolution of the water spill onto the wetted oil surface at different time instants (case 10).

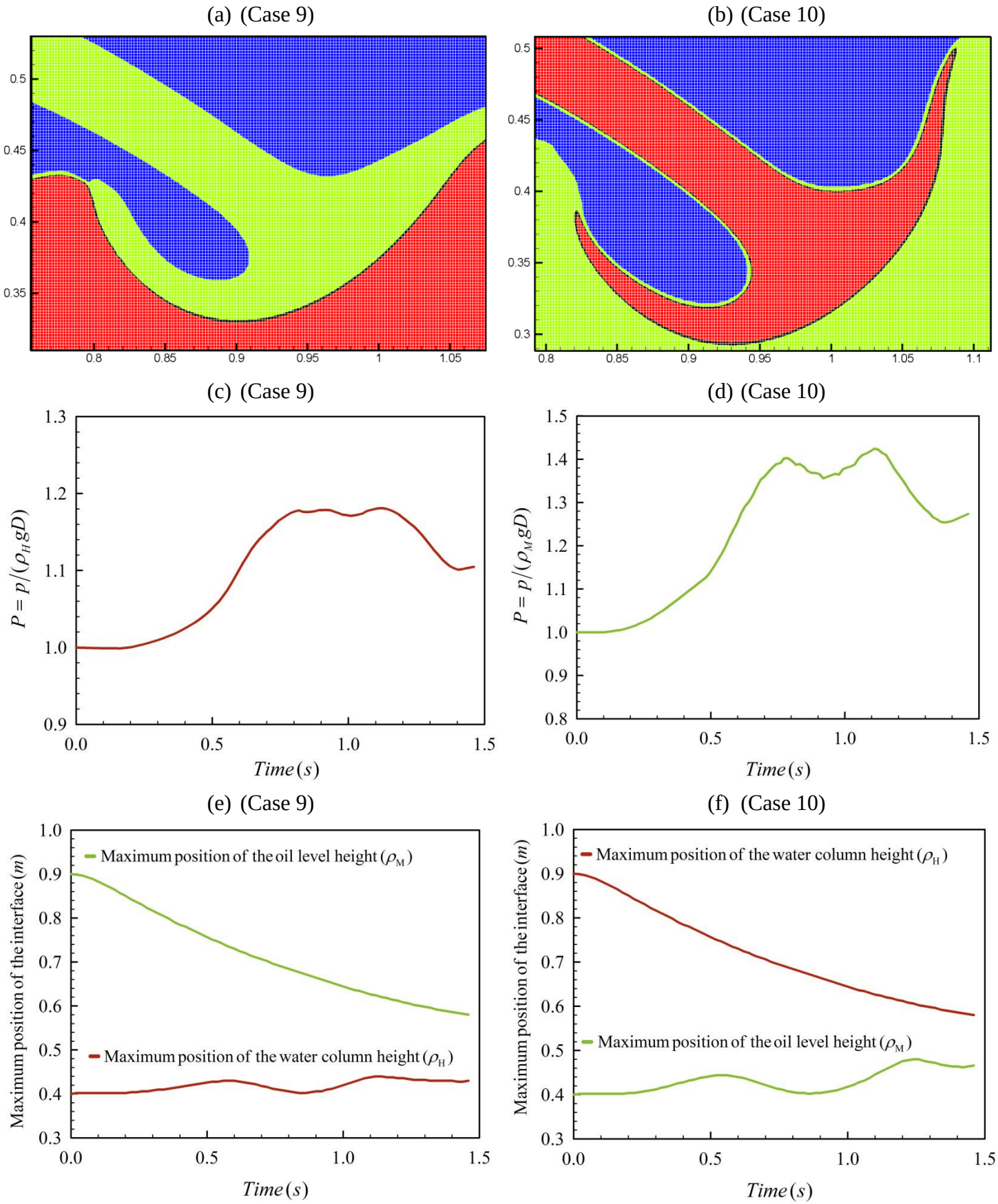

Fig. 25. (a) and (b) zoomed-in views of interface at t=0.28 in cases 9 and 10, (c) and (d) Time history of pressure variation on the bottom-right corner of the container (h_{R1}=0.0) in cases 9 and 10, (e) and (f) time variations of the maximum position of the interfaces at section x=0.5m.

Table 1. The linear and non-linear convection schemes defined in the Sweby and NV diagrams.

Scheme	Normalized function in Sweby diagram	Normalized function in NV diagram
1st order Upwind	$\psi(r)=0$	$K_f=\Phi_c$
2nd order Upwind	$\psi(r)=r$	$K_f=\frac{3\Phi_c}{2}$
Quick	$\psi(r)=\frac{r}{4}+\frac{3}{4}$	$K_f=\frac{3\Phi_c}{4}+\frac{3}{8}$
Central	$\psi(r)=1$	$K_f=\frac{\Phi_c}{2}+\frac{1}{2}$
2nd order HLPA	$\psi(r)=\frac{\lvert r\rvert+r}{1+r}$	$K_f=-\Phi_c^2+2\Phi_c$
Minmod	$\psi(r)=\begin{cases}\frac{\lvert r\rvert+r}{2} & r\le 1\\ 1 & r>1\end{cases}$	$K_f=\begin{cases}\frac{3}{2}\Phi_c & 0\le\Phi_c\le 0.5\\ \frac{1}{2}\Phi_c+\frac{1}{2} & 0.5<\Phi_c\le 1.0\\ \Phi_c & 0.5<\lvert\Phi_c-0.5\rvert\end{cases}$
Superbee	$\psi(r)=\begin{cases}\lvert r\rvert+r & r\le 0.5\\ 1 & 0.5<r\le 1\\ r & 1<r\le 2\\ 2 & r>2\end{cases}$	$K_f=\begin{cases}2\Phi_c & 0\le\Phi_c\le\frac{1}{3}\\ \frac{1}{2}\Phi_c+\frac{1}{2} & \frac{1}{3}<\Phi_c\le\frac{1}{2}\\ \frac{3}{2}\Phi_c & \frac{1}{2}<\Phi_c\le\frac{2}{3}\\ 1 & \frac{2}{3}<\Phi_c\le 1\\ \Phi_c & 0.5<\lvert\Phi_c-0.5\rvert\end{cases}$